

GEOLOGICA ULTRAIECTINA

Mededelingen van de  
Faculteit Aardwetenschappen  
Universiteit Utrecht

No. 145

**SEISMOLOGICAL ASPECTS OF  
INTERMEDIATE AND SMALL-SCALE  
UPPER MANTLE STRUCTURE**

**Considerations on a global and regional scale**

M.L. Passier

GEOLOGICA ULTRAIECTINA

Mededelingen van de  
Faculteit Aardwetenschappen  
Universiteit Utrecht

No. 145

**SEISMOLOGICAL ASPECTS OF  
INTERMEDIATE AND SMALL-SCALE  
UPPER MANTLE STRUCTURE**

**Considerations on a global and regional scale**

M.L. Passier

Promotor: Prof. Dr R.K. Snieder  
Department of Geophysics, Utrecht University,  
Utrecht, Netherlands.

Members of the dissertation committee:

Dr Ir G.C. Herman: Faculty of Technical Mathematics and Informatics,  
Delft University of Technology, Delft, Netherlands.

Prof. Dr J.C. Mondt: Department of Geophysics,  
Utrecht University, Utrecht, Netherlands.  
Royal/Shell Exploration and Production,  
The Hague, Netherlands.

Prof. Dr G. Poupinet: Laboratoire de Géophysique Interne et de Tectonophysique,  
Université de Grenoble, Grenoble, France.

Prof. Dr N.J. Vlaar: Department of Geophysics,  
Utrecht University, Utrecht, Netherlands.

Prof. Dr S.H. White: Department of Geology,  
Utrecht University, Utrecht, Netherlands.

**SEISMOLOGICAL ASPECTS OF  
INTERMEDIATE AND SMALL-SCALE  
UPPER MANTLE STRUCTURE**

**Considerations on a global and regional scale**

Seismologische aspecten van middelgrote en kleinschalige  
structuren in de bovenmantel—beschouwingen  
op globale en regionale schaal

(met een samenvatting in het Nederlands)

**PROEFSCHRIFT**

**TER VERKRIJGING VAN DE GRAAD VAN DOCTOR  
AAN DE UNIVERSITEIT UTRECHT  
OP GEZAG VAN DE RECTOR MAGNIFICUS, PROF. DR J.A. VAN GINKEL  
INGEVOLGE HET BESLUIT VAN HET COLLEGE VAN DEKANEN  
IN HET OPENBAAR TE VERDEDIGEN  
OP WOENSDAG 27 NOVEMBER 1996 DES VOORMIDDAGS TE 10.30 UUR**

**DOOR**

**MARTINUS LOUIS PASSIER**

Geboren op 13 mei 1969 te Bergen op Zoom

Promotor: Prof. Dr R.K. Snieder  
Department of Geophysics, Utrecht University,  
Utrecht, Netherlands.

The research described in this thesis (Chapters 2 through 5) was carried out at the Department of Geophysics, Utrecht University, Budapestlaan 4, PO Box 80.021, 3508 TA Utrecht, The Netherlands.

The work described in Chapter 6 was done at the Department of Earth, Atmospheric, and Planetary Sciences, Massachusetts Institute of Technology, Cambridge MA 02139, USA.

This research was partly supported by the Netherlands Organization for Scientific Research (NWO) through the PIONEER project PGS 76-144 and also by NATO through the Collaborative Research Grant #951225. This is Geodynamics Research Institute (Utrecht University) contribution 96.029.

*The world had to be round.  
If it was any other shape  
none of us wouldn't be here on it.*

---

*Woody Guthrie, 1946*

*Voor Tiny en Louis*

# Contents

<b>1</b>	<b>Introduction and summary</b>	<b>11</b>
<b>2</b>	<b>On the presence of intermediate-scale heterogeneity in the upper mantle</b>	<b>17</b>
2.1	Introduction . . . . .	18
2.2	Power spectra . . . . .	20
2.2.1	Spectra of earth models . . . . .	22
2.2.2	Explanations for the discrepancy . . . . .	25
2.3	Surface-wave multipathing . . . . .	33
2.3.1	Data and processing . . . . .	33
2.3.2	Extension to higher frequencies . . . . .	40
2.4	Synthetic experiments . . . . .	41
2.4.1	Models . . . . .	43
2.4.2	Synthetic spectra . . . . .	43
2.4.3	Results of ray tracing . . . . .	44
2.5	Convergence of models . . . . .	52
2.6	Conclusions and discussion . . . . .	53
<b>3</b>	<b>Using differential waveform data to retrieve local shear velocity structure or path-averaged shear velocity gradients</b>	<b>55</b>
3.1	Introduction . . . . .	56
3.2	Method . . . . .	57
3.2.1	Fundamental mode data . . . . .	57
3.2.2	Including higher modes . . . . .	61
3.2.3	Reparameterization . . . . .	63
3.3	Practical limitations . . . . .	65
3.4	Inversions of synthetic data . . . . .	67
3.4.1	Noise-free data . . . . .	70

3.4.2	Effects of noise . . . . .	75
3.4.3	Influence of variation in crustal thickness . . . . .	78
3.5	Real data examples . . . . .	81
3.6	Conclusions . . . . .	90
<b>4</b>	<b>Correlation between shear-wave upper mantle structure and tectonic surface expressions: application to central and southern Germany</b>	<b>93</b>
4.1	Introduction . . . . .	94
4.2	Method and Data . . . . .	96
4.3	Model . . . . .	102
4.4	Interpretation . . . . .	107
4.4.1	Eastern Part . . . . .	109
4.4.2	Western Part . . . . .	110
4.5	Conclusions . . . . .	113
<b>5</b>	<b>A possible interpretation of high shear-wave velocities beneath Bavaria, southern Germany</b>	<b>115</b>
5.1	Introduction . . . . .	116
5.2	Alpine history . . . . .	118
5.3	Suggested alternative scenario . . . . .	121
5.3.1	Temperature . . . . .	123
5.3.2	Composition . . . . .	127
5.3.3	Gravity . . . . .	128
5.4	Discussion . . . . .	133
<b>6</b>	<b>Surface wave waveform inversions to test shear-wave velocities under eastern Australia</b>	<b>135</b>
6.1	Introduction . . . . .	136
6.2	Method and data . . . . .	140
6.3	Results . . . . .	143
6.3.1	Case I . . . . .	144
6.3.2	Case II . . . . .	149
6.4	Conclusions . . . . .	152
<b>A</b>	<b>Ray tracing on a sphere</b>	<b>153</b>
	<b>References</b>	<b>157</b>



<b>Samenvatting in het Nederlands (Summary in Dutch)</b>	<b>172</b>
<b>Acknowledgments</b>	<b>178</b>
<b>Curriculum Vitae</b>	<b>180</b>

# Chapter 1

## Introduction and summary

Seismology can be defined as the mathematical and physical study of earthquakes. It is also the study of how the earth's vibrations, generated by earthquakes, can be used to make statements about the internal structure of the earth. Part of the seismological community focuses its attention on the mechanism of the source. The aims are to unravel the characteristics of the rupture process, in time as well as in space, and to come to a statistical description of the temporal and spatial distribution of earthquakes. Another group of seismologists is concerned with the propagation of the energy which is released when an earthquake occurs. This energy propagates along the surface (surface waves) and through the interior of the earth (body waves). This field of seismology is occupied with the description of the wavefield and the effects on the wavefield caused by heterogeneous earth structure along the propagation path.

A major goal for most seismologists is to determine the internal structure of the earth. Attempts to achieve this goal are made by using the registrations of the propagating energy released by earthquakes. Inferences about the earth structure can be made by either forward modeling or inverse modeling. Forward modeling means that the observable effects at the earth's surface of a specific structure in the earth on the propagating energy are modeled. The modeling result is then compared with the observed data. Inverse modeling uses the observed data as starting point and attempts to find in a systematic way the earth model that fits the data best. In seismology, inverse methods are often used to construct models of the seismic velocity in the earth's mantle and crust by using data which consist of travel times, if body waves are considered, or of dispersion measurements, if the data are provided by surface waves.

The development of seismology in general, and the construction via inverse methods of tomographic models down to depths of several hundred kilometers in particular, has benefitted tremendously from the rapidly increasing capacity and availability of computer facilities and data sets over the last few decades. Various three-dimensional models of the global seismic velocity distributions in the earth's mantle are nowadays available, as well as a set of regional velocity models of the mantle in regions such as Europe and the Mediterranean area, the Tibetan area, Antarctica, North America, the southern part of Brazil, etc. For the major part of the globe, however, no regional models have been developed. Due to the limited spatial occurrence of seismic events and recording networks it is also not very likely that a substantial part of the globe will be covered by regional models in the near future. An important difference between global and regional models is the length-scale of the structures that are imaged. The global models display structures on much larger scales than the regional models. There are several factors, such as limited resolution (path coverage) and regularization of the inversion procedure in combination with the integral, and therefore low-pass, character of the data, that cause the small-scale structure to be present in the inversion results in a less pronounced way than the larger structures. A similarity between the global and regional models is the amplitude of the imaged velocity anomalies with respect to a spherically symmetric reference model. In both cases, these anomalies are in the order of a few percent.

In present-day geophysics the global tomographic models are frequently used to establish a relationship between seismological images of the earth's mantle and the character of mantle convection. The dimensions of the velocity anomalies in the global seismological models are even used to actually constrain the nature of mantle convection. In doing so, it is implicitly assumed that the global models provide an adequate and complete description of mantle heterogeneity and that it is justified to neglect the smaller-scale structure, which is visible in regional models, when considering the whole globe. Chapter 2 addresses the question whether it is allowed to think that the earth's mantle is dominated by large-scale features or whether the existence of smaller-scale structure should also be acknowledged on a global scale. The length-scale of mantle heterogeneity is not only important with respect to mantle convection, but also other geodynamic processes strongly depend on the length-scale of mantle heterogeneity, since the gradients in the mantle structure are the driving forces behind these dynamic processes. In Chapter 2, a diagnostic is considered which depends on the gradient of earth structure rather than on the integral. This diagnostic is based on the concept of multipathing. Multipathing means that the lateral heterogeneities in the upper mantle cause the surface waves

to propagate along paths that deviate from the great circle between the source and receiver. The different paths between source and receiver result in a recording at the receiver position which is an interference between different arrivals from different directions. This will cause some frequencies to interfere constructively, whereas other frequencies will cancel out. As a result the amplitude spectrum of the surface waves will show peaks (positive interference) and notches (negative interference). With increasing propagation distance the multipathing effects will be stronger and the amplitude spectra will show more peaks and notches. It can be expected that a medium dominated by large-scale structure causes less severe multipathing than a medium with more energy at intermediate- and smaller-scale structure, because in a medium with smaller structure the gradients are stronger and therefore the deviations from the great circle path are larger. In Chapter 2, the amplitude spectra of long-period surface waves (between 60 and 360 s) are analyzed and the multipathing effects are compared with the effects predicted by the existing global models and by some synthetically generated models with more power at intermediate wavelengths than is the case in the global models. The conclusion is that the real earth should contain more power at the intermediate-scale structure than is currently modeled by the global models. Consequently, it is not allowed to neglect, on a global scale, the structures with length-scales as visible in the regional models.

In Chapter 3, a method is developed and tested to map gradients and smaller wavelengths more accurately. It uses the surface wave waveforms originating from one event and recorded in two stations which are located close to each other. The differences in the waveforms are inverted for local laterally homogeneous  $S$  velocity structure or for path-averaged horizontal  $S$  velocity gradients. In the first case the stations are situated on the same great circle to the source. Because the two stations are located close to each other, the propagation distance is small, which leads to less averaging of smaller structures. In the second case the two stations lie at approximately the same epicentral distance, but with a slightly different azimuth. In both cases, the frequency-dependent phase differences between the two recordings are used as data for an inversion for  $S$  velocity values. Some examples with real data are shown for the second case. The examples are related to a pronounced tectonic boundary in western Eurasia: the Tornquist-Teisseyre zone. Below a depth of 80 km, a velocity contrast between 8 and 9% is found across this boundary. This velocity contrast beneath the central part of the Tornquist-Teisseyre zone is contained within a width of at most 600 km. The use of higher mode energy enhances the resolution at larger depths (down to 400 km), where a switch of the sign of the contrast is observed. These results coincide well with other models obtained for this area.

In Chapter 4, an application is presented of the alternative use of the waveform inversion method of Chapter 3, namely the case of two stations on the same great circle to the source. Fundamental mode Rayleigh waveforms in the frequency range from 20 to 100 s have been inverted to obtain a three-dimensional  $S$  velocity distribution beneath central and southern Germany. The data come from 27 teleseismic events recorded at 17 broadband stations in Germany and adjacent areas. This results in 56 paths between pairs of stations, each pair lying on the same great circle with an epicenter. The phase differences between the waveforms recorded at a pair of stations have been inverted directly for the path-averaged  $S$  velocity perturbation between the two stations. All path models were then combined into a single three-dimensional model. The most prominent features of the obtained model are (1) low velocities beneath the Eger Graben, which are an expression of the deep-reaching rift structure, (2) high velocities between 40 and 120 km depth beneath northern Bavaria, caused by an apparent thickening of the lithosphere towards the south, (3) high velocities beneath the southern Rhine Graben area (presently inactive with respect to rifting), suggesting the absence of upwelling hot mantle material, and (4) low velocities beneath the northern part of the Rhine Graben and the presently experiencing rifting northern branch of the Central European rift system, including the Rhenish Massif west of the river Rhine with the volcanic fields of the Eifel. These reduced velocities indicate a broad updoming of the lithosphere-asthenosphere boundary. The model suggests a strong correlation between upper mantle  $S$ -wave structure at depths down to 200 km and tectonic surface expressions.

The high shear-wave velocity anomaly under Bavaria, shown by the model presented in Chapter 4, may be explained as being an expression of the Alpine lithospheric root. The issue of Chapter 5 is a possible alternative explanation for this velocity anomaly. The alternative explanation is related to the Alpine history. The closure of the Piemont ocean in the Cretaceous is a process which is related to the development of the Alps and the northern foreland. It is proposed that during the closure of this ocean, the young oceanic Adriatic plate subducted horizontally in a northward direction under central Europe (lithospheric doubling). At a certain stage, which is not tightly constrained by this scenario, the subduction polarity reversed to the present-day southward subduction of the European plate [Wortel, pers. comm.]. It is put forward that the detached part of the Adriatic plate was left behind under central Europe. The young age of this part of oceanic lithosphere prevented it from sinking to larger depths. The observed high-velocity anomaly would be caused by the remnant oceanic lithosphere. In Chapter 5, the first order implications of the proposed scenario in terms of thermal, compositional and gravitational effects are investigated. It is shown that temperature effects solely

can not explain the observed seismic velocities, because the temperature contrasts are almost eliminated due to the long cooling history. It is, therefore, more likely that compositional effects, possibly in combination with small thermal effects, can explain the high velocities. It is also shown that the gravitational implications of the lithospheric doubling scenario are consistent with large-scale Bouguer anomaly observations.

In Chapter 6, the technique of Chapter 3 is used as a tool to test specific features (and their amplitudes) of a three-dimensional tomographic model. As an example, some features of a recent  $S$  velocity model of the Australian region are tested. From the data, we directly extract local measurements of the velocity structure at various locations beneath Australia. These measurements do not suffer from several problems that occur in tomographic inversions of large datasets (e.g., spatial variations in resolution, different sampling of anisotropy). Consequently, the results are an independent test of the characteristics of the three-dimensional Australian model. The local measurements obtained in Chapter 6 appear to be consistent with this model.

Summarizing, the work described in this thesis has made clear that intermediate and smaller-scale upper mantle heterogeneity is underestimated by current global seismological models. This implies that large gradients are also underestimated. Because the gradients are the driving forces behind all kinds of geodynamic processes, an adequate image of structure and gradients is desirable if one is aiming at interpreting seismological models in a geokinematic and geodynamic context. Subsequently, a method using surface waves in order to map gradients or intermediate- and small-scale upper mantle structure has been outlined, tested, and applied to develop a three-dimensional  $S$  velocity model beneath central and southern Germany down to a depth of 200 km. The method has also been used to test aspects of a model of the  $S$  velocity structure under Australia. A specific feature of the Germany model is a high-velocity anomaly beneath northern Bavaria. This has been interpreted in the light of a kinematic scenario, consisting of a paleo-subduction process. This interpretation is a tentative example of the role seismological models may play in geodynamics. To enhance the future importance of this role, seismological studies should, among other goals, continue to aim at properly imaging upper mantle structures on a small scale in the areas of geodynamic interest.

## Chapter 2

# On the presence of intermediate-scale heterogeneity in the upper mantle

**Abstract** Power spectra of tomographic models of the entire earth and of models of Europe and the Mediterranean area are compared. This comparison reveals a discrepancy (a factor 15–30) between the power of both kinds of models at intermediate spherical-harmonic degrees (around  $l = 30$ ). Two possible explanations for this discrepancy are given. First, the fact that Europe is more complex than the global average, and second, the lack of resolution in the inversions. Another approach to the problem of the power spectrum of heterogeneities of intermediate length-scale is the study of multipathing of long-period surface-waves. The multipathing observed in the recordings of these waves, which manifests itself as an increasing complexity of their amplitude spectra due to increasing interference of spectral components with increasing epicentral distance, cannot be explained by present-day global earth models. The gradients in the models are simply not strong enough. However, random models with more power at intermediate scales, and consequently stronger gradients, are able to explain the observed multipathing. It is concluded that the global models underestimate the power in the heterogeneities of intermediate-scale structure in the earth. Finally, an explanation is given why current global models, although they do not contain sufficient power at shorter scales, do explain the travel-time and dispersion data used for the construction of the models.

---

<sup>1</sup>This chapter has been published as: M.L. Passier and R.K. Snieder, 1995. On the presence of intermediate-scale heterogeneity in the upper mantle, *Geophys. J. Int.*, **123**, 817–837. (Geodynamics Research Institute (Utrecht University) publication 95.072).

## 2.1 Introduction

The aim of seismic tomography is to determine the structure of the earth's interior. From the deviations of these models from lateral homogeneous models, conclusions are derived concerning, for example, plate motion histories and lithospheric structure [e.g., *Van der Hilst et al.*, 1991; *Zhang and Tanimoto*, 1991; *Spakman et al.*, 1993; *Su et al.*, 1994]. The tomographic models can be divided into two groups. The first group, global models, consists of models of the entire earth. One of the problems concerning this group of models is that the amplitudes of the heterogeneities vary from model to model due to differences in the inversion techniques employed [*Laske et al.*, 1994]. The second group, regional models, is the group of models of only one specific area of interest, such as the Caribbean or the Mediterranean area. The main difference between the two types of models is, besides the area covered, the scale length of the mapped heterogeneous structure (Figures 2.1a and 2.1b). Both models exhibit structures with velocity perturbations of a few percent, but the length scales on which these perturbations occur differ significantly. While global models display features on the scale of continents, oceans and shields, regional models show structures on the much smaller scale of subduction zones and mountain ranges, tectonic features that are invisible in current global models. For an extensive overview of recent seismological evidence on mantle heterogeneity, the reader is referred to *Nolet et al.* [1994]. A detailed overview of seismic models of the earth's mantle can be found in *Ritzwoller and Lavelle*, [1995]. Heterogeneous structure on any scale is very important in different branches of earth science. One question still open to debate in geophysics is, for example, which characteristic scales are associated with convection. Geologists and geochemists are concerned with dynamic and structural processes which take place in the lithosphere and upper mantle. The details of these processes are closely related to the dimensions of the structure. Geochemists may be interested in scales of mantle structure, because of their relation to the mixing of isotopes [*Carlson*, 1994]. Since in geophysics conclusions about convective patterns are sometimes drawn from the power spectra of global seismological earth models [e.g., *Montagner and Tanimoto*, 1991; *Montagner*, 1994], a detailed and correct image of heterogeneous structure is desirable. A quantity used to diagnose these conclusions is the power spectrum of the global models. Some researchers [e.g., *Tanimoto*, 1991; *Zhang and Tanimoto*, 1991, 1993] reported a  $l^{-2}$  dependent decay of spectral power with harmonic degree. *Woodward and Masters* [1991] found from their analysis of *ScS-S* residuals that large-scale heterogeneity in the lowermost mantle is predominant. *Su and Dziewonski* [1991, 1992] concluded from *SS* residuals that heterogeneity in the mantle is dominated by large-scale structure. Their



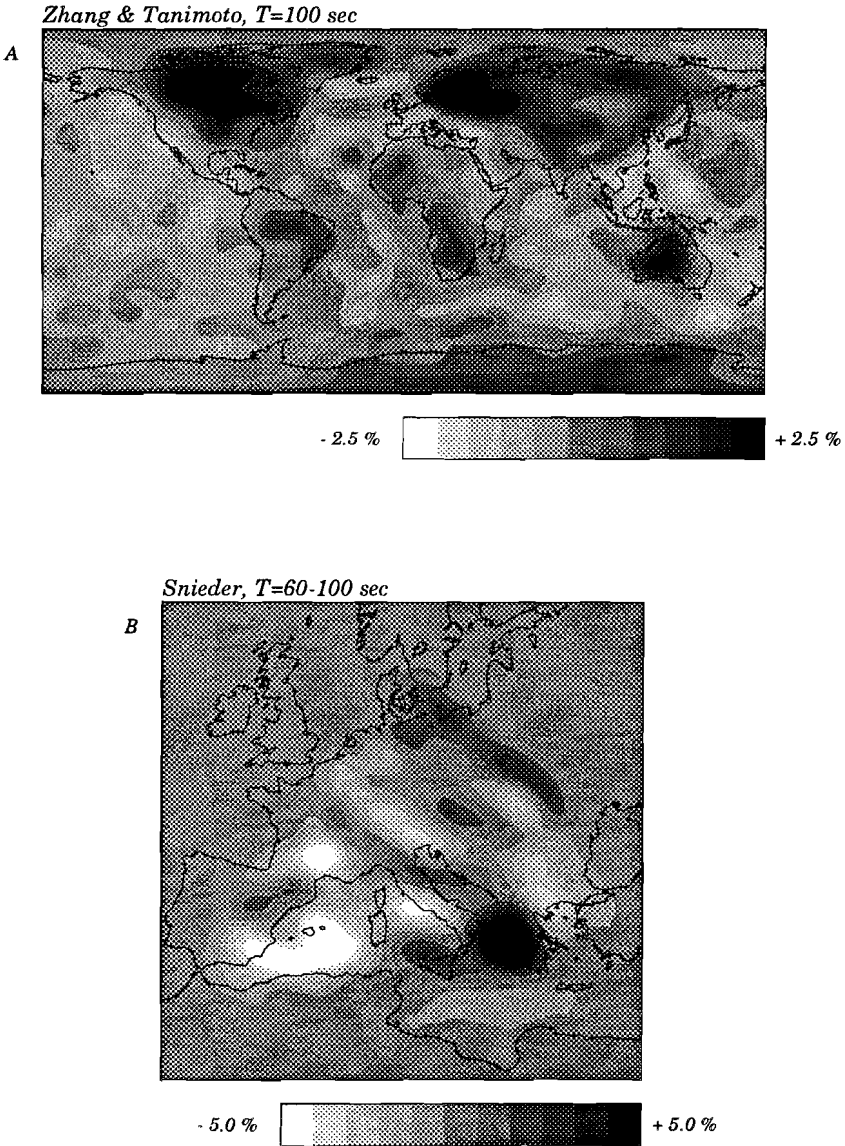


**Figure 2.1** (a) The global Rayleigh-wave phase-velocity model of Zhang & Tanimoto (1993) (ZT) and (b) the regional Rayleigh wave phase velocity model of Snieder (1988) (SNIE).

analysis revealed a decay rate of power which is less steep than  $l^{-2}$  for  $l$ -values up to 8, but which is much steeper for the higher harmonic degrees. Furthermore, they suggest that those results impose constraints on the nature of mantle convection.

The different views on the power spectrum of mantle structure can be divided into two categories. The first view [e.g., *Su and Dziewonski, 1991, 1992*] comprises a mantle in which heterogeneity is dominated by long-wavelength features. Beyond these dominant scales, structures with smaller scales are believed not to make significant contributions to the total power in the global structure. The second possibility is that one also recognizes the considerable contribution to the total global power of structure beyond the spectral range of global inversions, which is visualized in regional tomographic inversions. With respect to these regional structures, *Gudmundsson et al. [1990]* noted that the upper mantle contains strong power beyond  $l = 25$ . Since these views are contradictory, it is not possible to support them both. Either one believes that the global models provide a complete and correct description of the earth's interior, which implies that the regional models have to be considered inaccurate, or one acknowledges that significant structure is present on a regional scale.

This paper consists of two separate parts. In the first part power spectra of existing global and regional earth models are compared. From this comparison remarks are made about intermediate-scale structures in the earth. In the second part multipathing observations in long-period surface-waves are used to draw inferences about intermediate-scale earth structure.

## 2.2 Power spectra

All global, seismic-velocity perturbation fields,  $\frac{\delta v}{v}(\theta, \phi)$ , where  $v$  denotes surface-wave phase velocity or  $P$ - and  $S$ -wave velocity, were expanded in terms of spherical harmonics [e.g., *Stacey, 1992*]:

$$\frac{\delta v}{v}(\theta, \phi) = \sum_{l=0}^{\infty} \sum_{m=0}^l (a_{lm} \cos m\phi + b_{lm} \sin m\phi) p_l^m(\cos \theta) . \quad (2.1)$$

Because of the normalization condition of the  $p_l^m(\cos \theta)$ , the power of the spherical-harmonic expansion at degree  $l$  is given by

$$D_l \equiv \frac{\sum_{m=0}^l (a_{lm}^2 + b_{lm}^2)}{2l + 1} . \quad (2.2)$$

Model	$l$	$\lambda$ (km)	rms (%)
M84C (1984)	$\leq 8$	$\geq 4700$	1.4
ZT (1993)	$\leq 36$	$\geq 1100$	0.8
S12 (1994)	$\leq 12$	$\geq 3200$	1.6
POL (1994)	$\leq 16$	$\geq 2400$	1.0
GR (1994)	5–50	800–7300	1.5

**Table 2.1** Global- and intermediate-scale Rayleigh-wave models

In these terms, the power is defined as the square of the quantity that *Zhang and Tanimoto* [1991, 1993] call the amplitude for a particular harmonic degree  $l$ . In this study the power spectra of global models are compared with the power spectra of regional models. The global  $P$ -wave velocity models that were used are the model of *Inoue et al.* [1990], hereafter referred to as IFTO and the model of *Pulliam et al.* [1993], hereafter referred to as PVJ. The global Rayleigh-wave, phase-velocity models that were used (for a period of around 100 s) are the model of *Zhang and Tanimoto* [1993] (Figure 2.1a), hereafter referred to as ZT, the phase-velocity model calculated from the S12 shear-wave velocity model of *Su et al.* [1994], the phase-velocity model calculated from the M84C model of *Woodhouse and Dziewon-ski* [1984], and the model of *Pollitz* [1994], hereafter referred to as POL. In addition, the Rayleigh-wave model computed from the model of *Grand* [1994] was considered. This model covers an area smaller than the entire globe, but larger than the regional models employed in this study. This model will be denoted as GR. An overview of the Rayleigh-wave models is given in Table 2.1. The regional models that were used for comparison with the global models are the 60–100 s Rayleigh-wave, phase-velocity model of Europe of *Snieder* [1988] (hereafter referred to as SNIE, Figure 2.1b), the 100 s Rayleigh-wave, phase-velocity model calculated from the  $S$ -wave velocity distribution derived by *Zielhuis and Nolet* [1994] (hereafter referred to as ZN) and the EUR89B  $P$ -wave velocity model of the Mediterranean area by *Spakman et al.* [1993]. Only the POL, ZT, and SNIE models give perturbations directly of phase-velocity. The other models that give perturbations of  $S$ -wave velocity were transformed into relative phase-velocity models by calculating the depth integrals of the perturbations multiplied with the appropriate kernels [*Aki and Richards*, 1980]. All phase-velocity models include corrections for laterally varying crustal thickness, except the GR and the POL model. The POL model includes a correction for the

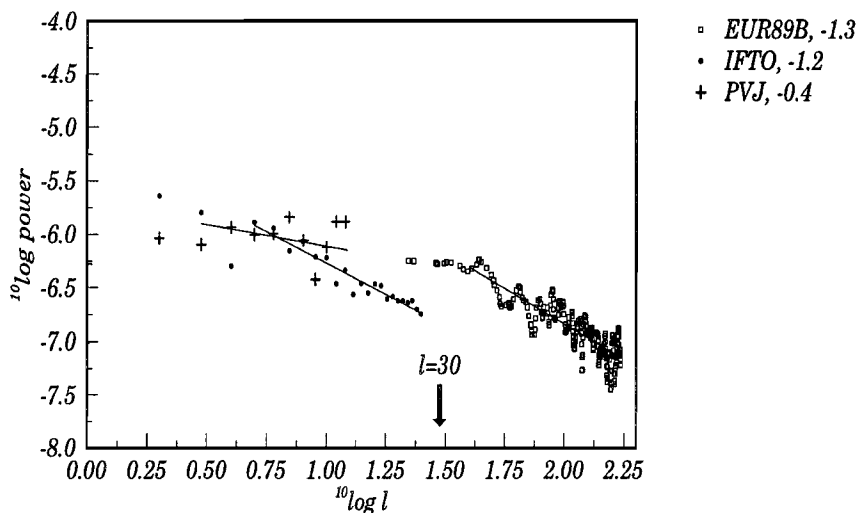


**Figure 2.2** Power spectra on a double logarithmic scale of the IFTO, PVJ, and EUR89B  $P$ -velocity models at a depth of approximately 500 km. The numbers in the legend indicate the slopes of the lines fitted through the spectra.

bending of the ray-paths and a correction for the earth's ellipticity. To obtain the spectra of the regional models a two-dimensional Fourier transform was applied to the model. In the wavenumber domain, the  $k_x, k_y$ -plane, power belonging to identical  $k$ -values ( $k^2 = k_x^2 + k_y^2$ ) was summed. The wavenumber was mapped into harmonic degree  $l$  according to  $ka = l + \frac{1}{2}$ , where  $a$  is the earth's radius [Aki and Richards, 1980]. Both the global and the regional power spectra were normalized to a unit surface area so that the spectra can be compared directly. In the normalization of EUR89B, ZN and SNIE only the regions with good resolution were taken into account.

### 2.2.1 Spectra of earth models

Figure 2.2 shows on a double logarithmic scale the power spectra of the  $P$ -wave velocity models PVJ, IFTO, and EUR89B at a depth of approximately 500 km. The pattern of decaying power spectra (and also the rates of decay) with harmonic degree  $l$  is characteristic of all depths. Note that the PVJ model decays less rapidly than both other models. The observation of the discrepancy of a factor of about 3 between the power spectra of the EUR89B model and the IFTO model around

$l = 30$  is also characteristic of all depths. Figure 2.3a reveals the power spectra for the ZT, M84C, POL, GR, S12, SNIE, and ZN phase-velocity models. As in Figure 2.2, the power spectra decay with increasing harmonic degree  $l$  and a discrepancy between the global and the regional models occurs around  $l = 30$ . Both decay and discrepancy, which are the features that we will focus the attention on in this section, are observed for the models that have been corrected for crustal thickness as well as for the models that do not include these corrections. All models decay at a rate of approximately  $l^{-2}$ , except the S12 model, which decays faster. At low harmonic degrees, the amplitudes of the S12 and M84C model are larger than the amplitudes of the other models. Also *Su et al.* [1992] pointed out the major differences in amplitude between the ZT model and the S12 model. As *Pollitz* [1994] already mentioned, at shorter wavelengths his model, POL, contains more power than the ZT model. The GR model is comparable to the POL model for  $l < 16$ , and for higher  $l$ -values it continues to exhibit significantly larger amplitudes than the ZT model. The discrepancy at intermediate wavenumbers ( $l \approx 30$ ) between the power in the ZT model and the regional models is a factor of about 30, but the discrepancy between the GR model, and perhaps also the POL model, and the regional models is considerably smaller (a discrepancy of factor 10–15). The close resemblance of the spectra of the SNIE model and the ZN model is interesting as the models were derived using different methods and different data. The phase-velocity models of Figure 2.3a have a faster decay with harmonic degree  $l$  than the  $S$ -wave velocity models. This is illustrated in Figure 2.3b where phase velocity and single-layer  $S$ -velocity spectra are compared for the global ZT model and the regional ZN model. The fact that the spectrum of the layer of the Zielhuis  $S$ -velocity model at 200 km depth lies under the spectrum of the Zielhuis phase-velocity model is a result only of the fact that the layer at 200 km depth exhibits less pronounced inhomogeneities than the phase-velocity model. The steeper slopes for the phase-velocity models may be attributed to the fact that the phase-velocity perturbation is a depth integral of the structure and therefore averages out the structures with smaller length scales.

The actual shape of the power spectra is controlled by several factors besides the earth structure itself. Errors in the data and numerical precision of the computation facilities limit the scale of resolvable structure. The lack of resolution (limitations in the ray coverage) and the inversion regularization applied (damping) lead to an underestimation of the highest-wavenumber components in earth structure which causes an artificially enhanced decay of the power spectra. All these factors may contribute to the size of the discrepancy at intermediate wavenumbers. The difference in the size of the discrepancy around  $l = 30$  for the  $P$ -velocity (Figure 2.2)

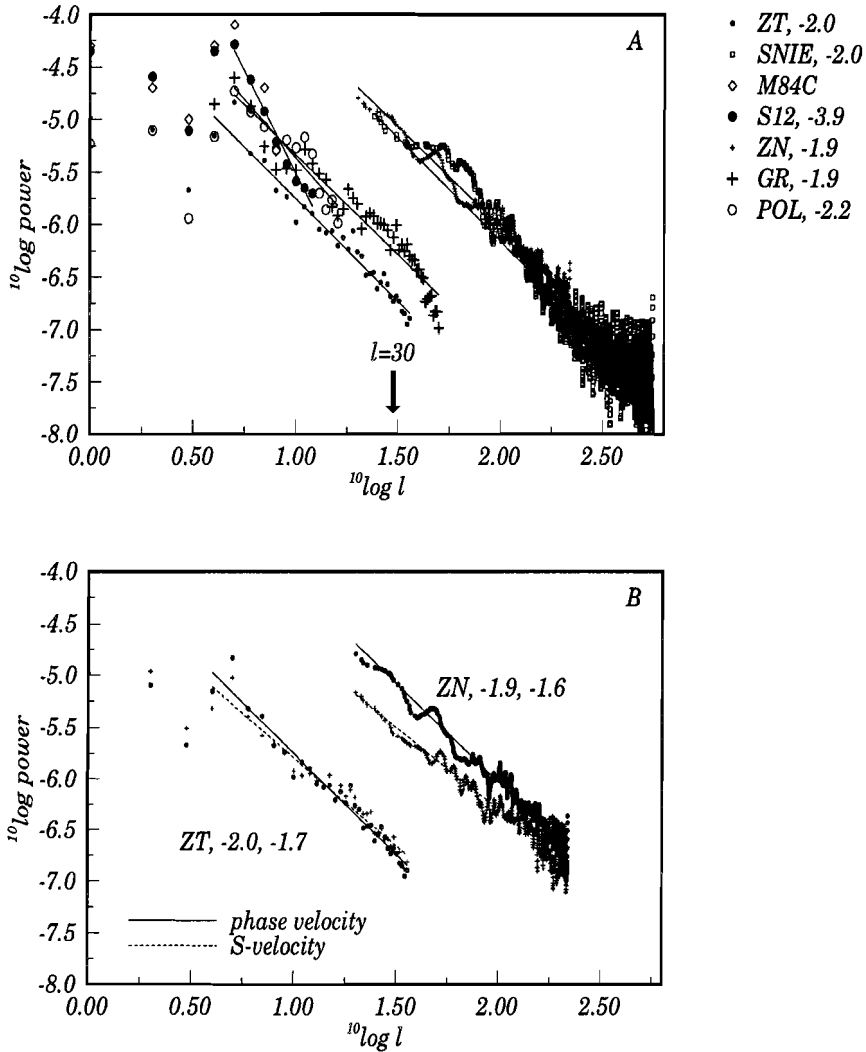


**Figure 2.3** Power spectra on a double logarithmic scale of (a) the ZT, M84C, S12, GR, POL, SNIE, and ZN Rayleigh-wave phase-velocity models (all at a period of approximately 100 s), and (b) the ZT phase-velocity model (dots) and the single layer of the ZT S-velocity model at 210 km (crosses) and the ZN phase-velocity model (dots) and the single layer of the ZN S-velocity model at 200 km (crosses). The numbers in the legend indicate the slopes of the lines fitted through the spectra. For M84C no decay rate is given, because the model only contains  $l \leq 8$ . Note in (b) the faster decay for the phase-velocities than for the S-velocities.

and the surface-wave phase-velocity (Figure 2.3a) may in part be due to differences in the parameters that control the spectral decay in the individual inversions. The power spectra, as presented in Figures 2.3a and 2.3b raise a question. It is obvious that the power in a certain harmonic component of the true earth structure should not depend on the scale on which one examines the earth. Figure 2.3a, however, shows two different values for the power belonging to structures on scales around 600 km ( $l = 30$ ), depending on whether the earth is studied on a global scale or on a regional scale. The problem which will be considered in the following section is whether the global and regional models are contradictory or not.

## 2.2.2 Explanations for the discrepancy

Two possible reasons for the discrepancy between the global and the regional models in Figure 2.3a will now be discussed in more detail. First, the extent to which the discrepancy at intermediate wavenumbers could be explained by the tectonic complexity of Europe, which is greater than the global average complexity, will be investigated. Second, a synthetic example will be presented which shows that the qualitative features of the comparison of the global and the regional spectra (decay, discrepancy at intermediate wavenumber) can be explained by a limited resolution in the inversion.

Figure 2.4a shows the ZT phase-velocity model in the region of the ZN phase-velocity model. Figure 2.4b shows the ZN model band-pass filtered between harmonic degree 20 and 36. These intermediate wavenumbers are present in both models. The ZT model and the ZN model have both been corrected for crustal thickness variations, allowing a direct and fair comparison. The ZT model does not resolve the low velocities under southern Europe, and the velocity contrast across the Tornquist-Teisseyre zone is much better resolved in the ZN model. The rms perturbation of the ZT model in this region is 1.4%. The rms perturbation of the filtered ZN model in the same region is 2.7%. The discrepancy in power is therefore a factor  $(2.7/1.4)^2 = 3.7$ . This is a considerable reduction of the factor 30 obtained from the comparison of the entire ZT model with the ZN model. The reduction reflects the situation of Europe being more complex than the global average. Given the uncertainty in the calibration of tomographic models, the difference of the factor  $2.7/1.4 = 1.9$  implies that the discrepancy between the results of global and regional studies can to a large extent be explained by the fact that Europe and the Mediterranean are more complex than the global average.

On the other hand, a finite ray coverage leads in general to tomographic images in which the smallest scales are most poorly resolved. This could explain the dis-

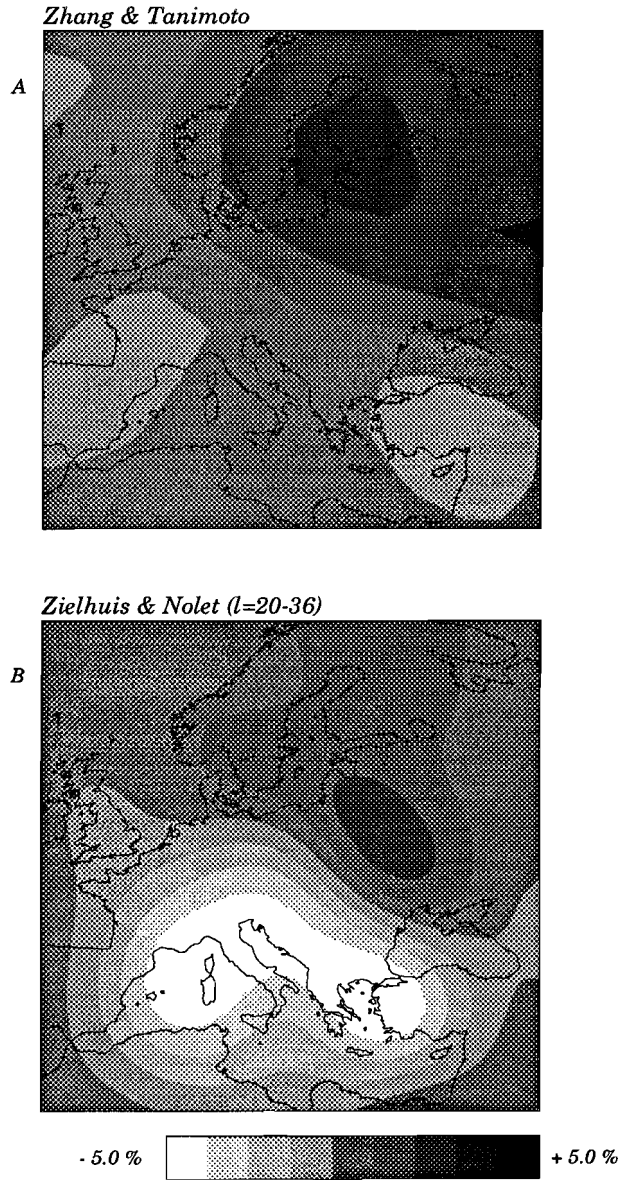


**Figure 2.4** (a) The ZT model for Europe. (b) The filtered ( $20 \leq l \leq 36$ ) ZN model for the same area.



crepancy in the power spectra of the global and regional models shown in Figure 2.3a. This is illustrated with the following experiment. A one-dimensional model of length unity, which represents a primitive analogue of the earth's structure, was sampled in two different ways. In order to simulate an inversion for a global model the model was integrated over 100 randomly chosen intervals with lengths that followed a Gaussian distribution with mean 0.8. The random intervals were uniformly distributed over the total interval from 0 to 1 with a wrap around the end of the interval, if needed. To simulate an inversion for a regional model, 725 integrals of the model were calculated over uniformly distributed intervals with lengths that followed a Gaussian distribution with mean 0.3. These numbers of data used in the "global" as well as in the "regional" inversions are much smaller than what is required for an accurately reconstructed model, because in the following examples the sampled models were defined by 1000 one-dimensional basis functions, for which a Fourier series was chosen, whereas inversions were carried out for a maximum of 725 data points. If there is significant power at small scales, this simulates the situation which also occurs in inversions for real earth structure. Note that the particular choice of these numbers of data is not really important. They are only chosen this way to reflect the difference in qualitative features of inversions on a global and on a regional scale: longer paths and a less dense ray coverage for global inversions and shorter paths and a denser coverage for regional inversions. This does not critically affect the conclusions as the examples will only be interpreted qualitatively rather than quantitatively. The model was integrated to yield the data, because the current seismological models are also derived from data that are integrals of earth structure; travel times, for example, are slowness integrals. The one-dimensional model used for the regional inversion was a high-passed version of the random model to avoid spectral leakage [Snieder *et al.*, 1991] from the lower frequencies into the regional model. Spectral leakage from the higher frequencies in the case of the "global" inversion turned out to be negligible. In the case of the "global" inversion the 100 integral data were inverted to obtain the coefficients of the 40 lowest basis functions ( $l \leq 20$ , where  $l$  is the number of wavelengths fitting between 0 and 1) and for the simulation of the "regional" inversion the 725 integral data were inverted for the coefficients of 290 higher basis functions ( $15 \leq l < 160$ ). In both inversions the ratio of the number of data to the number of model parameters is thus the same. The first model that was sampled was a  $\delta$ -pulse (Figure 2.5a). The reconstructed models can be regarded as the resolution kernels and are shown in Figures 2.5b and 2.5c. Due to the insufficient path coverage the inversion results are broader than the original  $\delta$ -pulse and side-lobes appear. This spatial smearing is also observed in real tomographic inversions (e.g. the resolution tests in Spakman *et al.* [1993]).

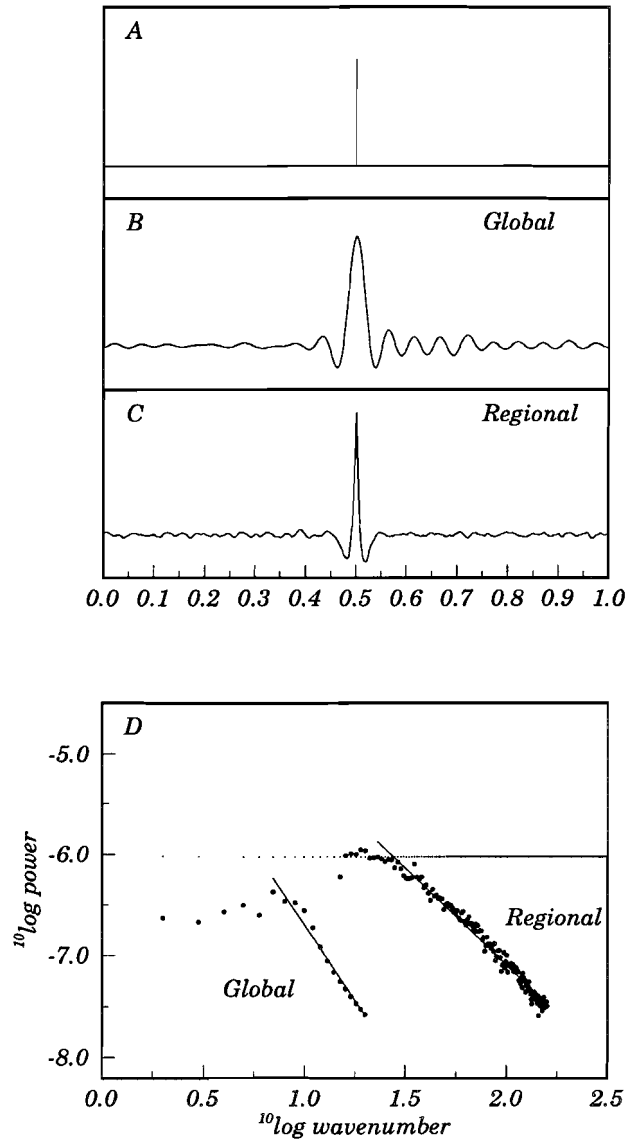


**Figure 2.5** (a) The  $\delta$ -pulse as input model in the synthetic inversion experiment. (b) The global resolution kernel. (c) The regional resolution kernel. (d) The power spectra of the models of (b) and (c) (heavy dots) and of the true model of (a) (light dots).

The spectra of the one-dimensional resolution kernels are shown in Figure 2.5d. These power spectra decay with harmonic degree,  $l$ , and show a discrepancy around the intermediate wavenumbers. The second model that was sampled consists of a realization of white random noise (Figure 2.6a). The models resulting from the inversions and their spectra are shown in Figures 2.6b, 2.6c and 2.6d. Figure 2.6d reveals that a structure originally with a white spectrum is imaged after inversion to a model with a decaying spectrum. The obtained spectra (Figures 2.5d and 2.6d) exhibit the same characteristics as the spectra of existing earth models in Figure 2.3a, including the discrepancy around the connecting wavenumbers.

In linear damped least-squares inversion, which is the same type of inversion with which existing models have been derived, the largest eigenvalues are associated with eigenvectors with dominant power at lower frequencies, whereas the smallest eigenvalues are associated with eigenvectors that contain dominant power at higher frequencies. This is illustrated with the black squares in Figure 2.7, which shows the power in the eigenvectors for the largest (Figure 2.7a) and the smallest eigenvalue (Figure 2.7b) for the case of the synthetic global inversion of Figure 2.6. A similar pattern for the power in the eigenvectors was observed for the synthetic regional inversion. This behaviour is due to the fact that path integration is a low-pass operation and that as a result the high-wavenumber components in the model have little effect on the synthetic data. There are two important factors that control the decay of the power spectra of the reconstructed models. The path coverage is limited, which leads to a blurring in the inversion and an underestimation of the high-wavenumber components. This is aggravated by the fact that the data are integrals of the model. Since integration is a low-pass operation this leads to an additional underestimation of the higher-wavenumber components. Once again, it is emphasized that the synthetic examples are not designed to simulate quantitatively their real counterparts. However, qualitative features (decay, discrepancy at intermediate wavenumber) are simulated and explained, indicating that the discrepancy between the global and regional power spectra in Figure 2.3a could very well be an artefact from the tomographic reconstruction technique employed. This would imply that the power in the higher wavenumbers in the global models is underestimated. In a similar way the power in the highest wavenumbers of the regional models may be underestimated.

The synthetic inversion experiment described above was repeated twice, once with the data being point samples of the model in Figure 2.6a and once with point samples of the derivative of that model as data. In the former case, the spectra of the model estimates were flat, similar to the flat spectrum of the initial model. The power in the eigenvectors was uniformly distributed over all wavenumbers (the

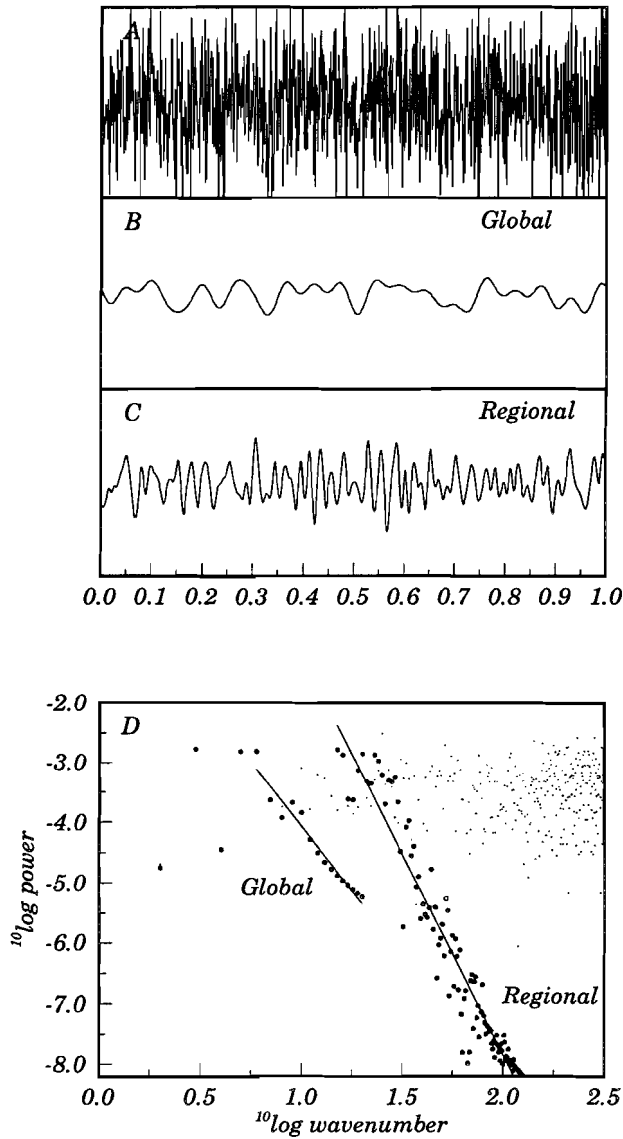


**Figure 2.6** (a) The random one-dimensional model used in the synthetic inversion experiment. (b) The global model obtained after inversion. (c) The regional model obtained after inversion. (d) The power spectra of the models of (b) and (c) (heavy dots) and of the true model of (a) (light dots).

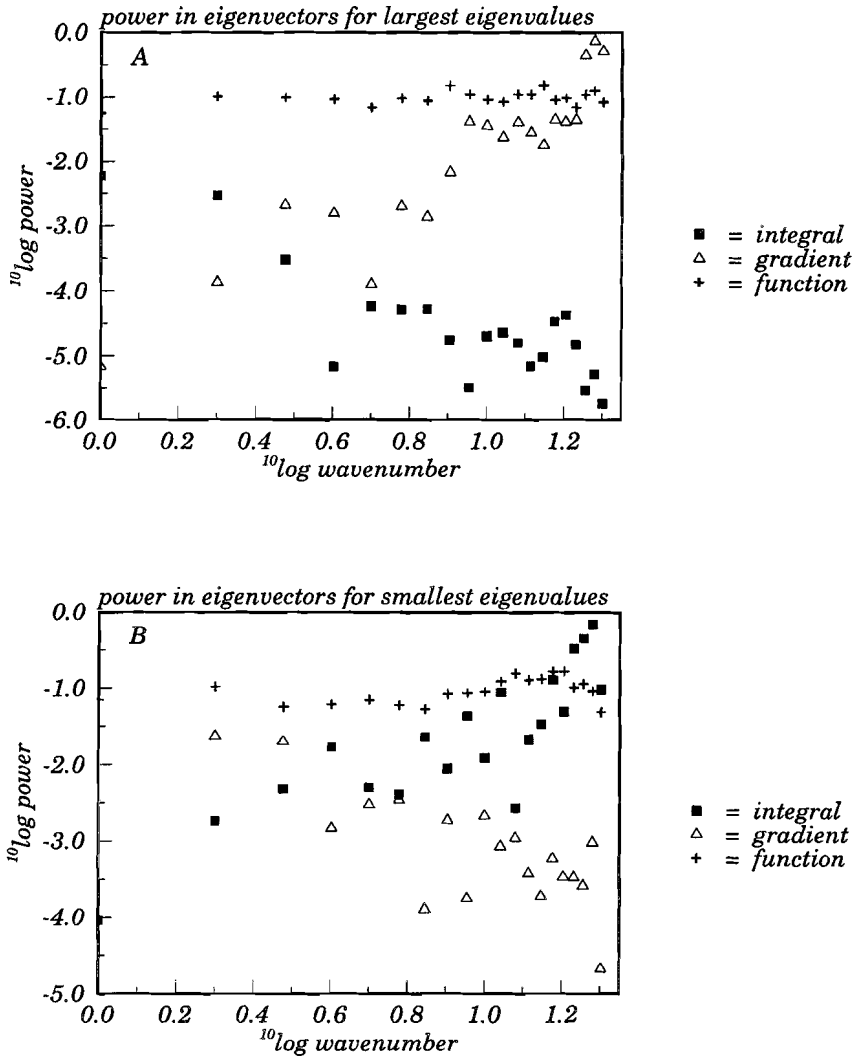


**Figure 2.7** Power in the eigenvectors belonging to (a) the largest eigenvalues and (b) the smallest eigenvalues for the three cases of the synthetic global inversion where the data for the inversion are integrals of the model (solid squares), the model itself (plus signs), and gradients (open triangles) of the model.

plus symbols in Figure 2.7). As a result, no particular wavenumber range was dominantly imaged in the inversion. In the latter case, the spectra of the model estimates exhibited an opposite trend compared to the original case where the data were integrals of the model. The power in the inversion results increased with increasing wavenumber and the power in the eigenvector belonging to the largest eigenvalue was dominated by the higher wavenumbers (the triangles in Figure 2.7a). The dominant power in the eigenvector for the smallest eigenvalue was present at the lower wavenumbers (the triangles in Figure 2.7b). This reflects the fact that the gradient is a high-pass operator. Therefore, inversions based on a limited data set would lead to models in which the high-wavenumber components are overestimated if the model were constructed on the basis of data that depend on gradients of the earth's structure. In other words, if gradient-dependent data are used, the power spectra of the reconstructed models increase with harmonic degree,  $l$ , if the path coverage is insufficient. For a complete data set and data that are not contaminated with errors, one would expect that the model could be reconstructed accurately, regardless of the way in which the data sample the model. It is clear from the discussion and the examples that the artefacts in the power spectra of the reconstructed models depend in a complicated way on the way in which the data sample the model and the fact that the data set is finite. It is not possible to give general rules for the artefacts in the reconstructed models, because these artefacts depend critically on the data and the regularization employed.

From the comparison between global and regional models and their power spectra (Figures 2.1–2.4) a question has been raised concerning the power at intermediate wavenumbers. At these scales, a discrepancy is observed between the global models and the regional models: the regional models exhibit more power than the global models. Two possible candidate explanations for this discrepancy were tested in further detail. The fact that Europe is more complex than the global average explained the size of the discrepancy up to a factor of 2 in amplitude. On the other hand, the qualitative features observed in the power spectra of existing earth models could be explained by a synthetic test simulating the role of finite ray coverage (limited resolution) in the inversion. In the next section a different approach will be used to investigate the issue of the power spectrum in the intermediate-wavenumber range. In this approach diagnostics derived from long-period, surface-wave data are considered. These data do not depend on integrals of the earth structure, but depend on a different property of the structure: the velocity gradient.

## 2.3 Surface-wave multipathing

In this section the fundamental-mode, Rayleigh-wave  $R_1$ ,  $R_2$ ,  $R_3$  and  $R_4$  arrivals in the period range between  $T = 60$  s and  $T = 360$  s are considered.  $R_1$  and  $R_2$  wave trains are the minor and major arc arrivals respectively.  $R_3$  and  $R_4$  leave the source in the same direction as  $R_1$  and  $R_2$ , respectively, but orbit the earth one more time before being recorded at a station. In a laterally homogeneous earth these waves will travel from the source to the receiver along the great-circle path. However, in the presence of lateral heterogeneities, horizontal gradients cause energy to refract away from the great-circle path. As a result, energy may take more than one path from source to receiver. This phenomenon is called surface-wave multipathing. Multipathing will manifest itself as constructive or destructive interference of the different frequency components of several wave trains arriving simultaneously at a station. As a longer path will yield more multipathing than a shorter path [White *et al.*, 1988], this will lead to amplitude spectra that are smoother for shorter distances ( $R_1$ ) and spectra that show more peaks and notches for larger propagation distances ( $R_4$ ). Increasing complexity of amplitude spectra with propagation distance is also alluded to by Romanowicz [1994]. In a homogeneous medium without multipathing the shape of the amplitude spectrum for a fixed azimuth is only influenced by anelastic damping, which causes a smooth exponential decay of the amplitude with increasing frequency. Therefore amplitude spectra of surface-waves can be used as a diagnostic which is sensitive to gradients (and consequently also length scales) of earth structure.

### 2.3.1 Data and processing

Long-period, vertical-component records sampled continuously at 1 sample per 10 s recorded by the GEOSCOPE network [Romanowicz *et al.*, 1991] were used. The events we chose are at shallow depths and have high surface-wave magnitudes. This ensures effective generation of fundamental-mode surface-waves. The four events and their characteristics are listed in Table 2.2. Table 2.3 lists the station locations and the event-station combinations that were used. A plus sign implies that a given recording was used. Recordings of events were rejected if, after band-pass filtering the signal between 60 and 360 s (the frequency range considered in this study), the signal-to-noise ratio was found to be too low to be able to distinguish the surface-wave arrivals from the rest of the signal by eye.

Each Rayleigh wave train was submitted to a frequency-domain time-variable filtering procedure [Landisman *et al.*, 1969]. With this procedure contributions from

Event	Date	Origin Time, UT	Lat	Lon	Depth, km	$M_s$
Chile	88/01/19	0730:31.9	24.7° S	70.6° W	33	6.7
Kamchatka	88/02/29	0531:41.4	55.2° N	167.4° E	33	6.8
Aroe	88/07/25	0646:06.6	6.11° S	133.7° E	28	6.7
Solomon	88/08/10	0438:26.1	10.4° S	160.8° E	34	7.4

**Table 2.2** *List of events used*

overtone could be removed and overlapping parts of arrivals (for example the tail of the  $R_3$  arrival and the beginning of the  $R_4$  arrival) could be separated. The frequency-dependent time windows used in the procedure were determined using the group velocity predicted by the PREM model [Dziewonski and Anderson, 1981] and had a length of approximately three times the period. In this way, overlapping parts of arrivals were only separated if the station was situated far enough away from the antipodal caustic ( $R_1$  interfering with  $R_2$  and  $R_3$  with  $R_4$ ) and the source caustic ( $R_2$  interfering with  $R_3$ ). At and near the caustics the interfering arrivals were not separated. The filtered wave trains were Fourier transformed and corrected for anelastic damping effects. This was done by multiplying the spectra with [Aki and Richards, 1980]:

$$S_c = S_{obs} \exp \left( \frac{\omega x}{2U(\omega)Q(\omega)} \right), \quad (2.3)$$

with  $S_c$  the corrected spectrum,  $S_{obs}$  the observed, uncorrected spectrum,  $\omega$  the angular frequency,  $x$  propagation distance,  $U(\omega)$  the group velocity, and  $Q(\omega)$  the attenuation for the fundamental mode according to the PREM model. It is important to note that the attenuation correction is a smooth function of frequency. The effect of the correction on the spectral complexity is therefore negligible compared to the effects of multipathing.

Due to anelastic damping the high frequencies will be less pronounced in the seismic signal at larger propagation distances. Noise, however, will still be present at the higher frequencies. When observed amplitude spectra are corrected for anelastic damping with (2.3), noise as well as true seismic signal is amplified. To investigate the potential contaminating effects of noise a synthetic experiment was performed, in which noise was added to a synthetic seismogram containing  $R_1$ ,  $R_2$ ,  $R_3$  and  $R_4$  fundamental mode arrivals according to the PREM model. As epicentral distance



Station	Lat	Lon	Chile	Kamchatka	Aroe	Solomon
RER	21.2° S	55.8° E				+
NOU	22.1° S	166.3° E			+	+
SSB	45.3° N	4.5° E		+	+	+
SCZ	36.6° N	121.4° W	+	+		+
CAN	35.3° S	149.0° E	+	+	+	+
PAF	49.4° S	70.2° E		+	+	+
TAM	22.8° N	5.5° E	+	+		
DRV	66.7° S	140.0° E		+	+	+
PPT	17.6° S	149.6° W	+	+	+	+
INU	35.4° N	137.0° E	+	+	+	+
CAY	4.9° N	52.32° W		+	+	+
CRZF	46.4° S	51.9° E	+		+	+
MBO	14.4° N	16.9° W	+		+	+
BNG	4.4° N	18.6° E	+			
KIP	21.4° N	158.0° W			+	+
HDC2	10.0° N	84.1° W			+	+

Table 2.3 Event-station combinations

the characteristic distance of an  $R_1$  arrival,  $90^\circ$ , was chosen. The experiment was carried out in order to find up to which frequency the corrected amplitude spectrum showed energy associated with surface-wave propagation and above which frequency the spectrum was strongly contaminated by noise. Frequencies for which the amplitudes were too much contaminated by noise were then excluded from later analyses. The added noise was constructed by convolving white noise with a part of the recording of the Kamchatka event at station INU. This part did not contain any fundamental mode arrival, so the entire energy content could be regarded as noise for our purposes. The amplitude of the noise was chosen to correspond with the average amplitude of the real seismograms outside the time windows with the surface-wave arrivals. The noisy synthetic signal was submitted to the processing procedure outlined above. By comparing the noise-free amplitude spectra and the noisy amplitude spectra it was concluded that for the  $R_1$  arrival the entire frequency band between 60 and 360 s could be used. All high frequencies could be reconstructed without significant distortion of the original noise-free spectrum. For

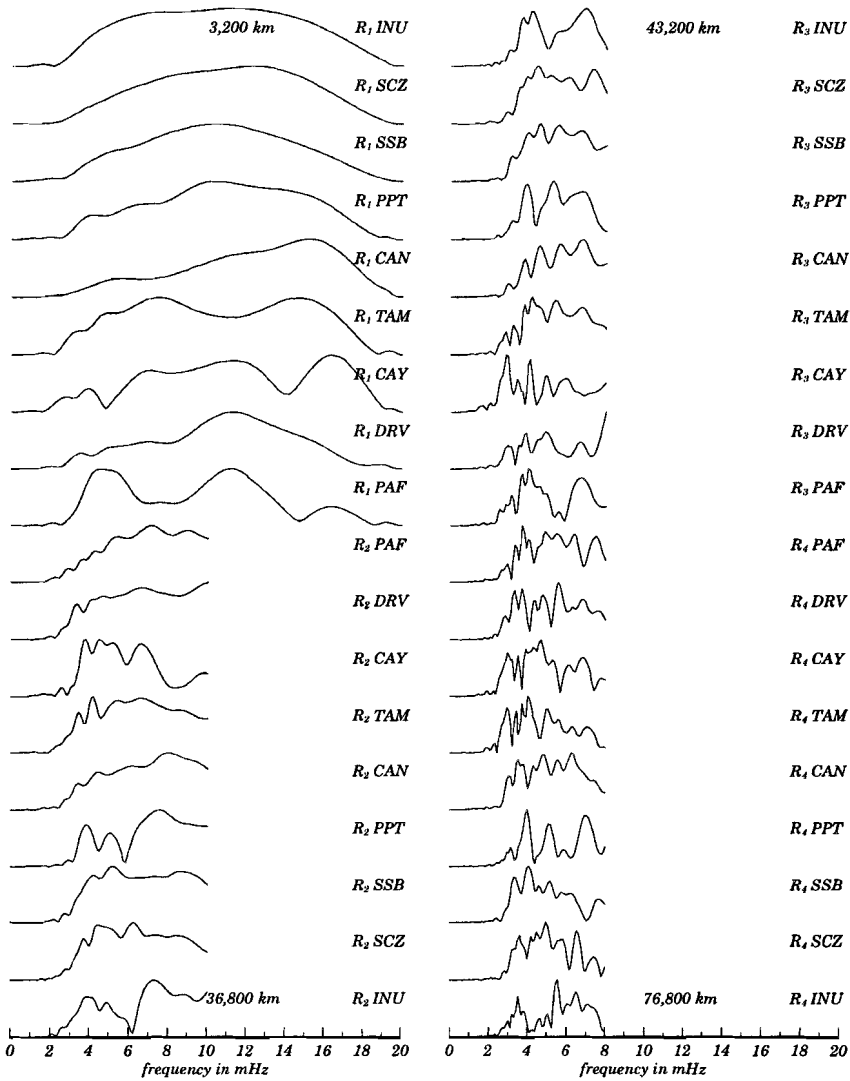
the  $R_2$  spectra the energy for periods shorter than 100 s could not be reconstructed properly. For the  $R_3$  and  $R_4$  spectra the range of useful frequencies was limited to periods longer than 125 s. The frequency bounds are based on subjective qualitative criteria. Because they are chosen in a conservative way, we expect the bounds can be applied to real data.

Figure 2.8 shows the amplitude spectra for the Kamchatka event. The spectra are characteristic of all spectra of the four events used in this study. For the higher orbits the frequency range in which contamination by noise can be expected is omitted. The spectra are arranged in order of increasing propagation distance. The spectra are normalized by their peak amplitude. Since we are only interested in the complexity of the spectra, their absolute amplitude is not relevant. It is clear that the complexity of the amplitude spectra increases with increasing propagation distance. They are smoother at short distances ( $R_1$ ) and show more peaks and notches at larger distances ( $R_4$ ). This behaviour is not always visible if two or three spectra are considered at stations with epicentral distances that do not differ by much. However, by considering the whole picture a trend of increasing complexity is clear. An increasing complexity is also evident if the subsequent amplitude spectra for a single station, e.g. TAM, are considered. In the absence of multipathing the spectra for different arrivals at a single station should have the same shape (after correction for attenuation). It follows from Figure 2.8 that this is clearly not the case.

To analyze the increasing spectral complexity with increasing propagation distance it has to be quantified by some measure. The number we introduce here to measure the spectral complexity will be called the peak-index. The peak-index  $P$  of a one-dimensional function  $f(\omega)$  is defined by

$$P(f) = \frac{1}{L} \int \frac{|\partial_{\omega\omega} f|}{|f| + \epsilon} d\omega , \quad (2.4)$$

where  $L$  is the total length of the interval over which the peak-index is determined and  $\partial_{\omega\omega} f$  is the second derivative of  $f(\omega)$  with respect to the variable  $\omega$ , which can be considered as frequency. The small number  $\epsilon$  prevents a division by zero. The peak-index is designed to measure the roughness of functions in the interval of interest. The basic idea behind this way of quantifying the complexity of a spectrum is illustrated if  $\epsilon$  is set equal to zero (generally,  $\epsilon$  will not be set equal to zero but to a small number, for instance, 5% of the average absolute value of  $f(\omega)$ ) and the peak-index of  $\sin(n\omega)$  is computed.  $P(\sin(n\omega)) = n^2$ : the peak-index grows as the square of the coefficient  $n$  that determines the oscillation in the function  $f(\omega)$ . Functions that vary strongly with frequency ( $\omega$ ) have high peak-index values,



**Figure 2.8** Amplitude spectra for the  $R_1$ ,  $R_2$ ,  $R_3$  and  $R_4$  arrivals of the Kamchatka event. Only relevant parts of the spectra are shown (see text). The spectra are arranged in order of increasing propagation distance and all spectra are normalized to the same level.

whereas functions with smooth  $\omega$ -dependence have low peak-index values. For a line (which is the zero frequency component if it is a horizontal line) the peak-index is nil. Note also that for a function  $f(\omega) = \exp(-\alpha|\omega|)$ , the peak-index is given by  $P(\exp(-\alpha|\omega|)) = \alpha^2$ . A sharply peaked exponential (large  $\alpha$ ) leads to a larger peak-index than a more gently decaying exponential (small  $\alpha$ ).

Figure 2.9 shows the peak-indices, as calculated over the relevant frequency intervals (this means the entire frequency range for the  $R_1$  arrivals, frequencies up to 10 mHz for  $R_2$  arrivals and frequencies up to 8 mHz for  $R_3$  and  $R_4$  arrivals), from the spectra of the Kamchatka event of Figure 2.8, as well as those for the other three events. Considering the expression for the peak-index (2.4) it is clear that the vertical scaling of the amplitude spectra in Figure 2.8 does not affect the value of  $P(f)$  (for small  $\epsilon$ ). The peak-indices shown here can be regarded as a diagnostic for multipathing caused by the gradients present in the real earth. In agreement with visual inspection of the amplitude spectra (Figure 2.8), the peak-index increases with increasing epicentral distance for all four events. The order of magnitude of the peak-indices is the same for all four events. This implies that the sampling of the globe by our data is wide enough so that we can regard the results presented in Figure 2.9 as generic characterizations of earth structure. If an earth with a uniform distribution of heterogeneous structure is assumed, the same amount of multipathing for arbitrarily chosen source-receiver configurations would be expected. Obviously, that leads to the same order of magnitude of the peak-indices. Although the absolute values are of the same order, there is substantial scatter about the empirical curves fitted for each event, but the visual differences are not believed to be truly significant. For example, if Figure 2.9b and Figure 2.9d are compared (the Chile and the Solomon event) differences are clear. This may be due to the fact that different rays sample different parts of the globe. Although the earth is sampled in a global fashion, the medium sampled by individual paths can differ significantly.

An unexpected feature, also observed in Figure 2.9, can be seen around the antipodal caustics (where  $R_1$  interferes with  $R_2$  and  $R_3$  with  $R_4$ ) and source caustics (where  $R_2$  interferes with  $R_3$ ) indicated by the vertical dashed lines in Figure 2.9. From a ray theoretical point of view, energy is expected to arrive almost simultaneously at these caustics from all azimuths. Considerable interference would then occur, the amplitude spectra would be complex and peak-indices would take large values. However, the peak-index values around these caustics in Figure 2.9 do not evidently show such an anomalous behaviour. This may be due to the fact that although many wave trains may arrive at the caustics, the differences in travel times may be small, which will not lead to an extraordinary complexity of the amplitude

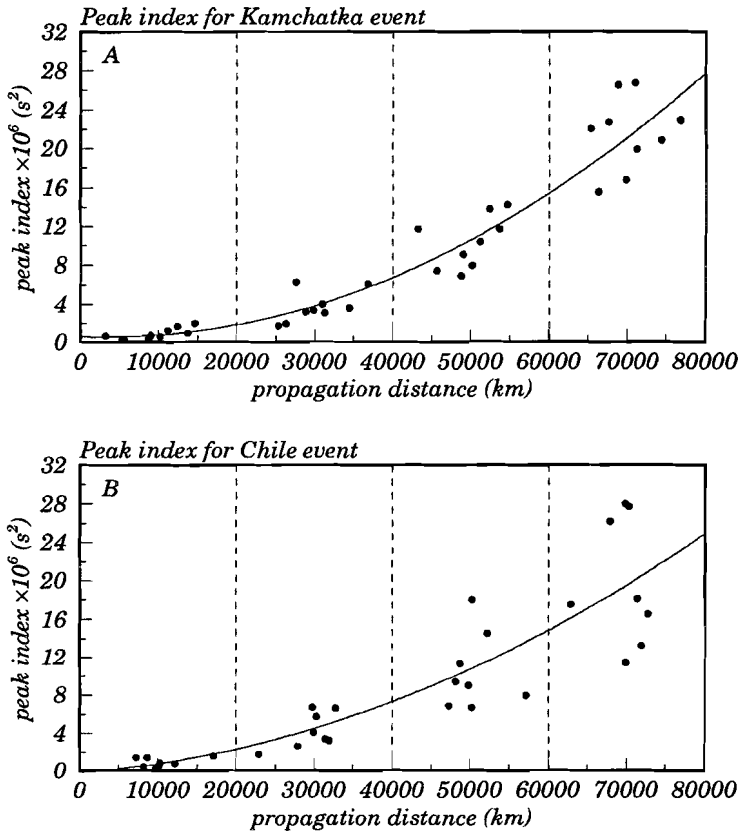


**Figure 2.9** Peak-index as calculated for the relevant parts of the amplitude spectra of the recordings of (a) the Kamchatka event (see also Figure 2.8), (b) the Chile event, (c) the Aroe event and (d) the Solomon event. The vertical dashed lines indicate the boundaries between the  $R_1$ ,  $R_2$ ,  $R_3$  and  $R_4$  domains. The data points are fitted with parabolas.

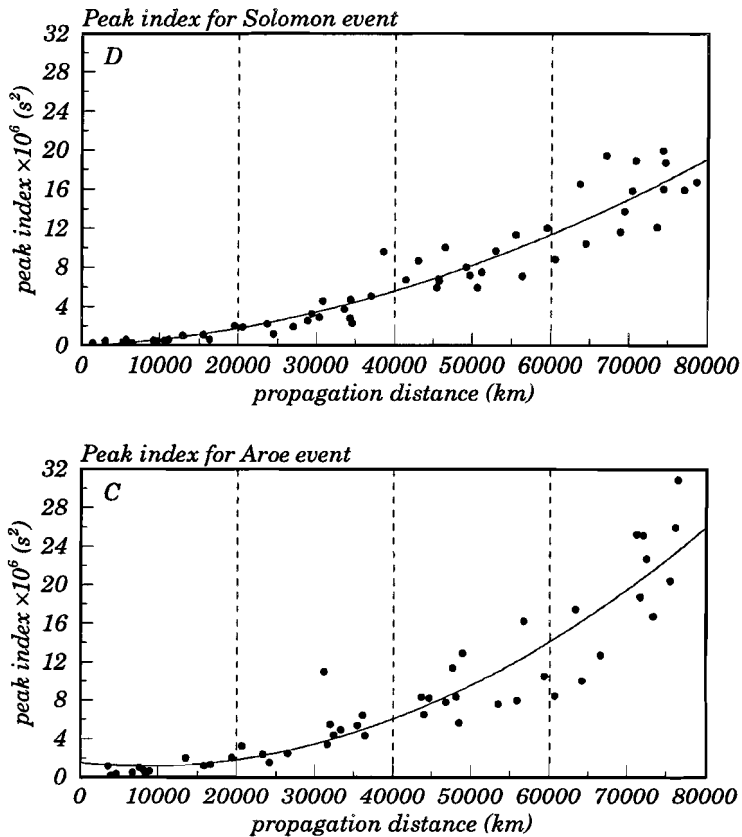


Figure 2.9 (continued).

spectrum.

### 2.3.2 Extension to higher frequencies

The data shown up to this point are the fundamental mode long-period Rayleigh wave arrivals. The propagation distances range up to about 80,000 km. It was demonstrated that multipathing on this scale manifests itself in increasing spectral complexity. One question that arises is whether this behaviour can also be found on a smaller scale if the frequencies are higher and if the propagation distances are shorter. To investigate this, an event in Guinea, Western Africa was examined (Dec. 22, 1983, origin time 04:11:29.2 UTC, epicentre  $11.95^\circ$  N,  $13.61^\circ$  W, depth 10 km.,

$M_s = 6.2$ ). The vertical component of the fundamental-mode Rayleigh wave of only  $R_1$  arrivals was considered. The event was recorded at seven stations of the NARS array [Nolet *et al.*, 1986a]. This broadband array was aligned along a great-circle from Scandinavia to Southern Spain. The epicentre of the Guinea event was located southward on the same great-circle. This leads to an ideal situation for comparing amplitude spectra because all the paths leave the source in the same direction. Therefore, there are no differences in the amplitude spectra caused by azimuth-dependent radiation factors. Following the same procedures as in the previous section, a variable filtering technique was applied to the data, again with group velocities according to the PREM model, but now between periods of 10 and 100 s. After filtering the amplitude spectra were corrected for anelastic damping using (2.3) with  $U(\omega)$  and  $Q(\omega)$  according to PREM. Figure 2.10a shows the amplitude spectra after this treatment. From top to bottom the normalized spectra are arranged in order of increasing epicentral distance. Note the difference in frequency content in comparison with the GEOSCOPE data (Figure 2.8), which contain frequencies up to 20 mHz, whereas the NARS recordings range up to 100 mHz. The entire frequency band was used to calculate peak-indices without rejecting any high frequency energy. The results are shown in Figure 2.10b. Two remarks can be made about this figure. First, there is again an increasing trend in the peak-index with increasing epicentral distance, indicating increasing multipathing. Second, the order of magnitude of the peak-indices is the same as the order of magnitude that was observed for the GEOSCOPE  $R_1$  arrivals for the same propagation distance (a peak-index of the order  $10^6 \text{s}^2$  for a propagation distance of several thousands of kilometers). This indicates that multipathing effects on high frequencies sensitive to shallow parts of the upper mantle and crust are similar to multipathing effects on lower frequencies sensitive to deeper areas.

## 2.4 Synthetic experiments

It is interesting to check whether the observed pattern of spectral complexity (and the related multipathing) can be retrieved for different existing earth models and for random, synthetic earth models. To investigate this, several synthetic experiments were performed, which were basically carried out in two steps. The first step consisted of tracing rays through a phase-velocity model (existing or random) and in the second step the ray configurations obtained were used to compute synthetic amplitude spectra for different propagation distances.

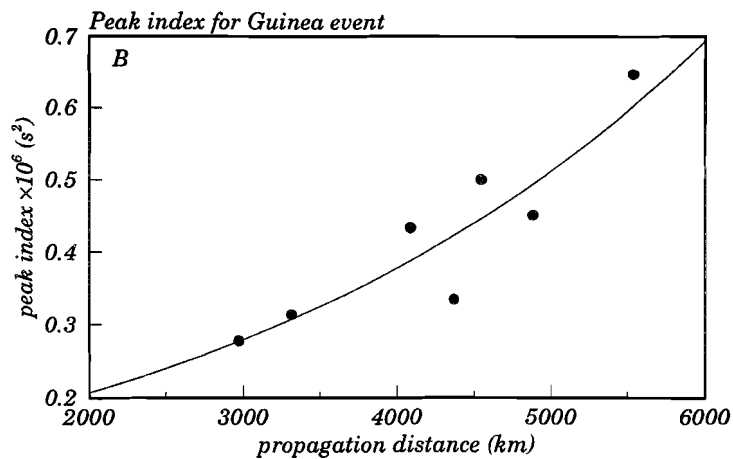
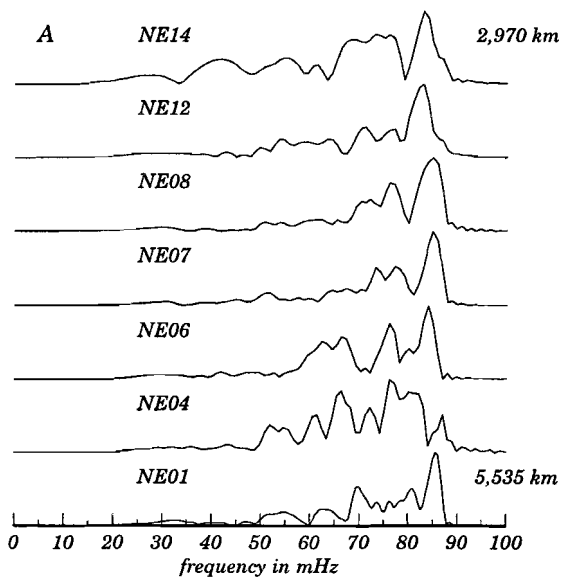


**Figure 2.10** (a) Amplitude spectra with increasing propagation distance and (b) the peak-indices for the recordings of the Guinea event recorded by NARS stations.



### 2.4.1 Models

The global models that were considered are the phase-velocity models used in the first part of this paper (for the power spectra of earth models, see also Table 2.1). The random models were expanded in spherical harmonics following definition (2.1). With a random number generator the coefficients  $a_{lm}$  and  $b_{lm}$  were chosen randomly. For each value of  $l$ , the coefficients  $a_{lm}$  and  $b_{lm}$  were normalized in such a way that the power spectrum as defined by (2.2) had the desired shape. Prescribing the shape of the power spectrum is a way to introduce characteristic length scales in the random model. A spectrum with most of the power at low harmonic degrees will result in longer characteristic length scales than a power spectrum which has the majority of its power at the higher harmonic degrees. The scaled coefficients were used to calculate the spherical harmonic expansion using (2.1). A simple scaling of the resultant  $\delta c/c$  field yielded the desired rms value of the perturbation. Note that a harmonic expansion (2.1) extends to infinite harmonic degrees, but for practical purposes the expansion has to be truncated at some level,  $l_{max}$ .

### 2.4.2 Synthetic spectra

The existing global models as well as the random models are defined on a sphere. The velocities were transformed using equation (A.2) in appendix A. The rays were traced through these transformed models using equations (A.1) in appendix A. With the ray configurations obtained by ray tracing synthetic amplitude spectra were computed. To construct spectra several ingredients were needed. In the experiments the source and five stations were located on the equator at epicentral distances of  $30^\circ$ ,  $60^\circ$ ,  $90^\circ$ ,  $120^\circ$  and  $150^\circ$ . For each station the seismogram  $s(t)$  was decomposed into a finite number,  $n$ , of wave trains,  $w$ , according to

$$s(t) = \sum_{i=1}^n A_i w(t - t_i) .$$

Each wave train corresponds to a ray geometrical arrival with an independent amplitude,  $A_i$ , and time delay,  $t_i$ . The problem is to determine, for each station, the number of arrivals, their amplitudes and their travel times. The determination of these quantities is discussed in appendix A. The reference wavelet was computed according to the PREM reference model along the equator and for the proper propagation distance. For example, if the  $R_1$  propagation distance is  $30^\circ$ , the reference wavelet for the  $R_3$  arrival was computed for a propagation distance of  $390^\circ$ . The phase velocity models through which the rays are traced are computed for a fixed

period. However, in the procedure outlined above all frequencies propagate through that same model for the phase-velocity perturbation. This is based on the assumption that characteristic length scales of the models do not differ much for the different periods. Since only the complexity of the amplitude spectra is modeled, rather than the details of the waveforms, this approach is a simple tool to describe the effect of multipathing on amplitude spectra.

For computational convenience the source was situated on the equator and the Greenwich meridian ( $\theta = 90^\circ$  and  $\phi = 0^\circ$ ), but this is not important, because the equator was arbitrarily aligned in the different simulations. According to ray theory [Woodhouse and Wong, 1986] or higher-order asymptotic theory [Romanowicz, 1987], the direction in which heterogeneous structure is traversed determines whether surface-wave energy is focused or defocused. Suppose that for some source-receiver configuration energy is focused at the receiver. If the source and receiver are reversed, the energy would travel in exactly the opposite direction and the energy is defocused at the receiver [Romanowicz, 1987, 1990]. This means that for example  $R_2$  and  $R_3$  experience opposite focusing effects, because large parts of their paths cross the same area but in opposite direction. Actually, a pattern of alternating high and low amplitude trains on the seismogram is often observed [Lay and Kanamori, 1985]. By shooting two bundles of rays from the source (one bundle of rays left the source in an eastward direction yielding  $R_1$  and  $R_3$  arrivals and one bundle was shot in the westward direction to obtain the  $R_2$  and  $R_4$  arrivals) possible focusing and defocusing effects were automatically included in the analysis.

### 2.4.3 Results of ray tracing

After ray tracing through the existing earth models and computing the synthetic frequency spectra, peak-indices were computed. In Figure 2.11 only the peak-indices for the ZT model are shown. The other models (Table 2.1, except GR, which is not a global model) yielded similar peak-indices. From Figure 2.11 it is obvious that the peak-indices, which would be the observed multipathing diagnostics if the earth were similar to one of the global models in Table 2.1, do not match the peak-index for the observed long-period surface-waves. For the global models only one arrival was found for each station, except for the longest  $R_4$  propagation path, which yielded three or four arrivals. Consequently, no multipathing and therefore no spectral complexity was modeled. This failure of existing global earth models to account for the observed complexity of amplitude spectra of surface waves should be interpreted as a lack of power in the higher-wavenumber components of these models. The gradients in lateral heterogeneity, as present in the real earth, must

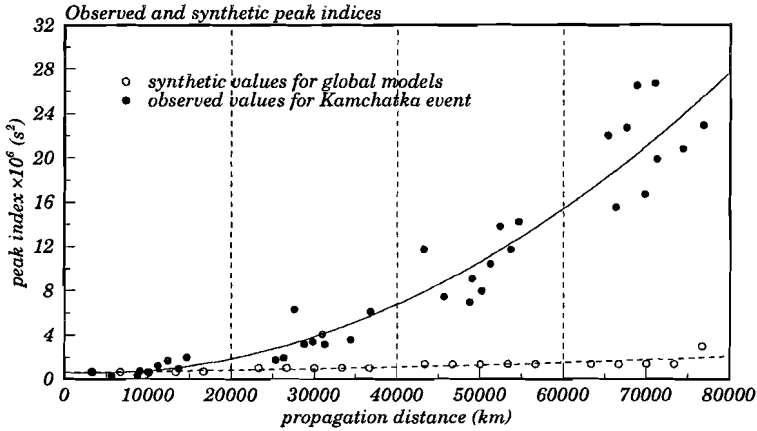


**Figure 2.11** Observed peak-indices of the Kamchatka event (solid circles) and synthetically computed peak-indices (open circles) for the ZT model, both fitted with parabolas. The other global models resulted in a similar pattern for the peak-index.

be underestimated by the current global earth models. *Romanowicz* [1987] came to the same conclusion based on the observation that anomalous amplitudes of  $R_2$  and  $R_3$  could not be explained by the M84C model.

As noted earlier, the power in most global models decays with harmonic degree,  $l$ , as  $l^{-2}$ . In the remainder of this section several scenarios for the power spectra are tested which contain more power at the high harmonic degrees. Figure 2.3a displays the power spectra of global and regional earth models. The two most important features of these spectra are the decaying character with harmonic degree,  $l$ , and the discrepancies around  $l = 30$ . The four power spectra that are tested in this section are based on the observations of Figure 2.3a and are displayed in Figure 2.12. Case I assumes a flat spectrum at low harmonic degrees and a decaying part,  $l^{-2}$ , at high harmonic degrees. This corresponds to the assumption that the  $l^{-2}$  decay of the global spectra is an artefact of the inversion, but that the  $l^{-2}$  decay of the regional spectra is accurate. Case II assumes a flat spectrum for the entire range of harmonic degrees. In this scenario it is assumed that the  $l^{-2}$  decay of both the regional and global spectra is an artefact of the inversion. Case III assumes a decay as  $l^{-2}$  over all harmonic degrees without a truncation at intermediate wavenumbers. Case IV represents a scenario only for a global model which decays as  $l^{-1}$ . Note that all these scenarios imply more power at shorter scales than the global models with an

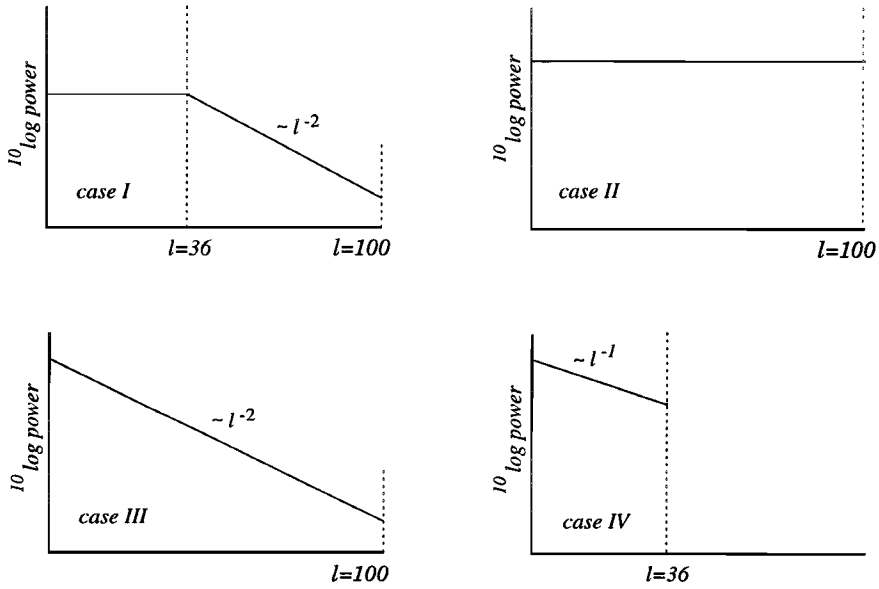


**Figure 2.12** The power spectra for the experiments with random models.

$l^{-2}$  decay. Figure 2.13 shows the velocity fields generated according to the different power spectra. It is important to note that the phase of the different spherical harmonic components of the random models used in this study is random, whereas the phase of the spherical harmonic components of the real global models is not. In the existing models, tectonic and topographic features, such as oceans and continents or shields, can therefore be distinguished. It is not quite clear what the influence of this phase correlation in the global models is on the spectral complexity of surface-waves. To investigate this, the following experiment was carried out. A random model was constructed with a power spectrum up to  $l = 36$  and decaying as  $l^{-2}$ . This model yielded the same result as the existing models (which have non-random phase), namely no multipathing. From this it can be concluded that the discrepancy between the observed multipathing and the multipathing computed for the existing models is not affected by the phase correlation in the global models.

The experiments were carried out with rms perturbations of the different random models between 0.5 % and 2.5%. The results discussed below (obtained with an rms perturbation of 1%) are characteristic for this range of perturbation values, since the peak-indices obtained did not vary much over this range of rms perturbations.

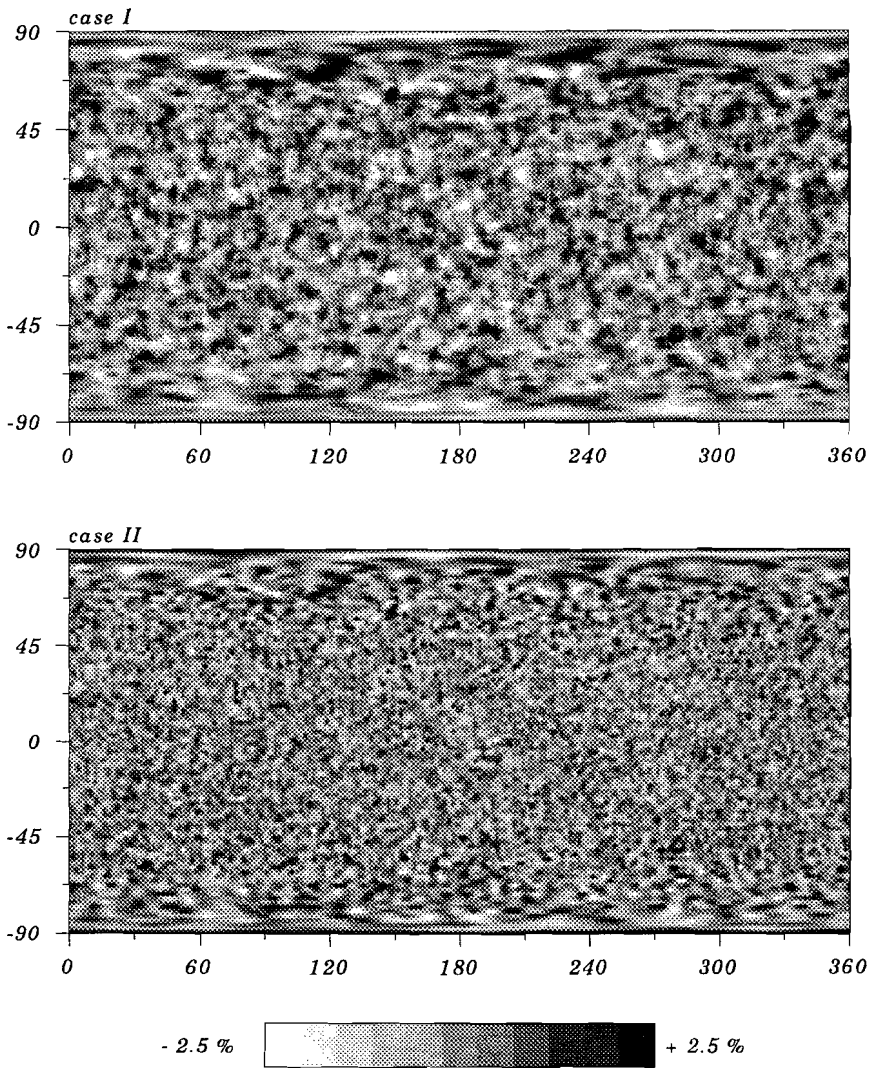


**Figure 2.13** Generated random models belonging to the different scenarios for the power spectra as shown in Figure 2.12.

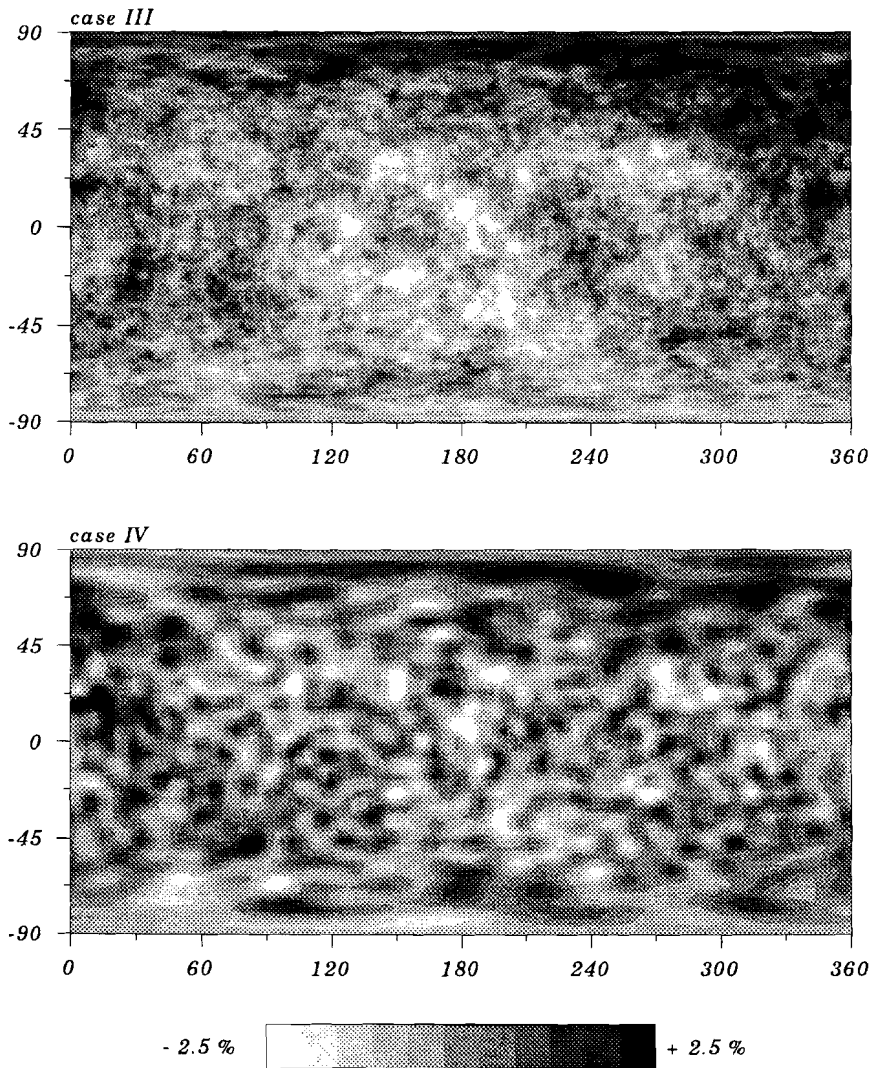


**Figure 2.13** (continued).

In case I and case III more than 95% of the total power is contained within the harmonic degrees lower than 36. This means that extrapolations of the power spectra to structures beyond the resolution limit of global models do not involve large enhancements of the rms levels of the global models. Therefore, the order of magnitude of the rms perturbations employed is in agreement with the rms levels observed in global models (Table 2.1). In case II 36% of the total power is contained within the harmonic degrees lower than 36. Hence, for a total rms level of a little more than 2% the rms perturbation of the “global part” of the random model ( $l \leq 36$ ) is around 0.8%. Although this comes close to the ZT model and the POL model (Table 2.1), it may be an underestimation of the true level in the earth. Figures 2.14a and 2.14b show the synthetic peak-indices for case I and case III, both in comparison with the peak-indices for the Kamchatka event. The results for case II were almost identical to those for case I and are therefore not shown. It is clear that a model with a power spectrum which decays over all  $l$ -values as  $l^{-2}$  and with an rms level up to 2.5% is not able to explain the observed multipathing, as the synthetically determined peak-indices are significantly lower than the observed ones (Figure 2.14b). However, a model with a spectrum as case I, approaches the observed values quite well (Figure 2.14a). The difference in the level of the peak-indices between case I and case III is directly reflected in the observed number of arrivals. For case I the number of arrivals ranged up to about 40 for the longest propagation paths but for case III not more than 15 arrivals were found.

The higher harmonic degrees up to  $l = 100$  do not contribute very much to the amount of global multipathing and therefore to the values of the peak-indices. This can be concluded from two observations. The first observation is that the power spectra of case I and case II are similar for the lower harmonic degrees ( $l \leq 36$ ) and differ for the higher degrees ( $l > 36$ ), but lead to similar multipathing effects. Thus the difference between the power spectra at higher harmonic degrees does not manifest itself in a difference in multipathing effects. The second observation is that a model with a case III spectrum cannot account for the observed amount of multipathing. The high harmonic degrees ( $l > 36$ ) added to the decaying spectrum ( $l^{-2}$ ) do not provide the additional power necessary to give rise to substantial multipathing. The reason why the higher harmonic degrees play a relatively unimportant role could be that very small-scale perturbations mainly cause small jitters in the ray paths rather than organized additional stationary phase arrivals. In addition, one should realize that for large harmonic degrees one cannot really justify using a ray geometrical treatment of the surface waves since the wavelengths of the surface waves are no longer small compared to the wavelengths of the heterogeneity.

Figure 2.14c shows the computed peak-index for a random model according to

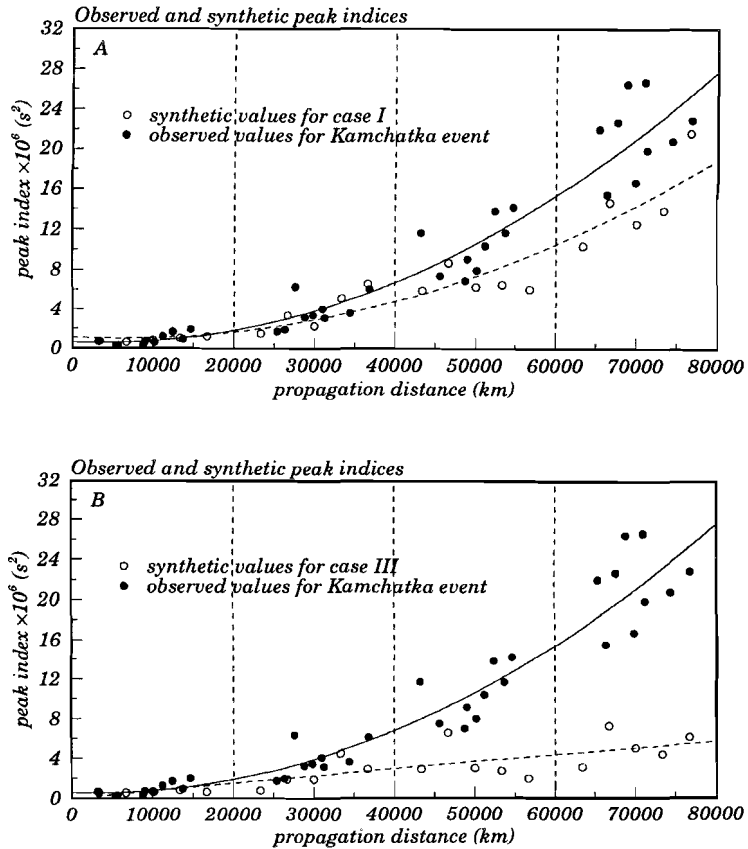


**Figure 2.14** Observed peak-indices of the Kamchatka event (solid circles) compared with the peak-indices as computed for the random models (open circles) belonging to the power spectra of (a) case I, (b) case III, and (c) case IV. All data points are fitted with parabolas.



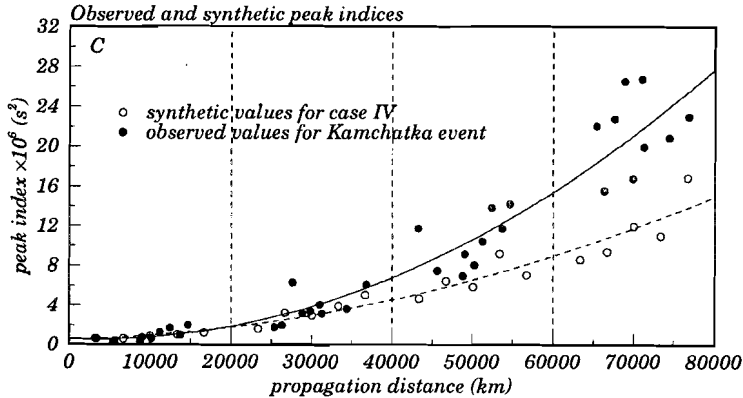
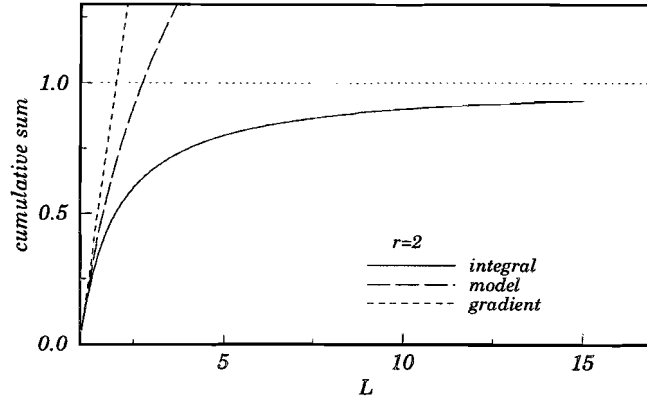


Figure 2.14 (continued).

scenario IV, again in comparison with the peak-indices for the Kamchatka event. For the lower orbits ( $R_1$ ,  $R_2$  and  $R_3$ ) the synthetic curves follow the observed curve well. Only at the longest propagation distances of the  $R_4$  arrivals do the synthetic values start to fall below the observed values.

In our analysis we assumed that a complete wave train can be decomposed into several identical individual wave trains. Each arrival has taken a different path to the receiver. In the real earth this leads to waveforms that are not exactly identical, because the structure along each path is not identical. Forward scattering, for example, could cause differences in the waveforms. In addition we assumed that characteristic length scales are similar for all frequencies. Due to these assumptions our analysis of the synthetic surface-wave spectra is correct up to first order. Only qualitative inferences can thus be drawn from the synthetic experiments. The peak-indices for the higher orbits seem to be better explained by models with power spectra like in scenarios I and II than by a model with a power spectrum like in case IV (compare Figures 2.14a and 2.14c). However, as our analysis is relatively crude, it is not justified to draw from this observation the conclusion that the heterogeneity power spectrum is flat up to at least  $l = 36$ . From the experiments discussed here it follows that the observed peak-indices, which depend on the gradients present in the true earth structure, cannot be explained by the global seismological models. If models are considered with more power at intermediate-scale structure and consequently stronger gradients, the observed complexity of the surface-wave amplitude spectra can be better explained. In addition to the power spectra in Figure 2.3a and the one-dimensional numerical examples of section 2.2.2, this is an additional



**Figure 2.15** Cumulative sums of the amplitude spectra of the model (long-dashed line), of the long-path integral of the model (solid line) and of the gradient of the model (short-dashed line) for the case that the model is described by a power spectrum of the shape  $l^{-2}$ . The convergence level is scaled to unity.

indication that at intermediate wavenumbers the current global seismological earth models underestimate the power present in the real earth.

## 2.5 Convergence of models

Although current global earth models are not able to account for the observed amount of multipathing, which depends on the gradient of the earth's structure, they are able to explain travel-times or surface-wave dispersion measurements. To explain this, consider the following example. Suppose the power spectrum of the earth decays as  $l^{-r}$ . The amplitude spectrum then decays as  $l^{-r/2}$ . The amplitude spectrum of the integral of the structure along a long path will then decay as  $l^{-r/2-1}$  [Mochizuki, 1993]. The amplitude spectrum of the gradient of the model will contain an extra factor  $l$  with respect to the amplitude spectrum of the model itself and will therefore be of the form  $l^{-r/2+1}$ . Figure 2.15 shows the cumulative sums of the amplitude spectra of the model ( $\sum_{l=1}^L l^{-r/2}$ ), of the long-path integral of the model ( $\sum_{l=1}^L l^{-r/2-1}$ ) and of the gradient of the model ( $\sum_{l=1}^L l^{-r/2+1}$ ) as a function of  $L$ . The parameter  $r$  was taken equal to 2, because that is the most common value for global models (Figure 2.3a). From Figure 2.15 it is clear that the cumulative sum of the integral converges rapidly (for  $L = 15$  the cumulative sum is more than

90% of the asymptotic value), but that the cumulative sum of the model itself and also the cumulative sum of the gradient of the model diverge. This implies that an expansion up to  $l = 16$  or  $l = 36$  (Table 2.1) of the global models is a sufficient and adequate description of the model in order to fit parameters that are integrals of the model. However, in order to fit parameters that depend on the gradients of the model, such as the peak-index of surface-wave amplitudes or polarizations, a description of the earth's structure up to these harmonic degrees will be insufficient. This explains why current earth models, although they do not contain sufficient power at intermediate scales, can account for the observed travel-time and surface-wave dispersion data, but need not necessarily account for the short-wavelength components of earth structure.

Of course the analysis of this section is crude. It ignores the extra oscillating terms in the spherical-harmonic expansion (2.1). For this reason the convergence will in practice be faster than in the simple model shown in Figure 2.15. However, this example explains qualitatively why gradient-dependent quantities are not accounted for by current earth models, while the observed travel times and dispersion measurements of surface-waves are.

## 2.6 Conclusions and discussion

The comparison of spectra of global and regional tomographic models shows a clear discrepancy at intermediate-scale structure between global and regional tomographic models. Two explanations are given for this discrepancy. One is that the earth is locally more complex than the global average. This reduces the discrepancy in the power spectra by a factor 10. On the other hand, a lack of resolution due to a limited path coverage explains the qualitative features of the observed spectra as well. The effect of limited path coverage is aggravated by the fact that the data are integrals of the model. The low-pass character of inversion for earth structure has previously been pointed out by *Kawakatsu* [1983], who addressed this topic by showing that the averaging property of great-circle data reduces the resolution of the heterogeneity in the result. *Mochizuki* [1993] quantified the low-pass effect present in the data by computing the sensitivity of lateral heterogeneity for the ray-theoretical line integral. Suppose by analogy that the data were gradients of the medium instead of integrals, a lack of resolution would manifest itself in poorly resolved large-scale structures. This is a well-known problem in exploration seismics; reflected waves only constrain the short-wavelength component of the impedance, but the trend in the impedance model is not constrained by the reflected waves

[*Jannane et al.*, 1989].

To investigate the shape of the power spectrum of the earth around the intermediate wavenumbers in another way, data were considered that depend on the velocity gradient of earth structure. The complexity of amplitude spectra of surface-waves is a result of interference due to multipathing. As multipathing is caused by gradients in earth structure, the complexity of the amplitude spectra is a measure of the gradients (and therefore also the length scales, because strong gradients are associated with small-scale structures and weak gradients are associated with large-scale structures). We demonstrated that existing global models do not explain the observed complexity of amplitude spectra of long-period surface-waves. We pointed out with a simple example why current models, although too smooth and unable to explain gradient-dependent multipathing data, are able to fit data that are integrals of the model. We showed that random models with more power at intermediate scales than the existing global models lead to multipathing that approaches observed effects. Extension of the spectra to  $l = 100$  was not of major importance as ray theory breaks down and rays are no longer sensitive to such small-scale structures. The main conclusion to be drawn from this study is that the earth probably contains more power at intermediate wavelengths (around  $l = 30$ ) than is currently imaged by the global seismological models.

Correct mapping of structure with intermediate wavelengths, which implies correct mapping of the gradients, is important, because horizontal density gradients are a driving force for convective currents. More detailed analyses of the intermediate-scale structure can be performed by using denser path coverages and shorter paths than are currently used. A second option is to construct earth models based on data sensitive to the gradients of the earth structure, such as amplitudes [*Woodhouse and Wong*, 1986; *Neele et al.*, 1993a,b] or polarizations [*Hu and Menke*, 1992; *Levshin et al.*, 1994]. A major problem with this is that such data are less robust than travel-time or surface-wave dispersion data. Such a different approach would, however, significantly change the type of information to be gained from seismological inversions.

## Chapter 3

# Using differential waveform data to retrieve local shear velocity structure or path-averaged shear velocity gradients

**Abstract** An algorithm is presented which uses the surface waveforms originating from one event recorded in two stations which are located close to each other. The waveforms are inverted for local laterally homogeneous  $S$  velocity structure or for path-averaged horizontal  $S$  velocity gradients. In the first case, the stations are situated on the same great circle to the source. In the second case, the two stations lie at approximately the same epicentral distance, but with a slightly different azimuth. In both cases, the frequency-dependent phase differences between the two recordings are used as data for an inversion for  $S$  velocity values. No a priori knowledge about the source parameters and the medium between the source and the nearest receiver is needed. These factors are estimated in the first step of the inversion (linear). In the second step of the inversion (nonlinear) the  $S$  velocity information is obtained. Synthetic tests show that the algorithm is a powerful tool to image structure with only two fundamental mode surface wave recordings as data. In addition, they show that for the case where a horizontal gradient is determined, higher modes can be included in the analysis to display gradients at larger depths, without the need to identify the individual modes separately. The power of the method is illustrated

---

<sup>1</sup>A shortened version of this chapter has been published as: M.L. Passier and R.K. Snieder, 1995. Using differential waveform data to retrieve local  $S$  velocity structure or path-averaged  $S$  velocity gradients, *J. geophys. Res.*, **100**, 24061–24078. (Geodynamics Research Institute (Utrecht University) publication 95.073).

with some real data examples that are all related to a pronounced tectonic boundary in western Eurasia: the Tornquist-Teisseyre zone. The results of the experiments with real data coincide well with previously obtained models for this area.

### 3.1 Introduction

The use of surface waves to determine the seismic velocities in the earth is widespread in present-day geophysics. This is done on a global scale [e.g., *Zhang and Tanimoto, 1993; Montagner and Tanimoto, 1991*] or on a regional scale [e.g., *Snieder, 1988; Roult et al., 1994; Zielhuis and Nolet, 1994*]. The attention in this paper will be focussed on inversion of surface wave data to model regional scale features. Already in the 1960s two- or multiple-station methods were applied to measure surface wave phase velocities [e.g., *Brune and Dorman, 1963; Knopoff et al., 1966, 1967*]. A classical approach is to use two stations that lie on approximately the same great circle with the source. In a first step, group and phase velocity dispersion curves are determined from the surface wave recordings. In a second step, these curves are used as data for an inversion to find the medium parameters. A more recent approach is to invert the recorded waveforms directly for path-averaged earth structure [e.g., *Lerner-Lam and Jordan, 1983; Nolet et al., 1986c*]. The procedure followed in this paper also uses the waveforms rather than the dispersion characteristics as data for the inversion. The presented algorithm is based on the method described by *Kushnir et al. [1988, 1989]*. Their method is an elegant version of the classical two-station method. The essential difference of their strategy compared to previous inversion strategies is that the medium between the two stations on the same great circle with the source is obtained by minimizing a functional which is independent of (1) the source parameters and (2) the medium between the source and the nearest receiver. In this paper their method is extended to another application in which two nearby stations with the same distance to the source are used to estimate the horizontal gradient in the earth. Also, in this extension higher modes can be incorporated in the inversion, which significantly enlarges the depth penetration and increases the resolution. In addition a tool is introduced to stabilize the inversion when using data with considerable noise. The power of the algorithm is illustrated with synthetic tests and examples of inversion of real data.

## 3.2 Method

The method used in this paper is based on an algorithm originally proposed by *Kushnir et al.* [1988, 1989]. They determine a horizontally stratified medium for the crust and uppermost part of the mantle between two stations lying approximately on the same great circle with the source. Their data are complex spectra of surface wave recordings. In the first step, parameters related to the source and the medium between the source and the nearest receiver are estimated. This constitutes a linear inverse problem. In the second inversion step, the model between the stations is determined using a method of nonlinear optimization. Their algorithm will be discussed and used as a basis for an extension to more general applications.

### 3.2.1 Fundamental mode data

The theory presented in this section is for multi-component Rayleigh waves in a Cartesian geometry. The extension to Love waves, spherical geometry [*Snieder and Nolet, 1987*], or single-component data is straightforward. Suppose the main portion of surface wave energy is carried by the fundamental mode and the energy content of higher modes can be neglected (this can often be achieved by time-variant filtering of the seismograms [*Landisman et al., 1969*]). For a station  $A$  the displacement can then be written in the frequency domain as

$$\mathbf{u}_A(\omega) = \frac{d_A}{g_A} \mathbf{p}(\omega) E(\omega) e^{i\phi_A} . \quad (3.1)$$

The vector  $\mathbf{u}_A(\omega)$  contains the data which are the complex amplitude spectra of the radial and the vertical component:  $\mathbf{u}_A(\omega) = (u_{Ar}(\omega), u_{Az}(\omega))^T$ . The superscript  $T$  denotes the transpose. In equation (3.1)  $d_A$  represents the anelastic damping, which depends on the wavenumber  $k$ , the epicentral distance  $\Delta_A$  and the quality factor  $Q$  as  $d_A = \exp(-k\Delta_A/2Q)$ .  $g_A$  denotes the geometrical spreading, which is proportional to the square root of the epicentral distance. The polarization vector  $\mathbf{p}(\omega)$  is the vector containing the Rayleigh wave eigenfunctions at the free surface for radial and vertical displacement under the stations [*Snieder, 1986*]:  $\mathbf{p}(\omega) = (r_r(\omega), i r_z(\omega))^T$ .  $E(\omega)$  contains the complex excitation terms of the source and  $\phi_A$  denotes the phase in station  $A$ . Assuming that an observation of the same event in a nearby station  $B$  can be considered as the observation in station  $A$ , but with a different phase and a slightly different amplitude due to small changes in geometrical spreading and damping, the recording in station  $B$  can be written as

$$\mathbf{u}_B(\omega) = \frac{d_B}{g_B} \mathbf{p}(\omega) E(\omega) e^{i\phi_B} .$$

If the phase  $\phi_B$  is decomposed as  $\phi_B = \phi_A + \delta\phi_{AB}$ , this can be written as

$$\mathbf{u}_B(\omega) = \mathbf{u}_A(\omega) \frac{g_A d_B}{g_B d_A} e^{i\delta\phi_{AB}} . \quad (3.2)$$

Combining equations (3.1) and (3.2) yields

$$\begin{pmatrix} \mathbf{u}_A(\omega) \\ \mathbf{u}_B(\omega) \end{pmatrix} = \begin{pmatrix} \mathbf{p}(\omega) e^{i\phi_0} \\ g d \psi_0 \mathbf{p}(\omega) e^{i\phi_0} \end{pmatrix} c(\omega) , \quad (3.3)$$

where

$$\begin{aligned} g &= \frac{g_A}{g_B} \\ d &= \frac{d_B}{d_A} \\ \psi_0 &= e^{i\delta\phi_{AB}} \\ c(\omega) &= \frac{d_A}{g_A} e^{i(\phi_A - \phi_0)} E(\omega) . \end{aligned}$$

The phase  $\phi_A$  (in  $c(\omega)$ ) has been split into a phase  $\phi_0$  according to a certain reference structure between the source and station  $A$  and a residual phase  $\delta\phi_A = \phi_A - \phi_0$ . The quantity  $\phi_0$  can easily be computed for a given reference model. It serves to remove contributions to  $c(\omega)$  that fluctuate strongly with frequency. Given the data  $\mathbf{u}_A(\omega)$  and  $\mathbf{u}_B(\omega)$ , equation (3.3) constitutes a set of linear equations in the complex scalar  $c(\omega)$ . The  $4 \times 1$  right-hand side vector, which will be called  $\mathbf{t}$ , does not only depend on  $\omega$  but also on the  $S$  velocity model  $\mathbf{m}$  that explains the phase difference of the spectra recorded at the two stations. This model is needed to compute the phase difference  $\delta\phi_{AB}$ , which is crucial in equation (3.3). Equation (3.3) can thus be written as

$$\begin{pmatrix} \mathbf{u}_A(\omega) \\ \mathbf{u}_B(\omega) \end{pmatrix} = \mathbf{u}(\omega) = \mathbf{t}(\mathbf{m}, \omega) c(\omega) .$$

Note that the scalar  $c(\omega)$ , hereafter referred to as the source term, depends only on the source and on the structure between the source and station  $A$ . An optimal estimate for the model  $\mathbf{m}$  can be obtained by minimizing the functional

$$\mathcal{F}_0(\mathbf{m}) = \sum_{\omega_k} \|\mathbf{u}(\omega_k) - \mathbf{t}(\omega_k, \mathbf{m}) c(\omega_k)\|^2 . \quad (3.4)$$

Note that this functional depends both on the model  $\mathbf{m}$  and the unknown source term  $c(\omega)$ . When  $\mathbf{m}$  is fixed,  $\mathcal{F}_0$  reaches a minimum for

$$\hat{c}(\omega_k) = \frac{\mathbf{t}^\dagger(\omega_k) \mathbf{u}(\omega_k)}{\mathbf{t}^\dagger(\omega_k) \mathbf{t}(\omega_k)} , \quad (3.5)$$



where  $\mathbf{t}^\dagger \mathbf{u}$  is defined as  $\sum_i t_i^* u_i$ . The asterisk denotes the complex conjugate. Variable  $\hat{c}(\omega)$  represents the least squares estimate of the excitation parameters and of the propagation effects through the medium between the source and station  $A$ . The reason for splitting  $\phi_A$  in the definition of  $c(\omega)$  (see above, equation (3.3)) into  $\phi_0$  and  $\delta\phi_A$  is that  $c(\omega)$  can be a strongly oscillating function of frequency. This may complicate a proper estimation of  $\hat{c}(\omega)$ . By including a factor  $e^{i\phi_0}$  in the vector  $\mathbf{t}$ , this problem is alleviated, as the part that is left in the source term is a smoother function of frequency than  $e^{i\phi_A}$ . Substitution of equation (3.5) into equation (3.4) and introducing a short-hand notation for the  $\omega_k$  dependence ( $\mathbf{t}_k \equiv \mathbf{t}(\omega_k)$ ) leaves the following functional to be minimized with respect to the model  $\mathbf{m}$ :

$$F_0(\mathbf{m}) = \sum_k \left\| \mathbf{u}_k - \mathbf{t}_k \frac{\mathbf{t}_k^\dagger \mathbf{u}_k}{\mathbf{t}_k^\dagger \mathbf{t}_k} \right\|^2 . \quad (3.6)$$

Given a reference model and a certain model  $\mathbf{m}$ , the phase difference  $\delta\phi_{AB}$  (and hence  $\psi_0$ ), and  $\mathbf{t}$  can be computed. The polarization vector  $\mathbf{p}$  and the damping  $d$  are computed for the reference model, which is correct up to first order. This makes it possible to minimize  $F_0(\mathbf{m})$  iteratively using a conjugate gradient algorithm. The vector  $\mathbf{t}(\mathbf{t}^\dagger \mathbf{u} / \mathbf{t}^\dagger \mathbf{t})$  in equation (3.6) consists of the synthetic complex amplitude spectra for the different components recorded by the two stations for the current model  $\mathbf{m}$  and for the frequency  $\omega_k$ . Therefore, synthetic seismograms can be generated for each component and each station using the model that minimizes  $F_0$ . Note that in this process the excitation terms are estimated from the data rather than computed from *a priori* knowledge of the source.

In practice, the minimization of  $F_0$  can be applied in two cases, which are shown in Figure 3.1. The first case, hereafter called case I, consists of two stations lying almost on the same great circle that connects them with the source. This configuration was also treated by *Kushnir et al.* [1988, 1989]. The second case, not treated by them and hereafter called case II, consists of two stations located at approximately the same distance from the source, but with a different back azimuth. Depending on which case is studied, the retrieved model  $\mathbf{m}$  which minimizes  $F_0$  has to be interpreted in different ways.

Suppose that case I is considered. The phase difference  $\delta\phi_{AB}$  for a wavenumber  $k$  between station  $A$  and  $B$  is needed for the computation of  $\mathbf{t}$  (and  $F_0$ ). If the distance between station  $A$  and  $B$  in case I (Figure 3.1) is called  $d\Delta$ , this phase difference is given by

$$\delta\phi_{AB} = k d\Delta = \frac{\omega}{c_0 + \delta c} d\Delta ,$$

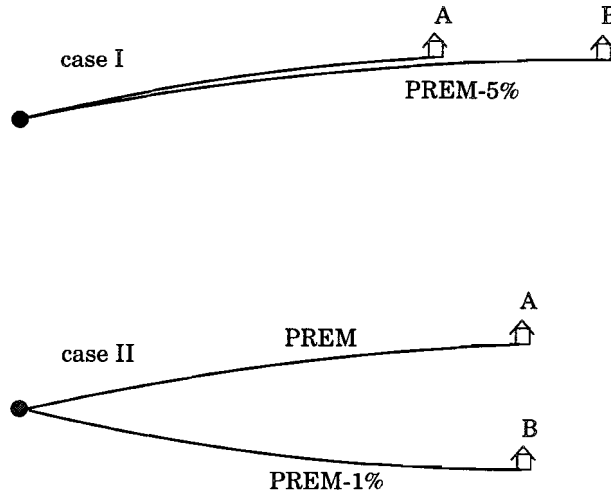


**Figure 3.1** The two source-station configurations to which the algorithm can be applied. The solid circles represent the sources, the houses represent the stations, and the lines represent the great circles along which the surface waves propagate. Also indicated are the models used for the synthetic inversions.

where  $c_0$  is the phase velocity in a reference model and  $\delta c$  the phase velocity perturbation. This perturbation is linearly related to the model perturbation  $\delta\beta/\beta_0$  ( $S$  velocity perturbation), which is a function of depth, via Rayleigh's principle [Aki and Richards, 1980]:

$$\frac{\delta c}{c_0} = \int \mathcal{K}(z) \frac{\delta\beta(z)}{\beta_0(z)} dz .$$

The values of  $\delta\beta/\beta_0$  are the model parameters for which the data are inverted. Any dependence of the phase velocity perturbation on  $P$  velocity and density perturbations is assumed to be small compared to the dependence on  $S$  velocity. The sensitivity kernel  $\mathcal{K}(z)$  can be found by Aki and Richards [1980], and is computed for a reference model. Rayleigh's principle states that this is correct up to first order. Because  $\delta\beta = \beta - \beta_0$ , the model parameters obtained by minimizing  $F_0$  in equation (3.6) should for case I be interpreted as the relative difference between the true  $S$  velocity structure and the reference  $S$  velocity model between stations  $A$  and  $B$ . This changes when case II is considered (Figure 3.1). If the epicentral distance from the source to  $A$  is the same as the epicentral distance to  $B$ , the phase

difference can be written as

$$\delta\phi_{AB} = \omega \int_0^\Delta D(s) \partial_\perp(1/c) ds , \quad (3.7)$$

where  $s$  is the distance along the ray path,  $D(s)$  the distance between the two paths for a propagation distance  $s$  and  $\partial_\perp(1/c)$  the derivative of the reciprocal phase velocity in the direction perpendicular to the great circle between the two paths. If the average slownesses along the paths to the stations are denoted by  $\langle 1/c_A \rangle$ , respectively  $\langle 1/c_B \rangle$ , the expression for the phase difference becomes

$$\delta\phi_{AB} = \omega \Delta \left( \left\langle \frac{1}{c_B} \right\rangle - \left\langle \frac{1}{c_A} \right\rangle \right) ,$$

with  $\Delta$  the epicentral distance. Expressing both phase velocities in reference velocity and a residual part ( $c_A = c_0 + \delta c_A$ ,  $c_B = c_0 + \delta c_B$ ) gives

$$\delta\phi_{AB} \approx \frac{\omega \Delta}{c_0^2} (\delta c_A - \delta c_B) ,$$

where  $\delta c_A$  and  $\delta c_B$  are the average phase velocity perturbations for the paths to the stations  $A$  and  $B$ . Using Rayleigh's principle again leads to

$$\frac{\delta c_A - \delta c_B}{c_0} = \int \mathcal{K}(z) \left( \frac{\delta\beta_A(z) - \delta\beta_B(z)}{\beta_0(z)} \right) dz ,$$

where  $\delta\beta_{A \text{ or } B}(z) = \beta_{A \text{ or } B}(z) - \beta_0(z)$ . Because  $(\delta\beta_A - \delta\beta_B)/\beta_0 = (\beta_A - \beta_B)/\beta_0$ , the parameters determined by an inversion of data for case II should be interpreted as the relative difference between the two average  $S$  velocity structures under paths  $A$  and  $B$ . Since this difference is a path-averaged quantity, the effect of local anomalies is smeared out over the entire path. This makes case II more suited for studying situations where a clear distinction between the structure under path  $A$  and the structure under path  $B$  can be expected.

### 3.2.2 Including higher modes

In the previous section it was assumed that the main part of the recorded energy was present in the fundamental mode Rayleigh wave only. Now suppose that also higher modes are present. In the following it is assumed for simplicity that the fundamental and the first higher mode carry the majority of the energy, but an extension to more higher modes is straightforward. The presence of a strong first higher mode causes the right-hand side of equation (3.3) to change. For every separate mode

the principle of the recording at one station being just the other recording with an additional, frequency dependent, phase shift remains valid. The theory of the previous section holds for each individual mode (each with its own polarization vector  $\mathbf{p}$  and scalar source term  $c$ ). Because the modes have to be summed, the scalars and vectors of the previous section now become vectors and matrices. The polarization vector  $\mathbf{p}$  transforms into a matrix  $P$ , each column representing the eigenfunctions for one mode:

$$P = \begin{pmatrix} r_{0r} & r_{1r} \\ ir_{0z} & ir_{1z} \end{pmatrix} .$$

The scalar  $d$  in equation (3.3) changes into a diagonal matrix  $D$  with the ratios  $d_B/d_A$  for the different modes on the different diagonal positions. The scalar  $\psi_0$  indicating the phase shift between the two stations also becomes a diagonal matrix  $\Psi$  with the phase shifts for the individual modes on the diagonal:

$$\Psi = \begin{pmatrix} e^{i\delta\phi_{AB,0}} & 0 \\ 0 & e^{i\delta\phi_{AB,1}} \end{pmatrix} .$$

The scalar source term  $c$ , which contains information on the excitation and the medium between the source and station  $A$ , changes into a vector  $\mathbf{c}$  of which each element represents one mode:

$$\mathbf{c} = \begin{pmatrix} \frac{d_{A,0}}{g_A} e^{i\delta\phi_{A,0}} E_0(\omega) \\ \frac{d_{A,1}}{g_A} e^{i\delta\phi_{A,1}} E_1(\omega) \end{pmatrix} .$$

Just as in the previous section, for each mode the phase in  $A$  is split into a reference phase, which is taken out of  $\mathbf{c}$  and a residual part in order to make  $\mathbf{c}$  more slowly oscillating. The set of linear equations now obtained can be written as (compare with previous section)

$$\mathbf{u}(\omega) = T(\mathbf{m}, \omega) \mathbf{c}(\omega) ,$$

where  $T$  is a matrix composed of the matrices discussed above.  $T$  has four rows (one for each recorded component) and two columns (or as many as there are modes in the signal). The functional to be minimized now becomes

$$\mathcal{F}_1(\mathbf{m}) = \sum_k \|\mathbf{u}_k - T_k(\mathbf{m}) \mathbf{c}_k\|^2 . \quad (3.8)$$

Estimating the source term  $\mathbf{c}_k$  in a least squares sense, *i.e.* estimating the source parameters and propagation effects between the source and  $A$  for the different modes, leads to

$$\hat{\mathbf{c}}_k = (T_k^\dagger T_k)^{-1} T_k^\dagger \mathbf{u}_k , \quad (3.9)$$

where the dagger denotes the Hermitian conjugate. Note the analogy between equations (3.9) and (3.5). Substitution of equation (3.9) in equation (3.8) gives the functional to be minimized:

$$F_1(\mathbf{m}) = \sum_k \left\| \mathbf{u}_k - T_k (T_k^\dagger T_k)^{-1} T_k^\dagger \mathbf{u}_k \right\|^2 . \quad (3.10)$$

From this point on the procedure is similar to the case with only the fundamental mode in the signal. Given a model  $\mathbf{m}$ ,  $\Psi$  and  $T$  can be computed and with the use of a conjugate gradient method  $F_1$  is minimized. Synthetic seismograms for the different components at the different stations can then be generated by computing  $T\hat{\mathbf{c}}$ .

The method derived for the fundamental mode only, as well as for the higher modes assumes that the values of the source terms ( $c(\omega)$  and  $\mathbf{c}(\omega)$ ) are identical for the stations  $A$  and  $B$ . This implies that large errors will be introduced if the radiation pattern  $E(\omega)$  of the source varies too much over the range between the takeoff azimuth to station  $A$  and the takeoff azimuth to station  $B$ . The radiation pattern of the source, and in particular the phase radiation pattern, should therefore be considered carefully prior to any inversion.

Summarizing, the method outlined by *Kushnir et al.* [1988, 1989] is an extension of previously used waveform inversion methods in the sense that detailed *a priori* knowledge about the source mechanism and the medium between the source and the nearest receiver is not necessary. These parameters are accounted for by the least squares determination of the source terms. It differs from the two-station method in the sense that a construction of a dispersion curve is not necessary to obtain  $S$  velocity information. In this way error propagation via the mapping from the the dispersion curve to  $S$  velocity is avoided. The method presented in this paper differs from their method in the sense that it is extended to the case of two stations at different azimuths and the same epicentral distance. Furthermore, the incorporation of higher modes is possible without the actual need to identify the individual modes in the signal.

### 3.2.3 Reparameterization

The scenario outlined in the previous sections performs a waveform fit in the frequency domain. The source term coefficients  $\hat{c}$  and  $\hat{\mathbf{c}}$  are estimated independently for each frequency, which leads to a large number of degrees of freedom. This number becomes even higher if data containing higher modes are used. A usual approach to include higher mode data in an analysis is using recordings of these higher modes

over an array of stations [e.g., *Nolet, 1975; Nolet and Panza, 1976; Cara, 1978; Dost, 1990*]. This approach is not followed here, which has the unwanted effect that a large number of degrees of freedom may cause an incorrect determination of the source terms for the individual modes. The source term determination will deteriorate further if considerable noise contaminates the data. Therefore, it might be convenient to reduce the number of degrees of freedom for the source terms in order to make the inversion more robust. This can be achieved by using a reparameterization of the source term. Reparameterization of the source term, which was not considered by *Kushnir et al. [1988,1989]*, will now be discussed for the case that the signal contains a fundamental mode and higher modes. The result simplifies in a trivial way if only the fundamental mode is present in the data.

In the previous section it was derived that the minimum of a functional (now generalized by replacing the summation by an integration) has to be determined:

$$\min \int \|T \mathbf{c} - \mathbf{u}\|^2 d\omega .$$

The function  $\mathbf{c}(\omega)$  can now be parameterized by a limited set of basis functions  $f_j(\omega)$  with complex coefficients  $\gamma_{ij}$ :

$$\mathbf{c}_i(\omega) = \sum_{j=1}^J \gamma_{ij} f_j(\omega) .$$

Inserting this expansion into the functional to be minimized and setting the derivative with respect to  $\gamma_{pq}$  equal to zero yields

$$\sum_{i=1}^N \sum_{j=1}^J \gamma_{ij} T_{ijpq} = M_{pq} , \quad (3.11)$$

where  $i$  and  $p$  range from 1 to the number of modes ( $N$ ) in the signal and  $j$  and  $q$  range from 1 to the number of basis functions used ( $J$ ). The elements of the tensor  $T$  and the matrix  $M$  are given by

$$T_{ijpq} = \sum_{k=1}^4 \int T_{ki} f_j T_{kp}^* f_q^* d\omega$$

$$M_{pq} = \sum_{k=1}^4 \int u_k T_{kp}^* f_q^* d\omega .$$

The index  $k$  ranges from 1 to 4, *i.e.* the number of recorded components. From equation (3.11) the coefficients  $\gamma_{ij}$  can be determined. When the main portion of

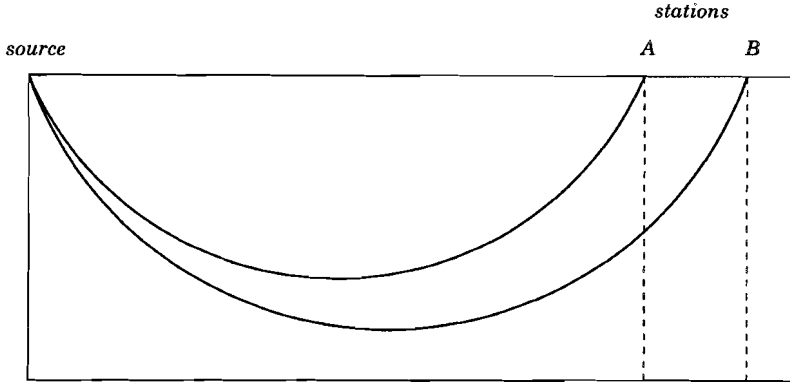


**Figure 3.2** Two body wave rays from a source at the surface to stations on the same great circle. The difference in the area sampled by the two rays is not restricted to the area between the stations *A* and *B* (bounded by the dashed lines).

energy is carried by the fundamental mode only, the tensor reduces to a matrix and the matrices of equation (3.11) reduce to vectors. In the examples shown in this paper Chebyshev polynomials have been chosen to parameterize the source term:  $f_n(\omega) = \cos(n \arccos x(\omega))$ , where the linear transformation

$$x(\omega) = \frac{2\omega - (\omega_{max} + \omega_{min})}{\omega_{max} - \omega_{min}}$$

is used to scale the argument of the Chebyshev polynomials between  $-1$  and  $+1$ .

### 3.3 Practical limitations

Several synthetic tests were performed in order to study the behavior of the inversion algorithm. These examples will be treated in the next section, but first an explanation is given why the algorithm can not be used for inversions of data from two nearby stations on the same great circle as the source which contain higher modes. Figure 3.2 illustrates in an extreme way the problem which is discussed here. Two geometrical body wave rays are drawn from the source to the stations *A* and *B*. Although the two stations lie on the same great circle as the source, the ray paths sample different areas. This implies that observable quantities at the stations are determined by structure along the entire ray path. Differences in observations between *A* and *B* can therefore not be purely projected on structure in the area

between  $A$  and  $B$  (area between the dashed lines). The situation is sketched here for body waves, but a similar principle holds for higher-mode surface waves, since after mode summation they also account for body wave arrivals [Harvey, 1981; Nolet et al., 1989; Marquering and Snieder, 1995].

The algorithm for case I (two stations on one great circle) has been designed with the idea that phase differences between the recordings in  $A$  and  $B$  are entirely caused by structure between  $A$  and  $B$  and that structure under the path from the source to  $A$  does not contribute to the observed phase differences between  $A$  and  $B$ . The question is whether in practice the structure between the source and  $A$  indeed has no effect on the recorded phase differences. To investigate this, the following experiment was carried out. In the Born approximation, the total displacement  $\mathbf{u}$  of a wave field is given in terms of a reference wave field  $\mathbf{u}^0$  and a perturbation  $\delta\mathbf{u}$  of that wave field:

$$\mathbf{u} = \mathbf{u}^0 + \delta\mathbf{u} .$$

For laterally homogeneous media with only a depth dependence of the structure, the reference wave field  $\mathbf{u}^0$  can be written for a given frequency as a sum of surface wave modes Snieder, [1986]. The perturbation  $\delta\mathbf{u}$  is linearly related to the model perturbations  $\delta\beta$  by

$$\delta\mathbf{u} = \iint K(x, z) \delta\beta dz dx ,$$

where for two dimensions  $K(x, z)$  is the sensitivity kernel for perturbations in the model parameters. This kernel contains a summation over all modes [Marquering and Snieder, 1995]. Consequently, for the difference between a wave field recorded in  $B$  and a wave field in  $A$ :

$$\delta\mathbf{u}^B - \delta\mathbf{u}^A = \iint [K^B(x, z) - K^A(x, z)] \delta\beta dx dz .$$

If a single mode is considered or when mode coupling is neglected, the kernels  $K^A$  and  $K^B$  vary in a similar way with depth ( $z$ ) and are constant in the horizontal  $x$  direction [Marquering and Snieder, 1995]. Therefore,  $K^B(x, z) - K^A(x, z)$  is only non-zero between  $A$  and  $B$ , implying that the differences in the recordings between  $A$  and  $B$  are only due to structure between  $A$  and  $B$ . This reflects the fact that when surface wave mode coupling is neglected, only the average structure between the source and the receiver affects the seismogram [e.g., Woodhouse, 1974]. This is exactly what happens in a case I inversion of the fundamental mode. However, if more modes are present in the signal, coupling between the individual modes will occur and  $K^A$  and  $K^B$  will both be varying in the  $x$  and  $z$  direction. Exact expressions for the kernels can be found by Marquering and Snieder [1995]. Figure



3.3b shows the spatial distribution of the sensitivity kernel  $K^B(x, z)$  for a period of 40 s in which only mode coupling between the first and the second higher mode is taken into account for an epicentral distance of 2060 km. Figure 3.3a shows the kernel  $K^A(x, z)$  for an epicentral distance of 2000 km. The fundamental mode is left out, because it dominates the other modes, and hence obscures the effect to be emphasized. Note that in Figures 3.3a and 3.3b the rudimentary shape of a geometrical ray is visible, despite the fact that only two modes have been used. (By coupling a high number of modes the transition can be made from surface waves to body waves.) Figure 3.3c shows the differential kernel  $K^B - K^A$ . Note the different contour levels in Figures 3.3a, 3.3b and 3.3c. The difference is only contoured between the source and 2000 km (station *A*). Between 2000 km and 2060 km the difference is just the value of the kernel in Figure 3.3b. In contrast to the situation where mode coupling is neglected (e.g., fundamental mode data only), the sensitivity kernels  $K^A$  and  $K^B$  do not depend only on the average between the source and receiver, but on the horizontal coordinate as well. For this reason the differential kernel in Figure 3.3c is not zero between the source and the closest station *A*. The value of the differential kernel in Figure 3.3c amounts up to about 10% of the individual kernels in Figures 3.3a and 3.3b. The values of the differential kernel between the source and 2000 km are about 10% of the values of the differential kernel between the stations at 2000 km and 2060 km. At first sight, 10% does not seem to be very much, but because the distance from the source to *A* is commonly more than 30 times larger than the distance between *A* and *B*, this part may contribute significantly to the difference between the recordings in *A* and *B*. This means that projecting differences between the waveforms of *A* and *B* solely on the region between *A* and *B* is therefore not correct when higher modes are taken into account. Hence no synthetic experiments are conducted for case I with seismograms containing higher modes.

### 3.4 Inversions of synthetic data

Case I (Figure 3.1) was tested with the distance between the source and station *A* set to 5000 km. The distance between *A* and *B* was chosen to be 50 km. The model that was used between the source and *A* and between *A* and *B* was a perturbed PREM model. For depths shallower than 1000 km an *S* velocity perturbation of  $-5\%$  was applied. Deeper than 1000 km, the model was just PREM. Case II (Figure 3.1) was tested with an epicentral distance of 5000 km, for *A* as well as *B*. Both stations were separated by 200 km. The synthetic seismograms for station *A* were computed

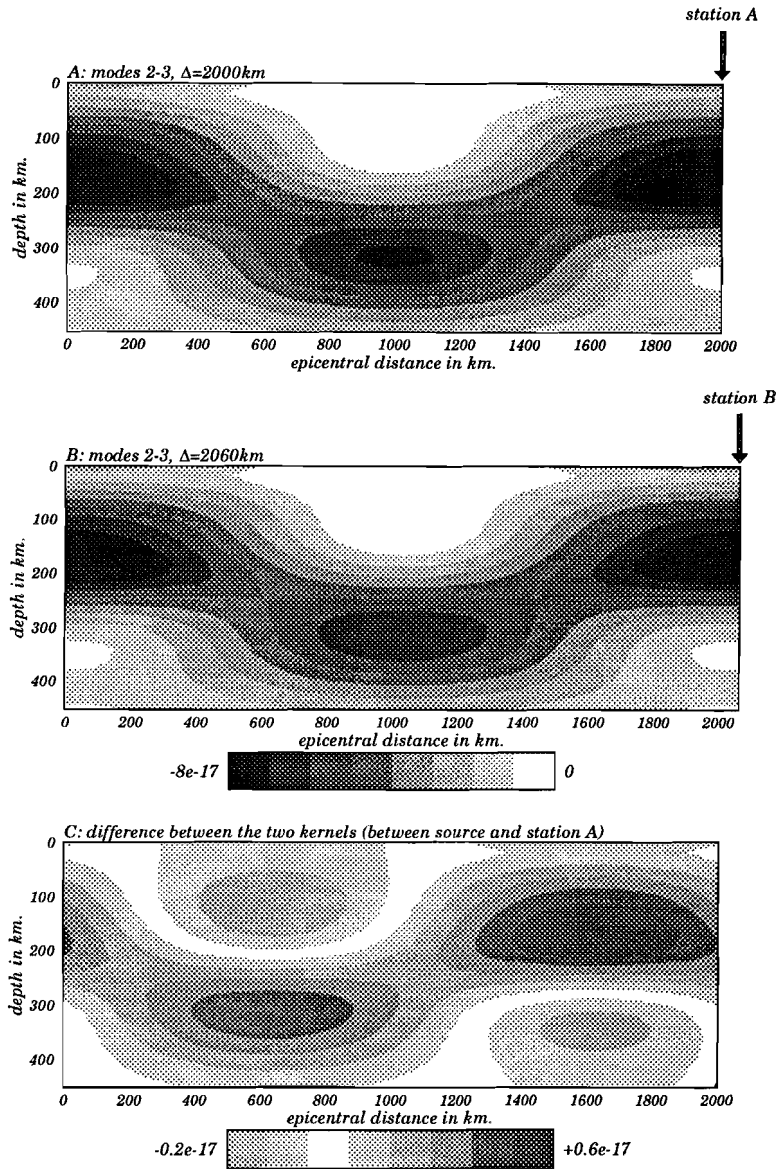


**Figure 3.3** (a) The spatial distribution of the sensitivity kernel for the coupling first and the second higher mode for a period of 40 sec and an epicentral distance of 2000 km. (b) The same kernel, but now for an epicentral distance of 2060 km. (c) The values of the kernel of (b) minus the values of the kernel of (a).

according to the PREM model and for station  $B$  the synthetic data to be inverted were computed according to a model which was 1% slower than PREM for the upper 1000 km. For these configurations synthetic seismograms with periods between 10 and 100 s were constructed and inverted. To generate seismograms with only the fundamental mode the source was placed at a depth of 30 km and to generate also higher modes the source was placed at 100 km depth. The limit of 100 s is in agreement with the frequency range of the real data which will be discussed later. Considering the employed model perturbations, the ideal results of the inversions would be a perturbation of  $-5\%$  for case I and a perturbation of  $+1\%$  for case II (if the PREM model is used as reference model). The models were chosen in such a way that cycle skipping ( $\delta\phi_{AB} \geq 2\pi$ ) would not occur for the frequency band under consideration in the inversions (20–100 s). If in an inversion of real data cycle skipping would be likely to occur, some *a priori* information about the structure has to be added in order to find the correct structure. To help avoiding ending up in a secondary minimum instead of the absolute minimum, the inversions were carried out in two steps. In the first step the lower frequencies were matched and in the second step the higher frequencies were included. If desired, a regularization can be applied to find the smoothest solution for  $\delta\beta/\beta$  that fit the data. Beside the recovered depth profiles, attention will also be paid to the reconstructed source terms  $\hat{c}(\omega)$  and  $\hat{\hat{c}}(\omega)$  of equations (3.5) and (3.9). In a synthetic experiment all source and propagation parameters are known and a comparison can be made between the exact value of the source term and the value as it is estimated by the inversion. In the previous part it was explained that for a particular mode the exact value of the source term is given by

$$c(\omega) = \frac{d_A}{g_A} e^{i\delta\phi_A} E(\omega) ,$$

where  $\delta\phi_A$  is the difference between the recorded phase in  $A$  and the phase in  $A$  according to a reference model. For both case I and case II this is (with the distance between the source and  $A$  called  $\Delta$  and with  $\delta c$  the deviation from the reference phase velocity  $c_0$  between the source and  $A$ )

$$\delta\phi_A = \frac{-\omega \Delta \delta c}{c_0^2} .$$

As  $\delta\phi_A$  and  $E(\omega)$  are unknown (or not exactly known) in an inversion of real data, a comparison between exact and estimated values can only be made under synthetic circumstances. The values of the source term as obtained by the inversion were determined by computing equations (3.5) and (3.9) for the correct model parameters ( $-5\%$  and  $+1\%$ ).

In the following sections several examples will be shown of inversions of synthetic data. The examples concerning case II and the examples where also higher modes are considered are new compared to *Kushnir et al.* [1988, 1989], who only studied the fundamental mode for case I and treated the higher modes only theoretically without analysis of synthetic or real data.

### 3.4.1 Noise-free data

The following inversion results were all obtained using synthetic data without noise. Figures 3.4a and 3.5a show the depth profiles obtained from inversion of seismograms containing only the fundamental mode for case I, respectively case II. Because the data were noise-free and contained only one mode, no reparameterization was used. Figure 3.4a, which is for case I, exhibits a good reconstruction of the  $-5\%$  difference between the actual and the reference model over the depth range where the fundamental mode has resolving power. For larger depths the solution gradually converges to zero because of the finite penetration of the employed fundamental mode Rayleigh waves. The deviations of the solution from  $-5\%$  at depths smaller than approximately 150 km give an indication for the error in the solution. Figure 3.5a shows that also a case II inversion yields good results at the depths where the Rayleigh waves penetrate; the  $1\%$  difference between the model for station *A* and the model for station *B* is well reconstructed. Again, due to limited penetration depth of the fundamental mode, the reconstructed perturbation goes to zero below the penetration depth of the Rayleigh waves. In case I as well case II the function  $c(\omega)$ , which is a combination of source excitation effects and propagation effects, is well determined by the inversion. This can be seen in Figures 3.4b, 3.4c, 3.5b, and 3.5c, which show that the exact values of  $c(\omega)$  and the values as obtained from the inversion do not differ much. As an example of the quality of the data fits, the fits for the vertical component in station *B* are shown in Figures 3.4d and 3.5d. The different waveforms are due to differences in the source mechanism used to generate the data. Except for the highest frequencies ( $T < 20$  s), which are present in the data, but are not taken into account in the inversion, the fits are good. Note also the smooth character of  $\hat{c}(\omega)$ , which makes an inversion without reparameterization possible. The inversions were carried out with PREM as reference model. This is reflected in the phase of  $c(\omega)$  (Figures 3.4b and 3.5b). Taking PREM as the reference model implies that for case II the term  $\delta\phi_A$  in the exact expression for  $c(\omega)$  equals zero (because the model between the source and *A* is PREM and therefore  $\delta c = 0$ ), whereas for case I  $\delta\phi_A \neq 0$ , because the model between the source and *A* is not PREM ( $\delta c \neq 0$ ). The phase of  $c(\omega)$  is therefore more slowly oscillating in case II

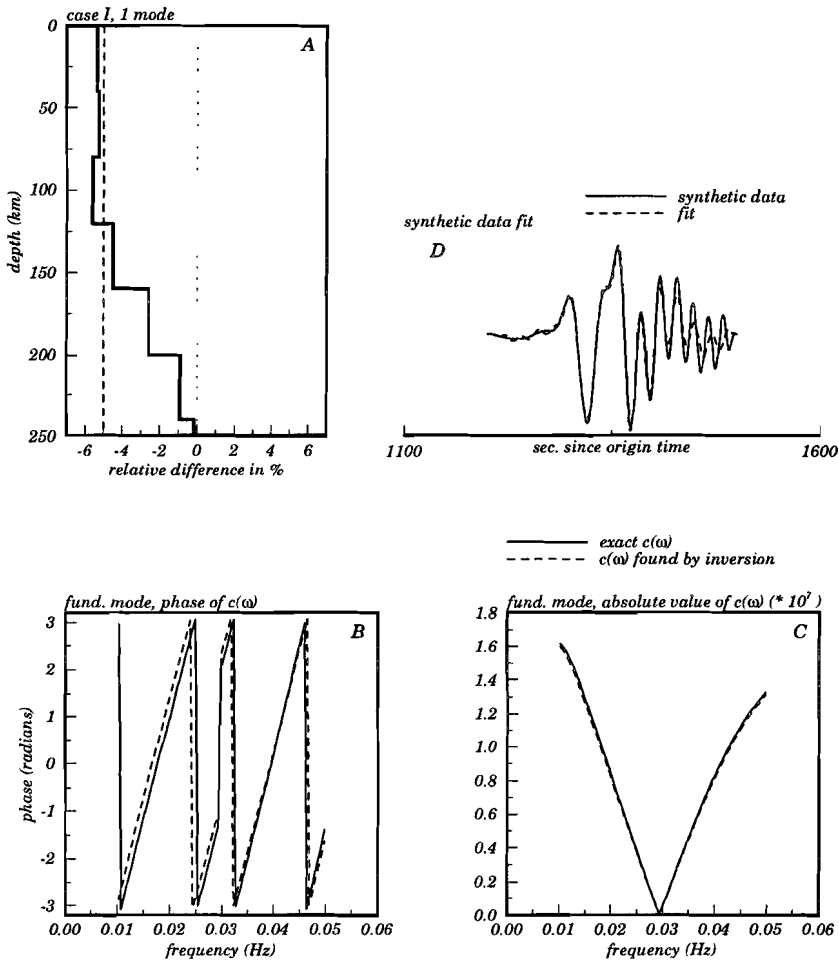


**Figure 3.4** (a) The reconstructed depth profile (solid line) for a case I inversion with only one mode in the seismogram. The thick dashed line indicates the “true” solution of  $-5\%$ , the thin dashed line is  $0\%$ . (b) The phase of the exact function  $c(\omega)$  (solid line) and the estimate of  $c(\omega)$  as obtained by the inversion (dashed line). (c) The same as (b), but now for the absolute value of  $c(\omega)$ . (d) The vertical component in station B (solid line), which was used as data for the inversion, and the fit (dashed line) after inversion.

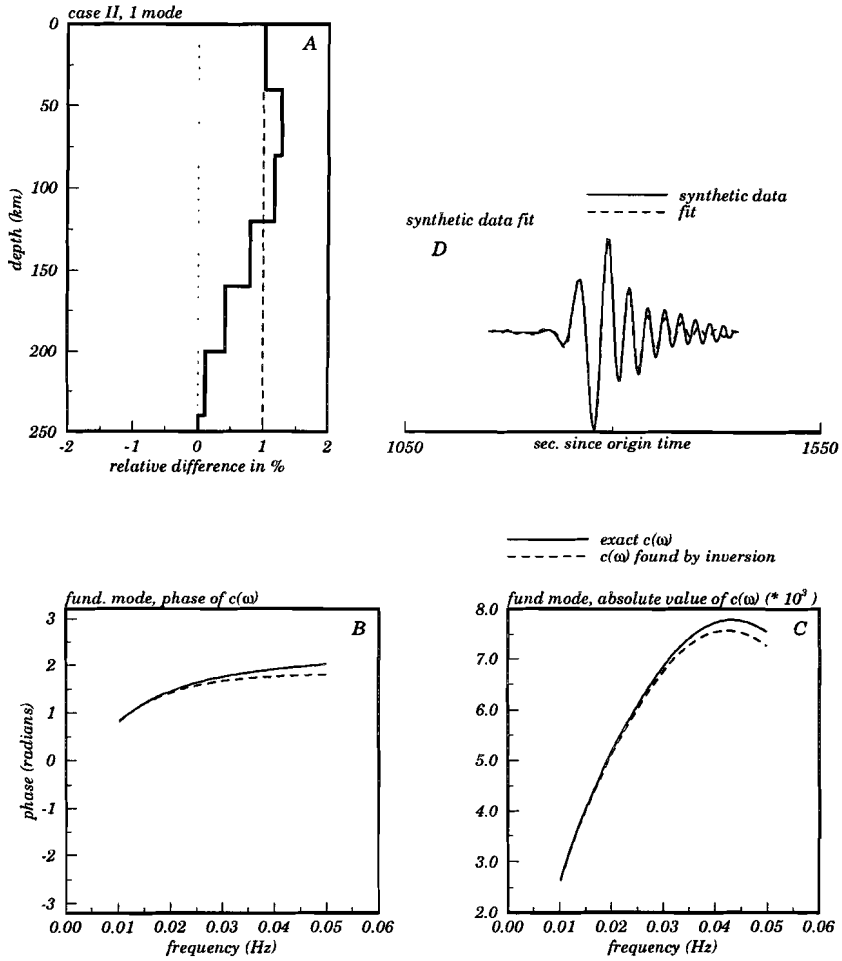


**Figure 3.5** The same as previous figure, but now for case II. The thick dashed line in (a) indicates the "true" solution of 1%.

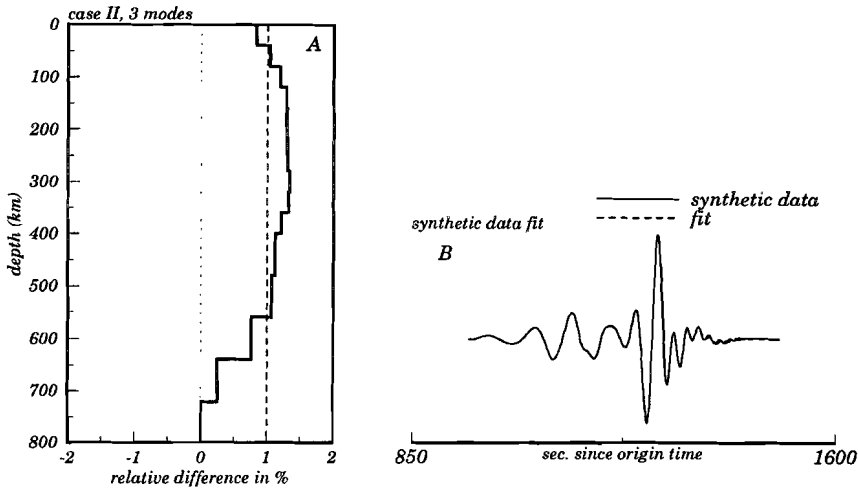


**Figure 3.6** (a) The inversion result (solid line) of a case II inversion without reparameterization of  $c(\omega)$  if the data contain three modes. The dashed lines are the same as in Figure 3.5. (b) The synthetic data and the fit for the vertical component in station B for the inversion result of (a).

(Figure 3.5b) than in case I (Figure 3.4b).

Figure 3.6a shows the result for a case II inversion (without reparameterizing the source term by Chebyshev polynomials) of a noise-free signal containing the fundamental mode and the first two higher modes. Compared to the inversion of one mode (Figure 3.5a) the perturbation of 1% is now reconstructed at larger depths. Again, the obtained fits to the data are good (Figure 3.6b). In Figures 3.7a-f the exact values of the source term (solid lines) are shown together with the values obtained from the inversion (short-dashed lines) for the three individual modes. The obtained absolute values (Figures 3.7a-c) severely oscillate and their amplitudes are not in agreement with the exact values. The obtained phase of the source term for the individual modes (Figures 3.7d-f) is not even close to the exact phase. Nevertheless, these estimations of  $c(\omega)$  lead to the reasonable model reconstruction and good data fits. Apparently, the deviations of the obtained source term from the exact source term do not affect the model reconstruction and the obtained waveform fits. This suggests that the deviations shown in Figures 3.7a-f are a variation in the null-space of the problem. The source terms that are obtained if  $c(\omega)$  is parameterized by four Chebyshev polynomials are shown by the long-dashed

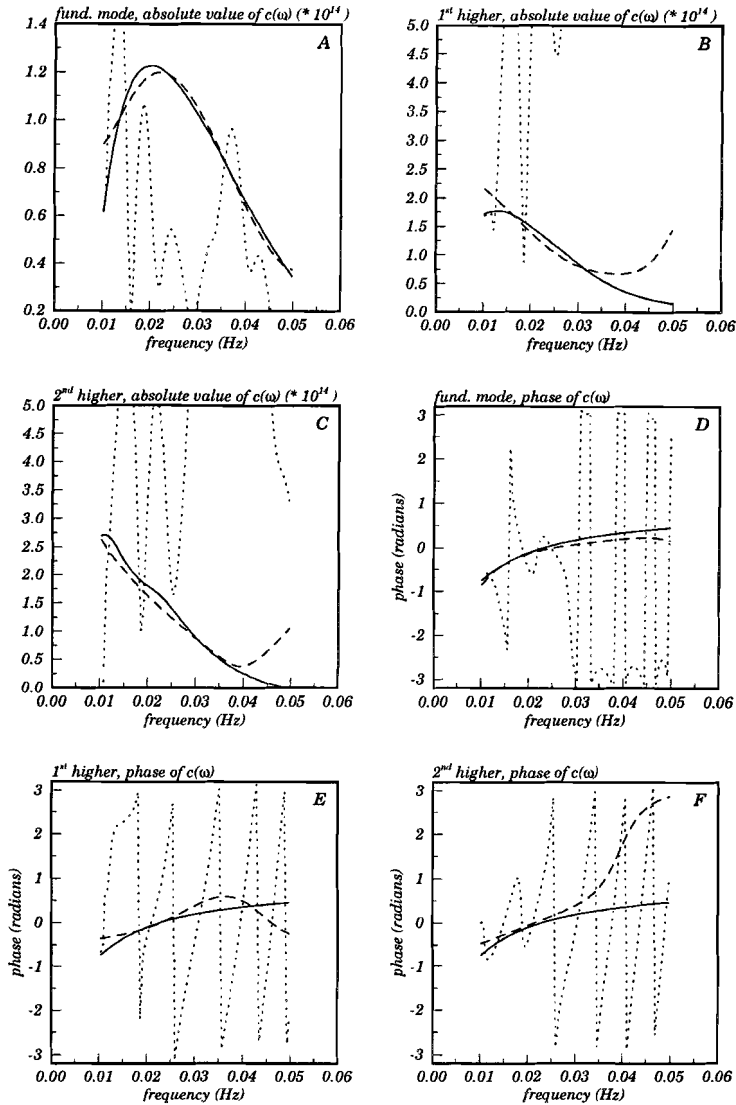


**Figure 3.7** (a)-(c) The absolute values of the exact (solid lines) and estimated (dashed lines) source terms for the three modes of the inversion of Figure 3.6. The short-dashed lines represent an inversion without parameterizing  $c(\omega)$  by Chebyshev polynomials and the long-dashed lines represent an inversion with  $c(\omega)$  parameterized by four Chebyshev polynomials. (d)-(f) The same as (a)-(c), but now for the phases.



lines in Figures 3.7a-f. Using less than four polynomials yielded larger deviations of the reconstructed values from the exact values. Using more than four polynomials increased the computation time, while the source term estimates did not change significantly. Only when more than ten polynomials were taken to parameterize  $c(\omega)$ , the estimates started to exhibit unwanted oscillations. In practice the choice of the number of basis functions one uses depends on how smooth the exact source term is. In contrast with the inversion without a reparameterization, the estimated amplitudes of the source term are now approximately similar to the amplitudes of the exact values and the oscillations have disappeared. The estimated phases also match the exact ones much better if a reparameterization is applied. The model obtained from the reparameterized source term estimates was almost the same as the model in Figure 3.6a and also the fits to the data were as good as in the case without using Chebyshev polynomials.

At this point the conclusion is that a parameterization of the source term by Chebyshev polynomials leads to a better determination of the source term  $c(\omega)$ , but that such a reparameterization is not really necessary for the reconstruction of the model perturbation. Although the inversion without the reparameterization yielded wrong estimates for the source terms when higher modes are included, the model parameters obtained by the inversion are close to their true values, because the deviations of the estimated source terms from the exact source terms lie in the null-space. In order to verify whether the presence of noise in the signal changes this conclusion, synthetic tests with noisy signals were performed.

### 3.4.2 Effects of noise

White noise has been added to the synthetic data used in the previous section. To get an impression of the amount of noise, Figure 3.8 shows an example of a synthetic waveform without noise and the same waveform with noise. The noise shown in Figure 3.8 has the same frequency bandwidth as the waveform. The seismograms contaminated with noise were submitted to the same inversion tests as the noise-free waveforms. Figure 3.9a shows the result for a case I inversion and Figure 3.9b for a case II inversion if the seismograms contain only the fundamental mode. In both cases the structure is well resolved for depths where the penetration depth is sufficient. The obtained data fits (not shown) are good. The inversions were performed without reparameterization, because only one mode was present in the seismograms. The results obtained here are comparable to those obtained for the inversions of the noise-free signals with only one mode (Figures 3.4a and 3.5a). Apparently, the presence of noise is not a limiting factor for inversions of data

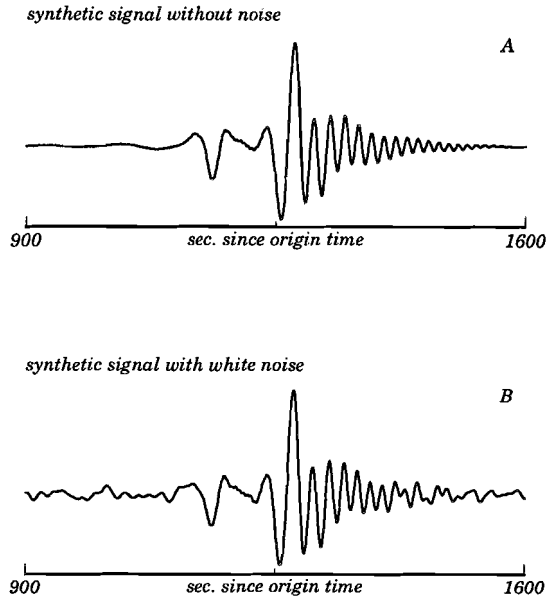


**Figure 3.8** (a) An example of a synthetic seismogram without noise. (b) The same seismogram but with white noise added.

consisting of only one mode. In Figure 3.10 the result is shown of a case II inversion of a signal of three modes contaminated with noise. The inversion was performed with parameterization of the source term by four Chebyshev polynomials. The model is well reconstructed down to a depth of approximately 500 km (Figure 3.10), which is almost as deep as in the noise-free case (compare with Figure 3.6a). The source terms estimated by the inversion (long-dashed lines in Figures 3.11a-f) do not differ much from those in Figures 3.7a-f. It turns out that if the inversion is carried out in the presence of noise without parameterization by Chebyshev polynomials, the retrieved model does not resemble the true perturbation of 1% at all. For this inversion the estimates of the source terms are shown as short-dashed lines in Figures 3.11a-f. The estimates strongly oscillate. Because the model retrieved from this inversion was very different from the true model, it can be concluded that in this case the deviations of the estimates of the source term from the exact values of the source term are not in the null-space of the problem. However, in the noise-free inversion (Figures 3.6 and 3.7), the deviations were in the null-space and

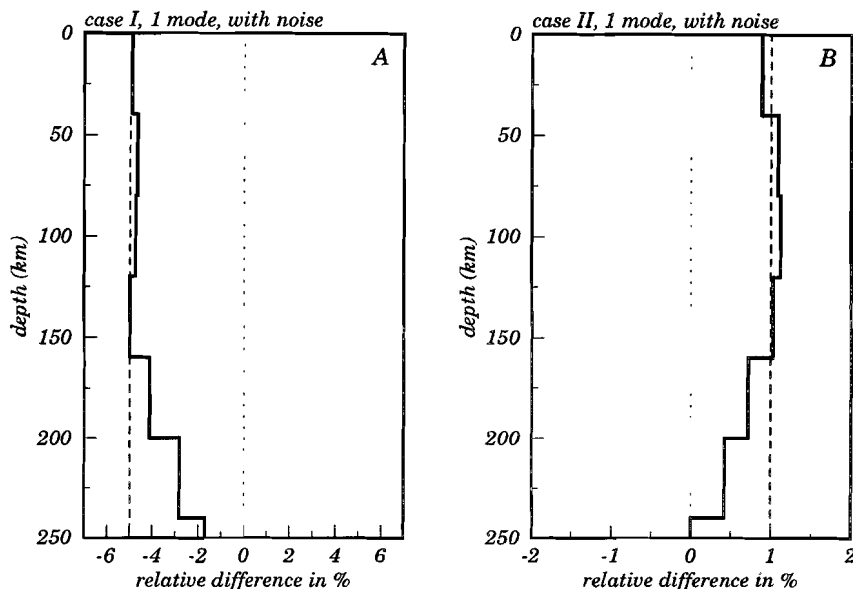


**Figure 3.9** (a) The case I inversion result of data containing only the fundamental mode. Noise was added to the data. (b) The same as (a), but now for case II.

reparameterization was not really necessary. With three modes *and* considerable noise in the signal, it is necessary to apply the reparameterization.

The dependence on whether or not noise is present is somewhat similar to the behavior of a singular value decomposition (SVD) to solve a linear system  $A\mathbf{x} = \mathbf{b}$ . Using SVD, the solution of this problem is given by [e.g., Menke, 1989]  $\mathbf{x} = V\Lambda^{-1}U^T\mathbf{b}$ . Matrix  $U$  contains the eigenvectors  $\mathbf{u}_i$  that span the data space, matrix  $\Lambda$  is diagonal and contains the eigenvalues  $\lambda_i$  of matrix  $A$ , and matrix  $V$  contains the eigenvectors  $\mathbf{v}_i$  that span the model parameter space. Assume for simplicity that the projections of the true model on the eigenvectors  $\mathbf{v}_i$  are of order 1. If  $\mathbf{b}$  is noise-free, and since  $\mathbf{b} = U\Lambda V^T\mathbf{x}$ , the dot product of  $\mathbf{b}$  with eigenvectors in  $U$  will then be of the order of the eigenvalue,  $(\mathbf{b} \cdot \mathbf{u}_i) = O(\lambda_i)$ , and the contribution of this eigenvector to the solution  $\mathbf{x}$  is of the order  $\frac{1}{\lambda_i}(\mathbf{b} \cdot \mathbf{u}_i) = O(1)$ . Small eigenvalues will therefore not dominate the reconstructed solution. However, if  $\mathbf{b}$  is contaminated with noise  $\mathbf{n}$ , the dot product  $(\mathbf{n} \cdot \mathbf{u}_i)$  is not necessarily of the order  $\lambda_i$ , and the corresponding contribution to the solution is of the order  $\frac{1}{\lambda_i}(\mathbf{n} \cdot \mathbf{u}_i)$ . This leads to

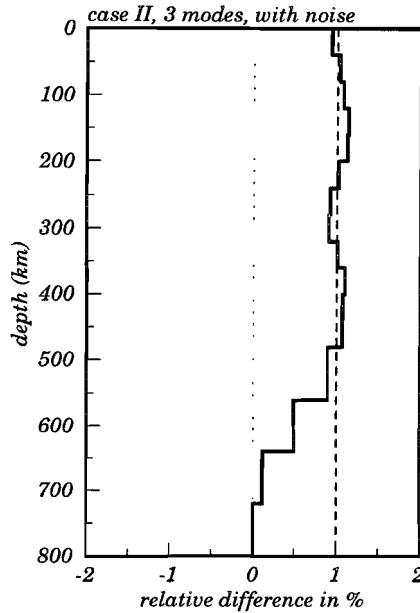


**Figure 3.10** The inversion result (solid line) of the case II inversion of data with three modes and noise. A parameterization of the source term by four Chebyshev polynomials was applied.

the familiar instability associated with small eigenvalues  $\lambda_i$ . Small eigenvalues may now have large influence on the solution.

### 3.4.3 Influence of variation in crustal thickness

Anticipating examples with real data, a final synthetic experiment was carried out in order to see what the influence is on the inversion result of a different crustal thickness in medium  $A$  and medium  $B$ . In this experiment (a case II inversion with only the fundamental mode and no noise in the data) the perturbation of the velocity was confined to a particular depth interval. Figure 3.12a shows the two models for which synthetic seismograms were computed. The first model (dashed line) has a crust of 10 km thickness and the second model (solid line) has a crust with a thickness of 40 km. The crustal  $S$  velocity in both models was set to 3.7 km/s and the upper mantle velocity was set to 4.5 km/s. Figure 3.12b shows the real difference between these two models (dashed line) and the retrieved difference

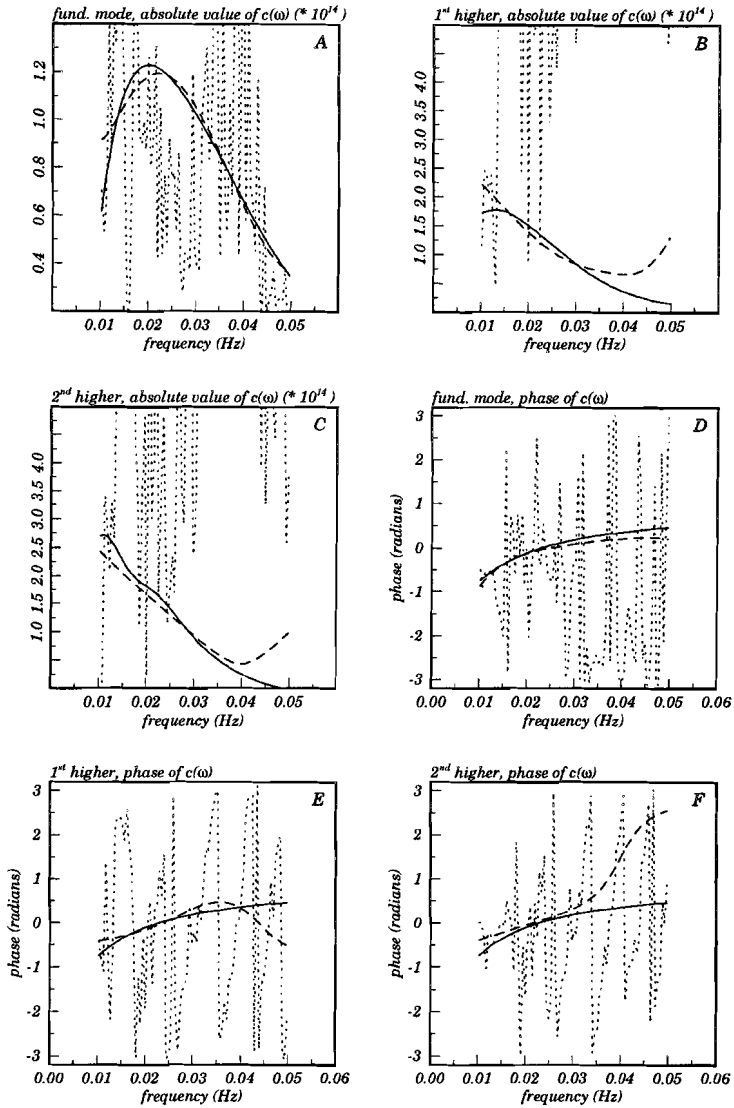


**Figure 3.11** The absolute values and the phases of the exact (solid lines) and estimated (dashed lines) source terms for the individual modes of the inversion of Figure 3.10. The short-dashed lines represent an inversion without parameterizing  $c(\omega)$  by Chebyshev polynomials and the long-dashed lines represent an inversion with  $c(\omega)$  parameterized by four Chebyshev polynomials.

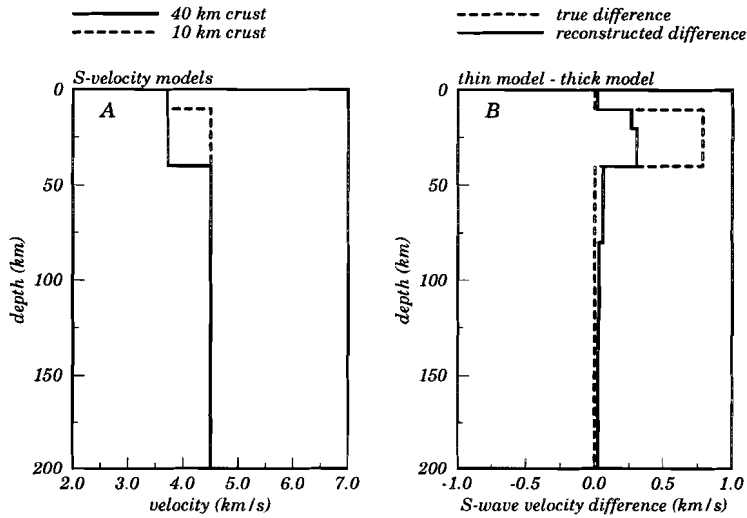


**Figure 3.12** (a) The two models used for the experiment (case II, only the fundamental mode, no noise) to determine the influence on the inversion of a difference in crustal thickness. (b) The true difference between the models (dashed line) and the inversion result (solid line).

(solid line). Because the model perturbations were applied in terms of velocity, the reconstructed model is also displayed in terms of difference in velocity instead of a percentage, but there is no fundamental difference between the two ways of plotting. There are two remarks that should be made about the retrieved model. First, the reconstructed difference in the depth range between 10 and 40 km is about one third of the true difference. This can be due to the nonlinearity of the relation between crustal thickness and phase velocity perturbation or to the fact that a perturbation of a discontinuity not necessarily leads to an equivalent perturbation of the velocities [Snieder and Romanowicz, 1988]. Second (and more important), outside the 10–40 km depth interval the reconstructed perturbation is close to zero. There is almost no smearing of the variation of crustal thickness between 10 km and 40 km to larger depths. This means that the solution for the deeper parts of the model is not affected by a possible difference in crustal thickness between the medium under the path to station *A* and the medium under the path to station *B*.

### 3.5 Real data examples

An example with real data of case I with only the fundamental mode in the signal is given by *Kushnir et al.* [1989]. They determined the average structure between Denmark and the northern part of The Netherlands with the use of two events from Honshu, Japan. They found a model between Denmark and The Netherlands which was consistent with the average geological data for that region. This and the good fits to the observed seismograms indicates the strong resolving power of the technique for case I.

In this section three applications will be shown of case II in western Eurasia. They all relate to the presence of the Tornquist-Teisseyre zone (TTZ, Figure 3.13). This narrow zone (at the surface less than 100 km), strikes from northwest to southeast and separates the old and stable Precambrium continental crust in the northeast (East European Platform, EEP) from the younger and tectonically much more complicated western and Mediterranean part of Europe (Tectonic Europe, TE). Crustal thickness ranges from 25 to 35 km under TE and from 40 to 55 km under the EEP [*Guterch et al.*, 1986; *Meissner*, 1986; *Blundell et al.*, 1992]. For the top of the mantle under the TTZ contrasts of up to 10% in  $S$  velocity are observed, with lower velocities under the younger TE [*Snieder*, 1988; *Zielhuis and Nolet*, 1994; *Lomax and Snieder*, 1994; *Pedersen et al.*, 1994]. At larger depths (300 to 400 km) indications are found for a change of sign of the contrast: the velocities under the EEP become lower than under TE [*Zielhuis and Nolet*, 1994; *Marquering et al.*, 1996].

The data that were used are recordings from the broad-band stations KONO (WWSSN, Norway), NE04 and NE15 (both NARS, The Netherlands). The station locations are depicted in Figure 3.13. Inversions were performed only with the vertical components, because the horizontal components were contaminated with too much noise. Before they could be inverted, the data had to be processed. They were decimated up to 1 sample per second and corrected for instrument response. After a multiple filter analysis the data underwent a time-variable filtering [*Landisman et al.*, 1969] in order to isolate the desired modes from the rest of the signal in the employed frequency band between 20 and 100 s. In the last step, which is only necessary for a case II inversion, a correction was applied for the difference in epicentral distance between the two stations. Consider Figure 3.13 for an impression of the order of magnitude of the differences in epicentral distance. Of the two stations involved in each inversion, the recording belonging to the largest epicentral distance was shifted back using an appropriate reference model. If the station at the largest epicentral distance was situated in TE, the PREM model was used to correct for

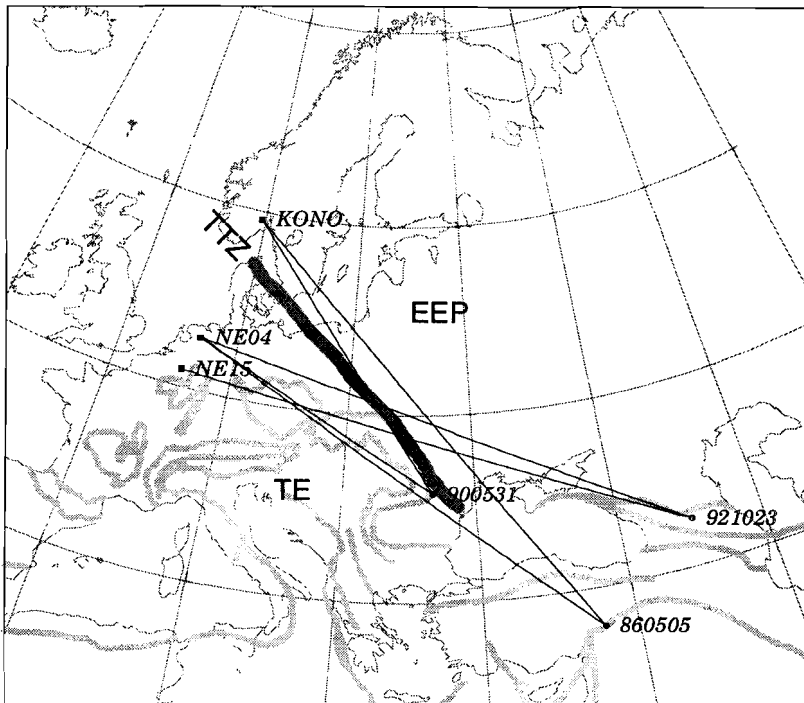


**Figure 3.13** The events (solid circles), stations (solid squares) and great circle paths used for real data inversions. Also indicated are the main European tectonic units. EEP, East European Platform; TE, Tectonic Europe; TTZ, Tornquist-Teisseyre Zone. Grid lines are drawn at  $10^\circ$  intervals.

the difference in epicentral distance. The model that was used for the correction if the station at the largest epicentral distance was situated on the EEP was the model *Zielhuis and Nolet* [1994] used as starting model for their inversions. For the appropriate model the quantity  $\exp(-i k \Delta x)$  was computed for each frequency component, where  $\Delta x$  is the difference in epicentral distance. These frequency dependent phase shifts were subtracted from the recorded phases at the station with the largest epicentral distance. The waveforms of the two stations could then be directly compared with each other. With the dip, rake and the strike the moment tensor elements were calculated, from which the complex radiation pattern  $E(\omega)$  [*Aki and Richards*, 1980] was determined for each event (Table 3.1.). For each of



Date	Time	Lon	Lat	Depth	$M_s$	Dip	Rake	Strike
86/05/05	03:35:38.8	37.8°	38.0°	10	5.9	54	9	260
90/05/31	00:17:48.4	26.8°	45.8°	96	6.0	26	54	90
92/10/23	23:19:45.2	45.1°	42.5°	15	6.5	13	144	302

**Table 3.1** *Event parameters*

these events the difference in the complex radiation pattern between the two takeoff azimuths to station *A* and *B* turned out to be small (in the order of a few percent for the amplitude as well as the phase), so that the assumption of a nearly equal radiation in both directions was not violated. The inversions revealed that the estimated values of the source terms showed a smooth behavior (also for the higher modes), which is comparable to the character of the exact source terms in the synthetic inversions. It was therefore decided to run the inversions without a reparameterization. However, some models resulting from inversions with reparameterization will also be presented for completeness.

The first event of which data were inverted is the May 5, 1986, event in Turkey (Figure 3.13, Table 3.1.) Figure 3.14a shows the vertical recordings in the stations KONO and NE04. The KONO record is corrected for the difference in epicentral distance. Due to the fact that this is a shallow event (10 km) almost all of the energy is contained within the fundamental mode. It is clear that the NE04 recording, which has propagated through the slower TE, arrives later than the faster EEP recording in KONO. The parts of both wavetrains after approximately 1000 s (i.e., the parts containing information on shallower structure) differ mainly in amplitude. This could be due to differences in crustal thickness or interference effects. The part of both wavetrains before 1000 s (containing information on deeper structure) is more coherent than the later part. Therefore, the reconstructed model at larger depths can probably be trusted more than the shallower reconstruction. The reconstructed models resulting from inversions with and without reparameterization of the source term are shown in Figure 3.14b. This figure represents the difference between TE and the EEP relative to the PREM model. A negative difference implies lower velocities under TE and higher velocities under the EEP. The most striking feature is the strong contrast between 8% and 9% below a depth of 80 km. The lower bound of this contrast is not well defined due to the decreasing resolving power of the fundamental mode with depth. This contrast seems to be consistent with

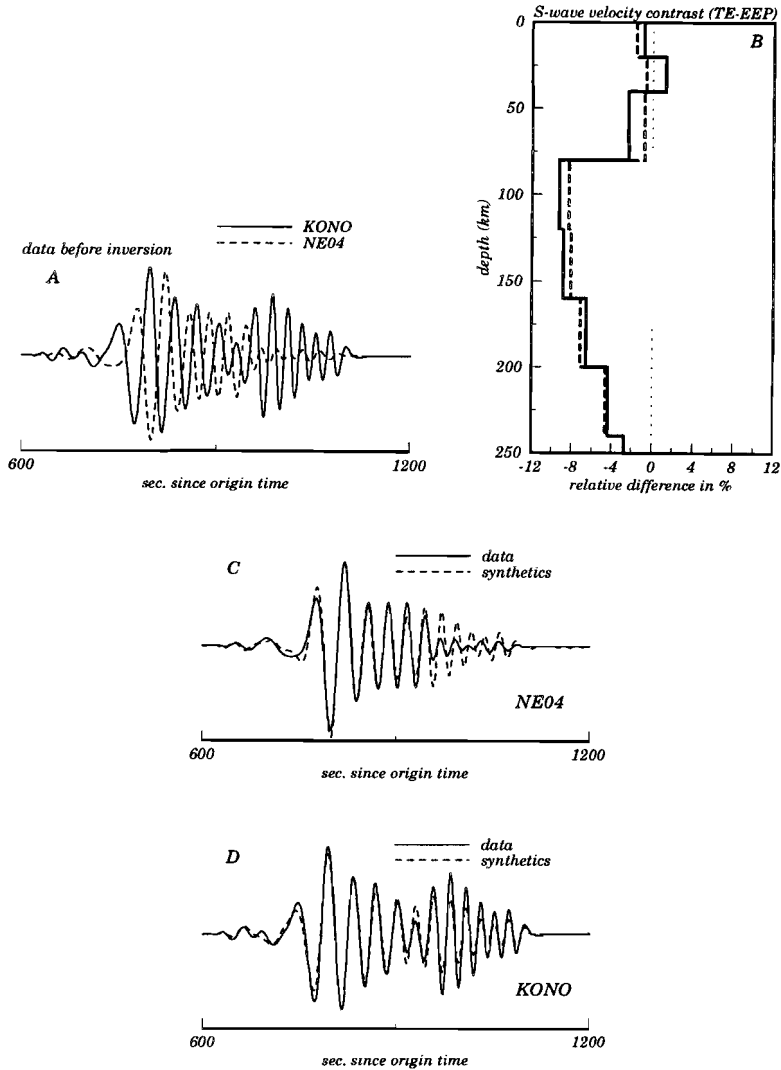


**Figure 3.14** Data and results for the May 5, 1986, event. (a) The vertical components prior to inversion. A correction has been applied to account for the difference in epicentral distance. (b) Solid line:  $S$  velocity contrast obtained from inversion (without reparameterization) of the data of (a). Thick-dashed line: result from inversion with reparameterization by 8 Chebyshev polynomials. (c) The NE04 seismogram (solid line) together with the synthetic seismogram (dashed line) based on the result (solid line) shown in (b). (d) The same as (c), but now for KONO.

other studies [*Alsina and Snieder, 1996; Lomax and Snieder, 1994; Snieder, 1988; Zielhuis and Nolet, 1994*]. The inversion without reparameterization reveals higher velocities under TE than under the EEP between 20 and 40 km depth, whereas the inversion with reparameterization does not. This, together with the fact that the amplitude of this perturbation should be considered with care (see previous section), implies that this contrast can not be interpreted unambiguously as an expression of the thicker crust on the east side than on the west side. Figures 3.14c and 3.14d show the real data and the fits based on the solution without reparameterization of Figure 3.14b. For station KONO the phases are quite well matched, even in the later part of the arrival. Amplitudes are only matched well for the early arriving part of the wavetrain (before 900 s). At NE04 amplitudes and phases are only reasonably fitted up to approximately 1000 s. The bad fit of the following later arrivals may be caused by interference phenomena in the data, which are not accounted for by the inversion. The fits for the inversion with reparameterization are comparable to the fits in Figures 3.14c and 3.14d.

The second example is the inversion of data of the October 23, 1992, event in the Caucasus (Figure 3.13, Table 3.1). In Figure 3.13 it can be seen that both paths propagate through the EEP as well as through TE. However, the part of the path to NE04 that traverses the EEP is longer than the part of the path to NE15 on the EEP. This implies, assuming that the location of the TTZ is the main factor causing differences in dispersion properties between the two paths and that the EEP exhibits higher velocities than TE, that (after correction for the difference in epicentral distance) the wavetrain at NE04 would arrive earlier than the wavetrain at NE15. In Figure 3.15a the vertical recordings at both stations (after correction for the difference in epicentral distance) are shown. As in the previous example, due to the shallow focal depth (15 km) only the fundamental mode is strongly excited. As expected, the wavetrain at NE04 arrives earlier than the wavetrain at NE15. It appears that the later part of the recording in NE04 is dominated by interference effects. The low frequencies in the earlier part of the wave packets seems to be most coherent. Therefore, the deeper part will be again the most reliable part of the model obtained from the inversion. The reconstructed models obtained from inversions with and without reparameterization of the source term are shown in Figure 3.15b. They show the difference relative to PREM between the path to NE15 and the path to NE04. The time shift in the data (Figure 3.15a) is translated into an approximately 1% lower velocity for the southern path than for the northern path. The amplitude of the contrast is strongly diminished compared to the amplitude of the reconstructed contrast for the 1986 event (Figure 3.14b), because now the contrast over the TTZ is smeared out over the entire path length

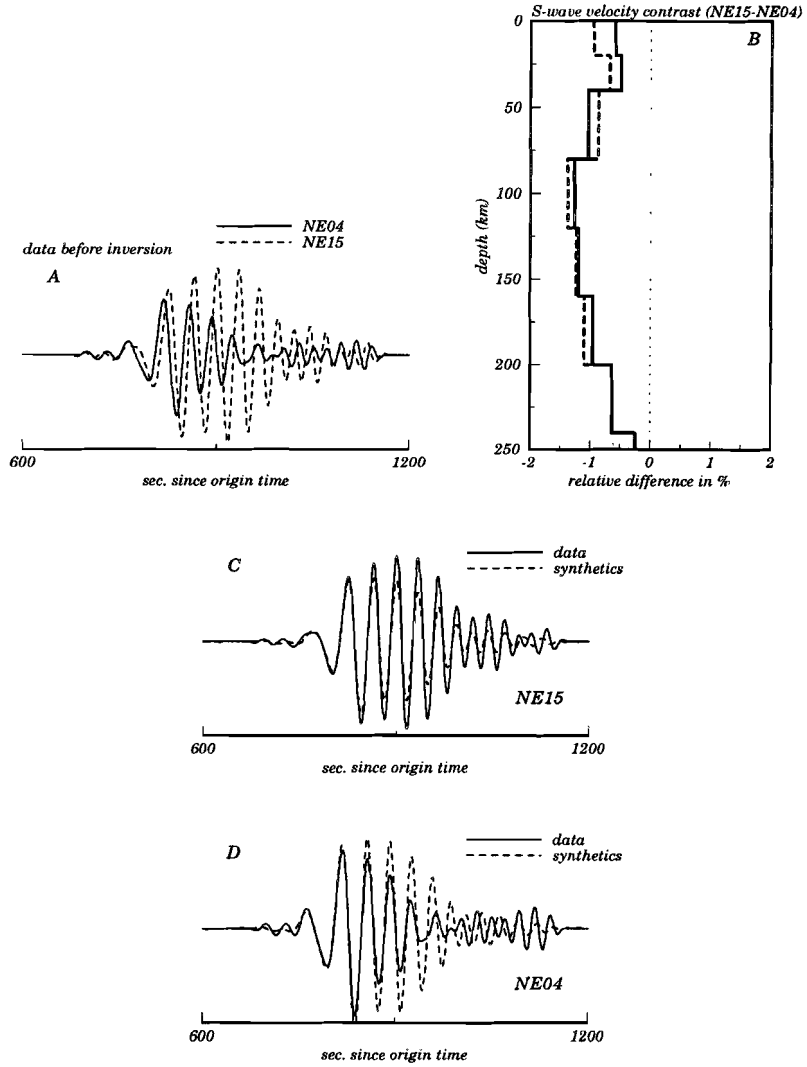


**Figure 3.15** The same as Figure 3.14, but now for the October 23, 1992, event in the Caucasus, recorded at NE04 and NE15.

(see equation (3.7)). *Snieder* [1987] showed that the deflection from the great circle direction at the receiver, ( $D_r$ ), is given by the path integral of the normal derivative of the phase velocity contrast:

$$D_r = \frac{1}{\Delta} \int_0^{\Delta} s \partial_{\perp} \left( \frac{\delta c}{c} \right) ds , \quad (3.12)$$

where  $\Delta$  is the epicentral distance and  $s$  the distance along the ray path. Note that this equation is of the same form as equation (3.7). *Woodhouse and Wong* [1986] presented an equivalent form of equation (3.12). If it is assumed that the obtained average  $S$  velocity contrast of about 1% results in a phase velocity contrast of the same strength, a deviation of about  $9^\circ$  from the great circle is predicted by equation (3.12). This coincides well with results obtained from a recent beamforming analysis by *Alsina and Snieder* [1996]. Figures 3.15c and 3.15d show the data and the fits to the data resulting from the inversion without reparameterization. Although the amplitudes are not perfectly fitted for NE15, the phases are well fitted, except for the very last part of the wavetrain. For NE04 only the lowest frequencies are matched; the higher frequencies probably suffer from interference effects that are not accounted for by the theory. The fits for the inversion with reparameterization are comparable to the fits in Figures 3.15c and 3.15d.

The final example concerns a deeper event which beside the fundamental mode also excited significant higher mode energy. The event occurred in Romania, May 31, 1990, at a depth of 96 km (Figure 3.13, Table 3.1). Recordings in KONO and NE04 were used for inversions without reparameterization. In the data a clear higher mode arrival can be observed (Figure 3.16a). After generating synthetic seismograms with different number of modes for this event and comparing these synthetic waveforms with the recorded waveforms, it was decided to assume that in these data the energy was carried by the fundamental mode and the first higher mode. From the waveforms, which do not contain significant interference effects due to the deep source, the path to KONO (mostly east of the TTZ) appears to be faster than the path to NE04 (west of the TTZ). Three inversions were carried out: one inversion in which the complete waveforms were fitted with the fundamental and the first higher mode, one inversion in which the complete waveforms were fitted with only the fundamental mode and one inversion where the fundamental mode in the signal was fitted with the fundamental mode. For this last inversion the higher mode energy was removed using time-variant filtering. The three models obtained by the inversions are shown in Figure 3.16b. Both thick dashed lines indicate the models after the inversions for one mode. The reconstructed model perturbations are similar to the model shown in Figure 3.14b, although the amplitude of the contrast

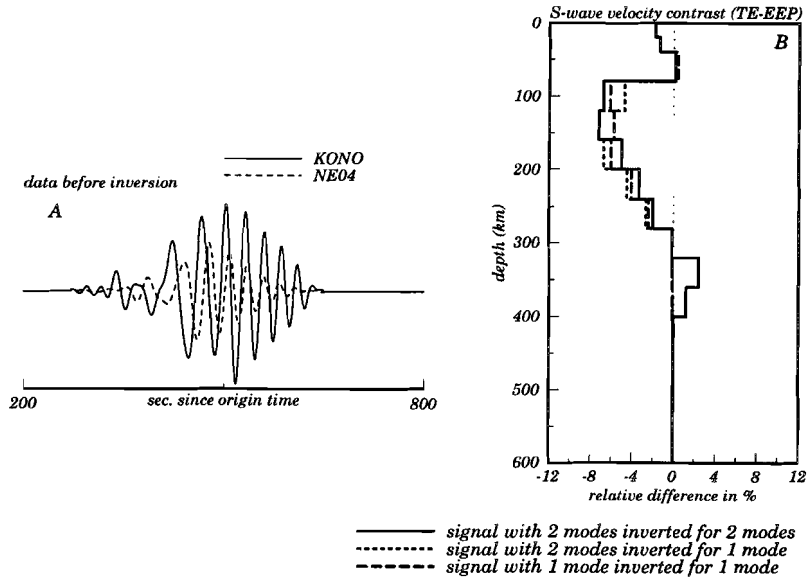


**Figure 3.16** Data and results for the May 31, 1990, event. (a) The waveforms prior to inversion. (b) The inversion results for the three experiments described in the text.

is somewhat less in Figure 3.16b than in Figure 3.14b. This might be caused by the fact that the path to KONO for the 1990 event is not entirely through the EEP. As the contrast will be smeared out along the total path, the amplitude of it will slightly diminish. In addition, the term  $D(s)$  in equation (3.7) is smaller for the event of Figure 3.16 than for the event of Figure 3.14. In Figure 3.16b it can be seen that the results of the inversions for one mode (dashed lines) do not reveal any significant structure at depths greater than 250 km. This changes when the complete waveforms are inverted for two modes (solid line). Between 300 km and 400 km depth a contrast is revealed with higher velocities under TE than under the EEP. A similar reversal of the velocity contrast around the TTZ was also observed by Zielhuis and Nolet [1994]. Figures 3.17a and 3.17b show that the synthetic data fit the real data extremely well for the inversion of the complete signal for two modes. The amplitudes and phases are better fitted than in Figures 3.14 and 3.15, probably because there are less indications for interference in the seismograms and because the difference in the amplitudes of the excitation term for the takeoff directions to

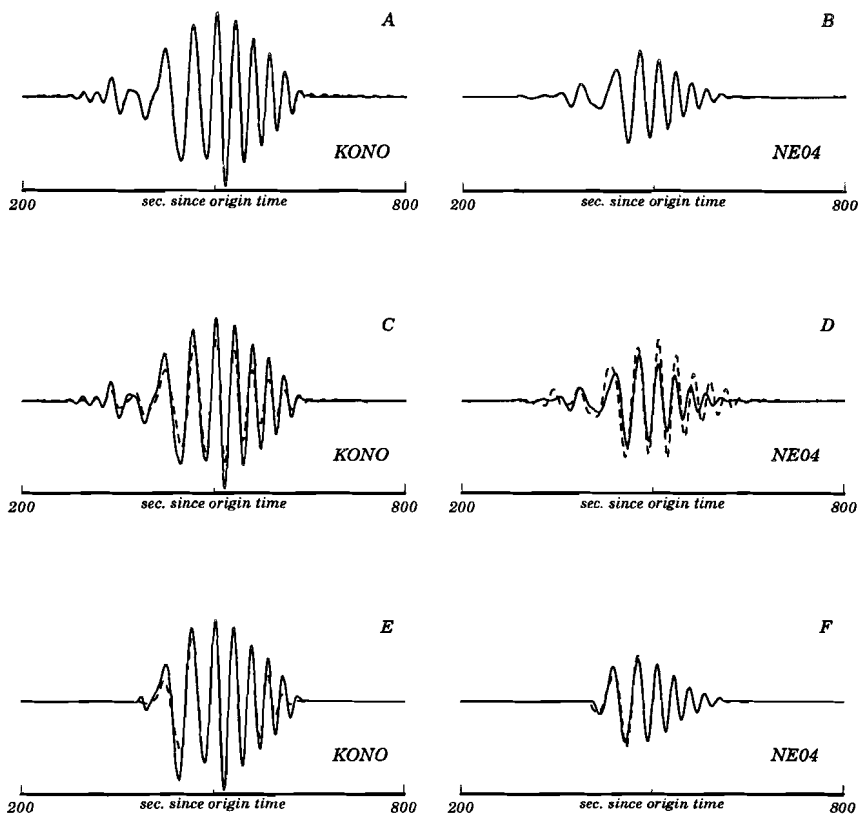


**Figure 3.17** (a)-(f) The original (solid lines) and synthetic (dashed lines) waveforms for the different experiments described in the text with the data of the May 31, 1990, event. (a)+(b) Two modes fitted with two modes. (c)+(d) Two modes fitted with one mode. (e)+(f) One mode fitted with one mode.

KONO and NE04 is smaller than in the previous examples. If the complete signal with two modes is fitted with only the fundamental mode, the fits of Figures 3.17c and 3.17d are obtained. At NE04 the inversion fails to fit the higher mode and also the fundamental mode is poorly fitted, even the phases. At KONO the fit is better, but not as good as the fit of the complete signal with two modes. The degraded fits can be explained by the fact that the source term  $\hat{c}$  is completely erroneously estimated, because a source term for only one mode is determined, while two modes are contained within the signal. Finally, the results for the case where the signal with the higher mode removed was inverted for only the fundamental mode are shown in Figures 3.17e and 3.17f. The fits are better than in Figures 3.17c and 3.17d. The experiments with the 1990 Romania event confirm that including higher mode information in the inversion is possible and gives more resolution at depth. Furthermore, if the waveforms are not inverted for the actual number of modes that they contain, the retrieved model may be reasonable, but the fits to the data deteriorate.

## 3.6 Conclusions

Using one source and two stations, the method described in this paper provides a powerful tool to image either the local  $S$  velocity structure between the two stations (if they lie on the same great circle, case I) or the path-averaged horizontal  $S$  velocity contrast between the structures under the two paths from the source to the stations (case II). Because the data depend via a linear functional on the contrast, it could be worthwhile to combine results of studies using polarization data, which depend in a similar way on a contrast in a model, with results obtained from a study using the method described in this paper. An advantage of the presented method is that only two surface wave recordings are needed to produce a result. At the same time this may also be a drawback of the method, because the data need to be of high quality. It has been shown that the applicability of case I is limited to the use of the fundamental mode only. In that case, the method does not differ much from the classical two-station method. If also higher modes are present in the signal, the phase differences between the recordings in both stations can not be attributed solely to the region between the two stations, where this is implicitly assumed in the method. When case II is under consideration, higher modes can be included in the analysis, which yields resolution at depths where no resolution is achieved with only the fundamental mode. Another advantage of the method is that no *a priori* knowledge of the source mechanism or the medium between the



source and the nearest receiver is necessary. These parameters are combined into a single quantity (the source term) which is estimated by the algorithm. Inversion experiments of synthetic data without noise showed that either this source term is determined correctly (if only the fundamental mode is present in the signal) or the estimated source term deviates from the correct value, but these deviations are in the null-space (for an inversion of data containing three modes). In the latter case, a parameterization of the source term by Chebyshev polynomials improved the estimation of the source term considerably, although this reparameterization is not necessary to obtain reasonable model parameters by the inversion. However, for the synthetic inversion of data containing three modes *with* noise, the reparameterization of the source term turned out to be necessary. The noise caused the estimates of the source term to deviate from the exact values in such a way that the obtained model parameters were unacceptable. In general, reparameterization of the problem is a way to reduce the number of degrees of freedom and to stabilize the inversion with respect to noise. The high number of degrees of freedom may cause the estimates of the source term to exhibit oscillatory behavior, while the exact source term is much smoother.

The method is based on an algorithm developed by *Kushnir et al.* [1988, 1989]. The extensions made in this paper consist of the introduction of a way to solve a horizontal contrast (case II), the extension to higher modes and the attention paid to the source term (reparameterization). Three examples with real data concerning the Tornquist-Teisseyre zone from the Black Sea to southern Scandinavia demonstrate the power of the algorithm: obtaining useful *S* velocity gradient information with only a few waveforms. Including higher mode energy increases the depth range of interest. The results with the data around the TTZ indicate that strong gradients may exist over small distances: the 9% velocity contrast in the upper mantle beneath the central part of the TTZ is contained within a width of at most 600 km. As this may occur on numerous other places on earth, this supports the conclusions of Chapter 2 that neglecting these kind of structures when considering the entire globe is not obvious. To outline a feature like a transition zone in the mantle, such as the TTZ, more accurately, additional data will be needed (e.g., more source-receiver paths or polarization measurements). Concluding, it can be said that the algorithm presented in this paper is not designed to provide three-dimensional images of specific regions, but it can be useful to add easily obtainable results as constraints to inversions that do aim to monitor complete three-dimensional structure.

# Chapter 4

## Correlation between shear-wave upper mantle structure and tectonic surface expressions: application to central and southern Germany

**Abstract** We have inverted fundamental mode Rayleigh waveforms in the frequency range from 20 to 100 s to obtain a three-dimensional  $S$  velocity distribution beneath central and southern Germany. The data come from 27 teleseismic events recorded at 17 broadband stations in Germany and adjacent areas. This results in 56 paths between pairs of stations, each pair lying on the same great circle with an epicenter. The phase differences between the waveforms recorded at a pair of stations have been inverted directly for the path-averaged  $S$  velocity perturbation between the two stations. All path models were then combined into a single three-dimensional model. The most prominent features of the obtained model are (1) low velocities beneath the Eger Graben, which are an expression of the deep-reaching rift structure, (2) high velocities between 40 and 120 km depth beneath northern Bavaria, caused by an apparent thickening of the lithosphere towards the south, (3) high velocities in the uppermost mantle beneath the southern Rhine Graben area (presently inactive with respect to rifting), suggesting the absence of present upwelling hot mantle material, and (4) low velocities beneath the presently experiencing rifting northern branch of the Central European rift system, including the northern part of the Rhine

---

<sup>1</sup>This chapter has been accepted for publication in *J. geophys. Res.* (Geodynamics Research Institute (Utrecht University) publication 96.034).

Graben and the Rhenish Massif west of the river Rhine with the volcanic fields of the Eifel. These reduced velocities indicate a broad updoming of the lithosphere-aesthenosphere boundary. Our model suggests a strong correlation between upper mantle  $S$ -wave structure at depths down to 200 km and tectonic surface expressions.

## 4.1 Introduction

Germany (Figure 4.1) is an interesting area for geodynamic research. Features such as the Rhine Graben, the volcanism in the Eifel, and the fact that the area lies just north of the Alps, which are an expression of a large collision process, make Germany a region which has attracted the attention of earth scientists over the years. The study in this paper is focussed on the shear-wave velocity structure beneath central and southern Germany. Although we acknowledge that there is a difference between  $P$  and  $S$  velocity structures [e.g., *Gutenberg*, 1953, 1959], we feel that it is appropriate to mention also some results of  $P$  wave studies in this introduction, because in general  $P$  and  $S$  velocity models correlate quite well (compare for instance the  $P$  velocity model of *Spakman et al.* [1993] and the  $S$  velocity model of *Zielhuis and Nolet* [1994]). Many regional seismological studies have been carried out using data from the Gräfenberg Array in central Germany [e.g., *Buttkus*, 1986; *Hadiouche et al.*, 1991; *Harjes and Seidl*, 1978]. Also the Rhine Graben area has been the subject of many regional seismological studies [e.g., *Glahn and Granet*, 1992; *Glahn et al.*, 1993; *Granet*, 1986; *Reichenbach and Mueller*, 1974; *Seidl et al.*, 1970]. Besides seismological studies, rheological, gravitational, and petrological studies have contributed to a better understanding of different small-scale features beneath the Rhine Graben [*Fuchs et al.*, 1987; *Glahn et al.*, 1992; *Gutscher*, 1995; *Illies and Fuchs*, 1974; *Illies and Mueller*, 1970; *Kahle and Werner*, 1980]. Comprehensive reviews of the crustal and upper mantle structure beneath the Rhine Graben are provided by *Prodehl et al.* [1992, 1995]. In addition to the studies on a local scale using a variety of geophysical methods there are also several three-dimensional seismological models available on a continental scale, such as the  $S$  velocity models of *Marquering et al.* [1996], *Snieder* [1988] and *Zielhuis and Nolet* [1994] or the  $P$  velocity model of *Spakman et al.* [1993]. The local studies mainly investigate crustal properties related to the geology of the area and are often related to  $P$ -wave structure. We want to try to bridge the gap between the studies on a local and on a continental scale by covering a regional area larger than the areas that have been studied on a local scale, but smaller than the existing continental-scale models for Europe. On this scale, we aim to make the connection between expressions of surface

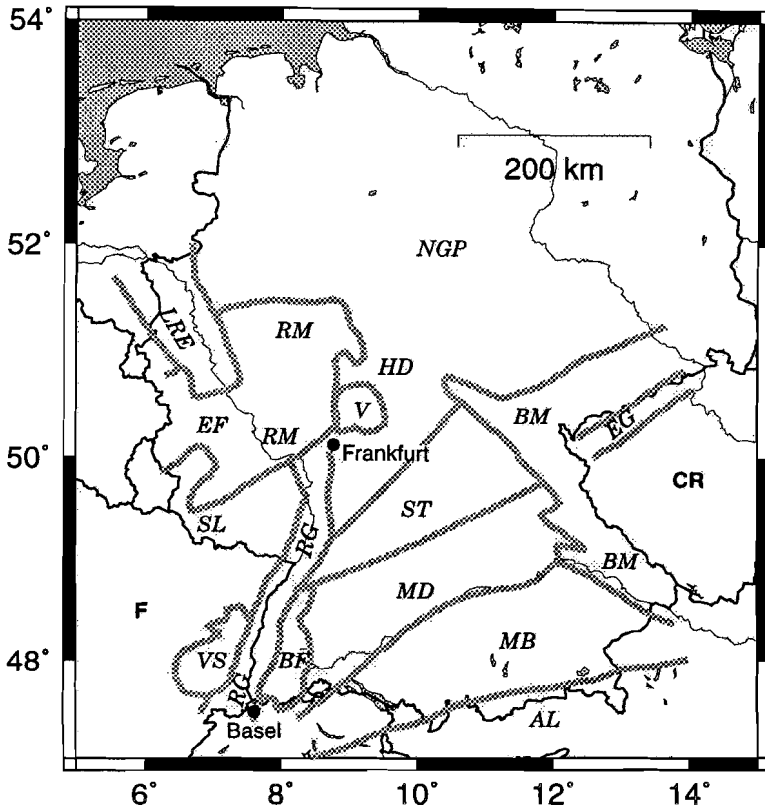


**Figure 4.1** Sketch of the main geographic and tectonic units in the area investigated in this study. RM, Rhenish Massif; EF, Eifel; SL, Saarland; V, Vogelsberg; HD, Hessen Depression; NGP, North German Plain; RG, Rhine Graben; LRE, Lower Rhine Embayment; VS, Vosges; BF, Black Forest; ST, Saxothuringian Zone; MD, Moldanubian Zone; MB, Molasse Basin; AL, Alps; BM, Bohemian Massif; EG, Eger Graben; F, France; CR, Czech Republic.

geology and shallow upper mantle structure. *Stange and Friederich* [1993] recently determined an average one-dimensional  $S$  velocity profile from the dispersion of fundamental mode Rayleigh waves for southern Germany. Earlier publications on  $S$  velocity beneath Europe include those by *Knopoff* [1972], *Lehmann* [1961], *Mayer-Rosa and Mueller* [1973], *Panza* [1985], *Panza and Mueller* [1978], *Panza et al.* [1980], and *Seidl and Mueller* [1977].

Since a few decades, surface waves have proven to be a useful tool to study crustal and mantle structure [*Press*, 1956]. *Passier and Snieder* [1995a] recommend the use of paths that are relatively short with respect to the wavelengths in order to map small-scale heterogeneities properly. In this paper, we use surface waves to investigate the three-dimensional  $S$  velocity structure beneath central and southern Germany.

## 4.2 Method and Data

The method used in this paper to derive a three-dimensional  $S$  velocity model from surface wave recordings consists of two steps. In the first step, which is based on an algorithm originally proposed by *Kushnir et al.* [1988, 1989] (hereinafter referred to as KLL), a set of one-dimensional horizontally averaged  $S$  velocity depth profiles is obtained. The second step, a linear inversion of these one-dimensional constraints, yields a laterally and with depth varying  $S$  velocity model. For more details and extensions to several other applications of the KLL algorithm the reader is referred to *Passier and Snieder* [1995b].

We have used 56 paths from 27 events recorded in 17 broadband stations (Figure 4.2, Tables 4.1 and 4.2). Most of the stations belong to the German Regional Seismic Network, but also broadband stations in Zürich (ZUR), Stuttgart (STU), Walferdange (WLF), Echery (ECH), Krefeld (NE39), Witteveen (WIT), and Epen (HGN) were included. Additionally, we have used broadband data coming from a station belonging to the Gräfenberg array (GRF) [*Harjes and Seidl*, 1978]. The waveforms used as data for the KLL algorithm were the vertical components of the fundamental mode of direct Rayleigh waves with periods between 20 and 100 s. An instrument correction and a time-variant filtering [*Landisman et al.*, 1969] were applied to the original seismograms to isolate the desired wave trains from the rest of the signal. Average  $S$  velocity perturbation depth profiles relative to the PREM model [*Dziewonski and Anderson*, 1981] with a crustal thickness of 30 km have been obtained along the paths in central and southern Germany (Figure 4.2) with the model parameterized by six layers down to a depth of 200 km.

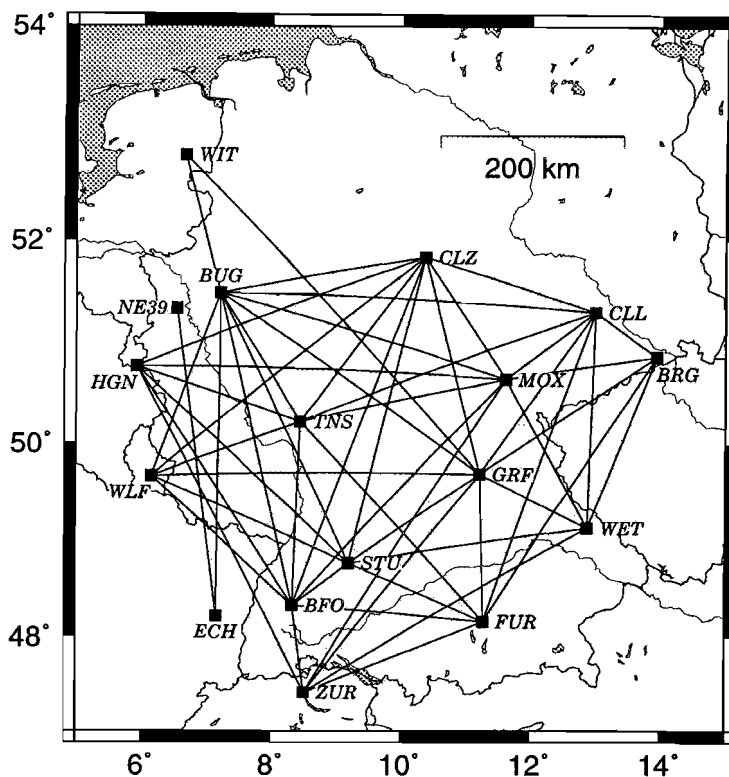


**Figure 4.2** The 17 stations (filled squares) and the 56 paths in central and southern Germany and vicinity that were used in this study

The variations in the depth of the Moho discontinuity beneath central and southern Germany appear to be minor [Gutscher, 1995; Meissner *et al.*, 1987; Zeis *et al.*, 1990], except for the severe change of Moho depth in rift structures. Whereas normal Moho depth is about 30 km, it reduces to around 24 km beneath the southern Rhine Graben, possibly affecting the final velocity model. An experiment was done in order to determine how the change in Moho depth under a rift influences the recovered velocity model. Figure 4.3a shows the result of using synthetic waveforms at two stations separated by 250 km for a model with the Moho discontinuity at 24 km depth and then inverting these data. An *S* velocity contrast across the Moho implied a perturbation relative to the reference model of 10% between 24 and 30 km

Station	Lon	Lat
BFO	8.53 E	48.33 N
BRG	13.95 E	50.77 N
BUG	7.21 E	51.59 N
CLL	13.20 E	51.31 N
CLZ	10.57 E	51.84 N
ECH	7.16 E	48.12 N
FUR	11.48 E	48.16 N
GRF	11.42 E	49.69 N
HGN	5.92 E	50.67 N
MOX	11.82 E	50.65 N
NE39	6.39 E	51.34 N
STU	9.40 E	48.77 N
TNS	8.65 E	50.22 N
WET	13.08 E	49.14 N
WIT	6.87 E	52.81 N
WLF	6.15 E	49.57 N
ZUR	8.71 E	47.41 N

**Table 4.1** *Stations used*

depth (the dashed line in Figure 4.3a). The solid line in Figure 4.3a shows that the reconstructed velocity perturbation is mainly restricted to depths shallower than 40 km. Since there is almost no smearing to larger depths, the differences in crustal structures do not significantly affect the model below 40 km depth.

Figure 4.3b shows the result of a test using synthetic data where a perturbation of 5% was applied to the upper 80 km of the reference model. This test, similar to the one described earlier, was done to investigate the influence of lithospheric perturbations on deeper structure within the inversion. Figure 4.3b shows that the reconstructed velocity perturbation is in good agreement with the 5% of the input model, without significant smearing to larger depths, indicating that no artifacts occur due to lithospheric anomalies.

The 56 path-averaged  $S$  velocity perturbation depth profiles were combined into a three-dimensional  $S$  velocity perturbation model of the crust and upper mantle by linear inversion. For this purpose, the area of interest was rotated to the equator,

Date	Time (UTC)	Lat	Lon	M <sub>s</sub>	Region
91/05/30	13:17:44	54.5 N	161.6 W	6.7	Alaska
91/07/13	02:50:14	42.1 N	125.6 W	6.9	Oregon
91/12/22	08:43:13	45.5 N	151.1 E	7.4	Kurils
92/09/09	13:08:55	76.2 N	6.7 E	5.7	Svalbard
94/05/26	08:26:52	35.4 N	4.1 W	5.7	Gibraltar
94/06/06	20:47:43	3.0 N	76.2 W	6.4	Colombia
94/06/20	09:09:04	29.1 N	52.6 E	5.8	Iran
94/09/01	15:15:52	40.3 N	125.8 W	6.9	California
94/10/27	17:45:56	43.6 N	127.3 W	5.9	Oregon
94/11/09	18:21:04	43.7 N	147.2 E	6.1	Kurils
94/12/10	16:17:35	18.0 N	101.2 W	6.3	Mexico
95/01/06	22:37:35	40.3 N	142.2 E	6.9	Honshu
95/01/12	10:26:47	44.1 N	147.0 E	6.2	Kurils
95/01/22	02:38:11	41.6 N	29.3 W	5.1	Azores
95/01/26	07:00:46	36.4 N	71.0 E	5.7	Afghanistan
95/02/10	20:26:59	19.5 S	68.6 W	5.6	Chile
95/02/12	20:13:36	59.6 N	153.1 W	5.5	Alaska
95/02/23	21:03:05	35.1 N	32.3 E	5.8	Cyprus
95/03/01	02:04:24	55.7 N	161.2 E	5.4	Kamchatka
95/03/14	17:33:30	54.8 N	161.4 W	5.9	Alaska
95/04/29	11:50:53	1.3 S	28.3 E	5.5	Zaire
95/05/04	02:18:48	1.8 N	128.4 E	6.1	Halmahera
95/05/13	08:47:15	40.0 N	21.6 E	6.6	Greece
95/05/16	03:35:02	36.4 N	70.9 E	5.7	Afghanistan
95/05/27	13:03:55	52.5 N	142.9 E	7.6	Sakhalin
95/06/15	00:15:51	38.4 N	22.2 E	6.5	Greece
95/06/25	06:59:07	24.9 N	121.8 E	5.9	Taiwan

Table 4.2 *Events used*



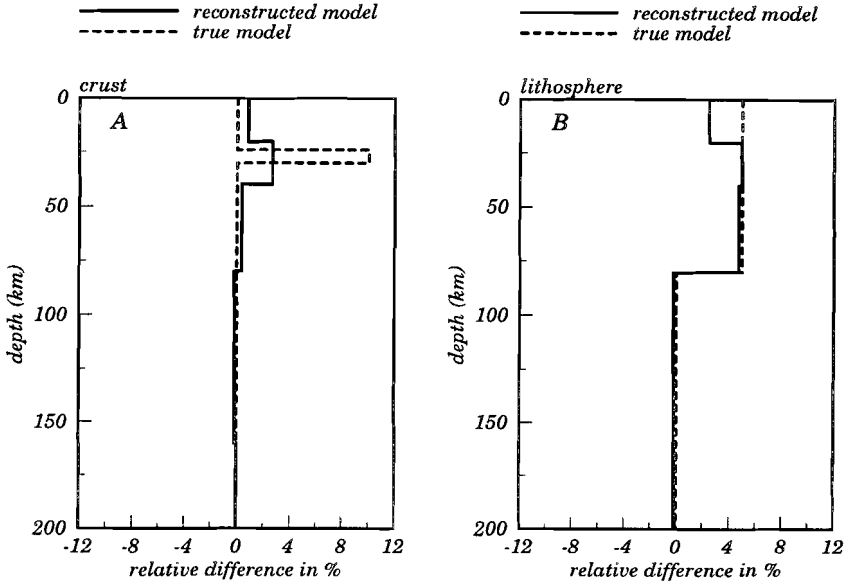


**Figure 4.3** (a) Synthetic test to show the influence of a variation in crustal thickness. The dashed line is the input model, which differs from the reference model between 24 and 30 km depth due to the difference in crustal thickness. The solid line is the inversion result. (b) The input model (dashed line) is the reference model perturbed by 5% in the upper 80 km. The model after waveform inversion is shown by the solid line.

with the equator running eastward through the point which corresponds to  $10^{\circ}\text{E}$ ,  $50.5^{\circ}\text{N}$ . Using a Cartesian projection, it was laterally parameterized by 225 discrete cells, each of which measured  $0.47^{\circ} \times 0.47^{\circ}$ . Thus the following linear system had to be solved for each individual layer:

$$\begin{bmatrix} A \\ \lambda D \end{bmatrix} \mathbf{m} = \begin{bmatrix} \mathbf{d} \\ 0 \end{bmatrix}, \quad (4.1)$$

where  $A$  is the matrix relating the model to the data,  $D$  is a regularization term (weighted by  $\lambda$ ) to minimize the horizontal gradient of the model,  $\mathbf{m}$  is the model vector, and  $\mathbf{d}$  is the data vector with the path-averaged  $S$  velocity perturbations from the KLL algorithm. This system was solved with the LSQR algorithm [Paige

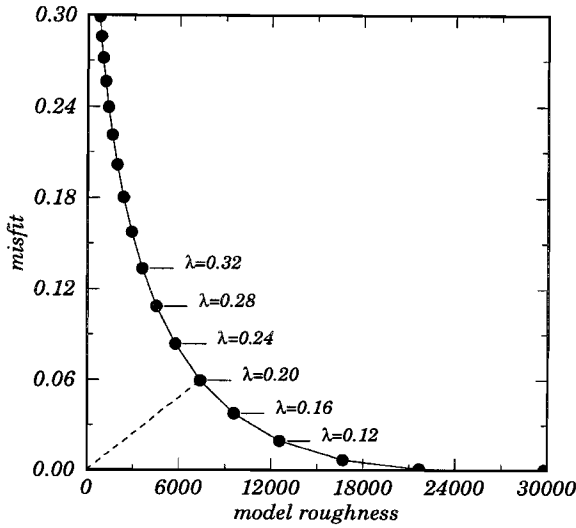


**Figure 4.4** Trade-off curve for the third layer (between 40 and 80 km) of data misfit versus model roughness. Some values of the smoothing weight  $\lambda$  are indicated along the curve. Other points are at intervals of 0.04. The point  $\lambda = 0.20$  is closest to the origin.

and Saunders, 1982] to find the model  $\mathbf{m}$  that minimizes the misfit  $M = |\mathbf{A}\mathbf{m} - \mathbf{d}|^2 + \lambda|\mathbf{D}\mathbf{m}|^2$ . The value of  $\lambda$  was determined from the trade-off curve of data misfit  $\mu$  versus model roughness  $r$ , which are defined by

$$\mu = \frac{\sum_{i=1}^{56} (d_i - \tilde{d}_i)^2}{\sum_{i=1}^{56} (d_i)^2} , \tag{4.2}$$

and

$$r = \iint |\nabla\mathbf{m}|^2 dx dy ,$$

respectively. In (4.2),  $d_i$  are the *S* velocity perturbations as found by the KLL algorithm and  $\tilde{d}_i$  are the average perturbations as predicted by the three-dimensional model  $\mathbf{m}$  along a path. For different values of  $\lambda$  the quantities  $\mu$  and  $r$  were computed for all layers. As an example, Figure 4.4 shows the trade-off curve of  $\mu$  versus  $r$  for the layer between 40 km and 80 km depth. The point  $\lambda = 0.20$  is closest to the origin. This value of  $\lambda$  was used to construct the final model, as the other layers showed similar curves.

### 4.3 Model

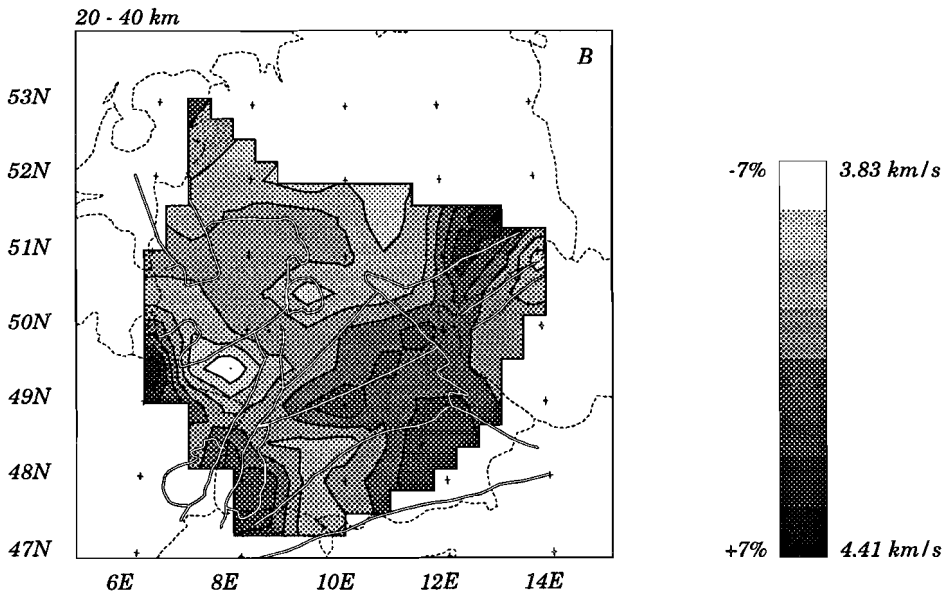
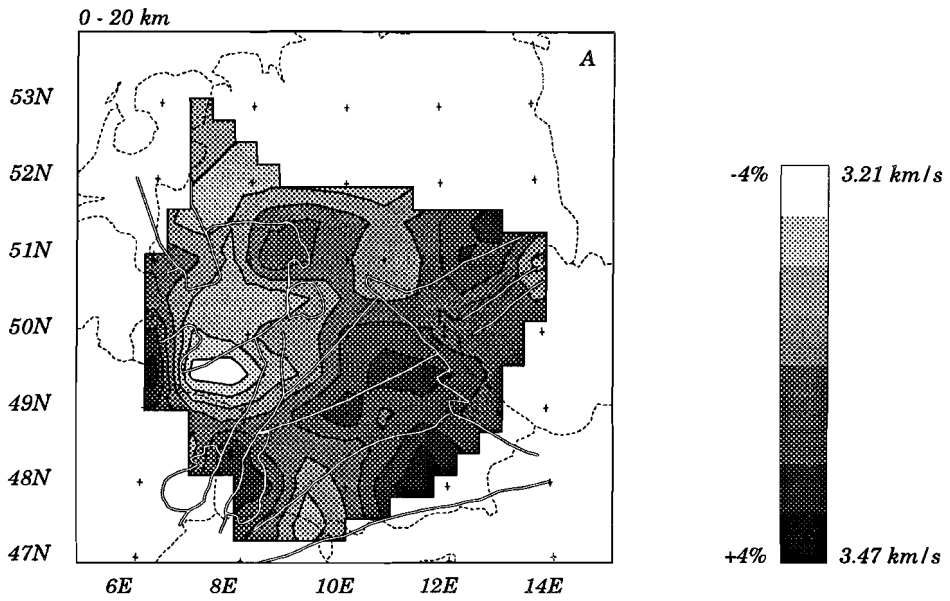
Figure 4.5 shows the six layers of the final model. The perturbations are contoured with respect to the mean perturbation for that specific layer. Light shading indicates negative  $S$  velocity perturbations, dark shading indicates positive  $S$  velocity perturbations. The ranges of the velocity perturbations as well as the ranges of the absolute  $S$  velocity values are indicated in the legend bars. The model is not shown outside the area spanned by the rays. Note that the perimeter of this area does not coincide with the boundaries of the cells used to parameterize the model in the inversion.

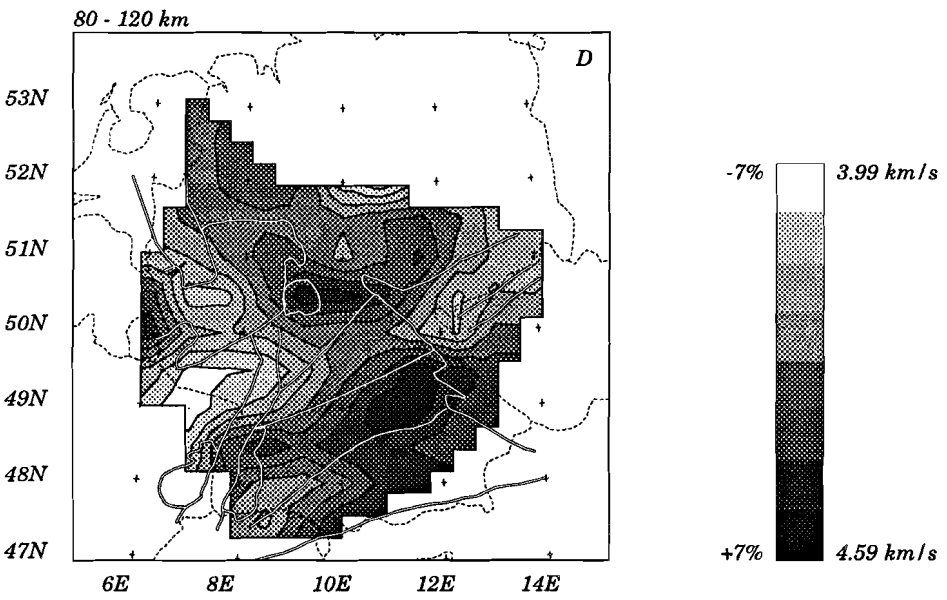
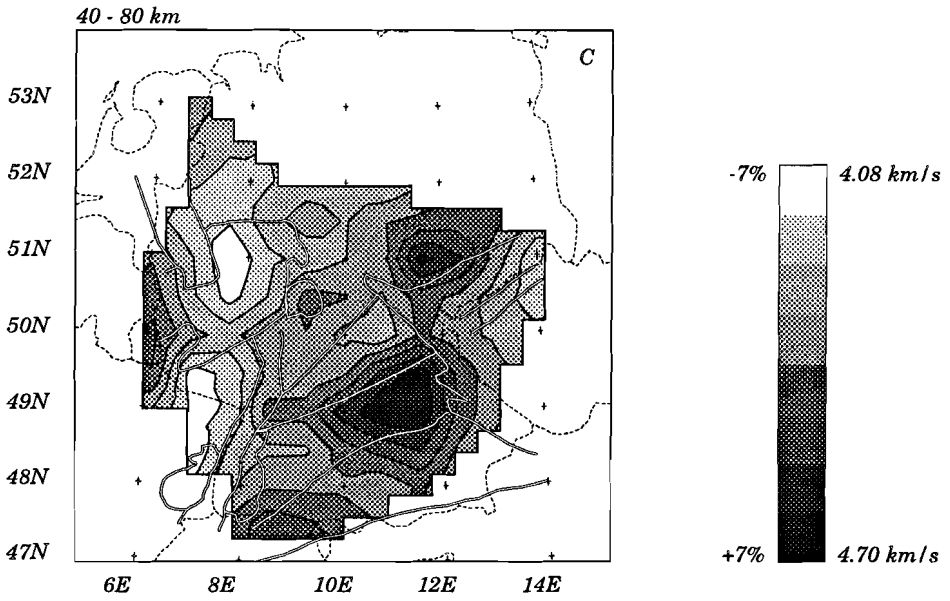
A misfit reduction  $\varepsilon$  can be defined for each layer in the linear inversion as  $\varepsilon = 100\% \times (1 - \mu)$  (with  $\mu$  defined in (4.2)). Going from the shallowest layer downward, we obtained values for  $\varepsilon$  of 91.3%, 88.0%, 94.3%, 79.3%, 74.6%, and 74.8%, respectively. It is clear that the model explains the majority of the data (the  $S$  velocity perturbation depth profiles) used for the linear inversion. Another measure of the quality of the model is the misfit reduction with respect to the original waveforms. This quantity is defined by the average of the individual waveform misfit reductions for the separate paths:

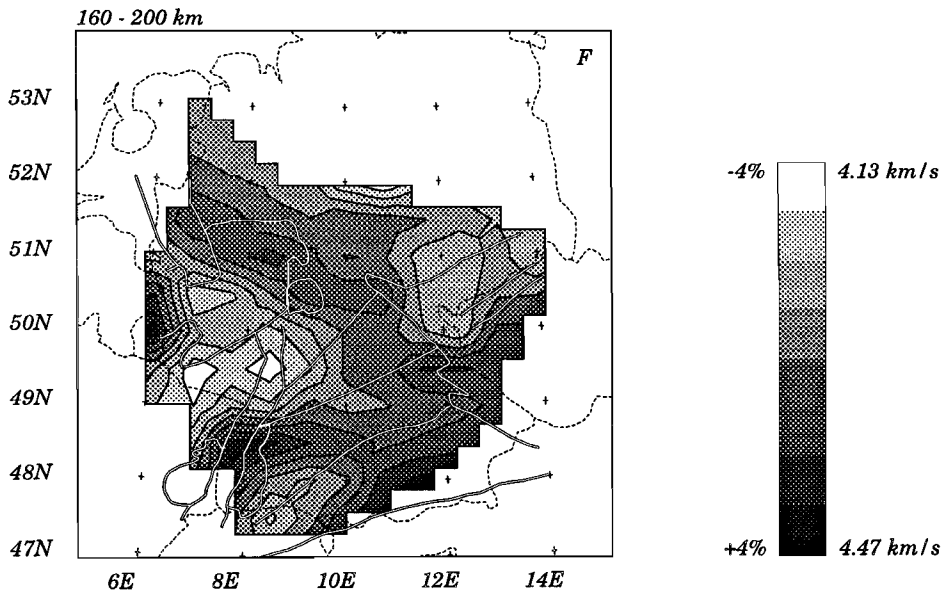
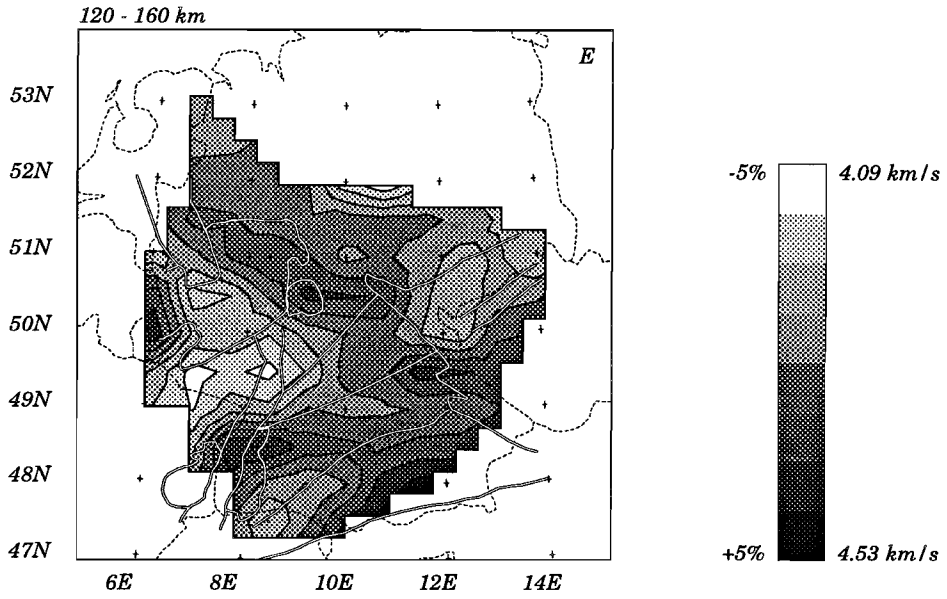
$$\eta_j = 100\% \times \left[ 1 - \frac{\sum_i \|s_{ij} - \tilde{s}_{ij}\|^2}{\sum_i \|s_{ij}\|^2} \right] . \quad (4.3)$$

In (4.3),  $\eta_j$  is the waveform misfit reduction for the  $j^{\text{th}}$  path,  $s_{ij}$  the complex spectral value for the  $i^{\text{th}}$  frequency component of the waveform recorded at the station with the largest epicentral distance (for path  $j$ ), and  $\tilde{s}_{ij}$  the complex spectral value of the synthetic waveform according to the model. Using the averages of the model in Figure 4.5 along the paths of Figure 4.2 results in a waveform misfit reduction of 84.5%. However, this number is not as well suited for measuring the quality of the model as the misfit reductions  $\varepsilon$  listed above. This is because the KLL algorithm is most sensitive to a misfit of the phase rather than the amplitudes. An amplitude mismatch between the data and the synthetics therefore contributes to the misfit,

**Figure 4.5** *On the next three pages: the six layers of the final shear-wave velocity model below Germany. The range of the perturbations (relative to the layer mean) is plotted to the left side of the legends and the range of absolute  $S$  velocities is plotted to the right side of the legends. The depth interval of the layers is given in each frame title. Also indicated are the main geographic and tectonic units, which are explained in Figure 4.1.*







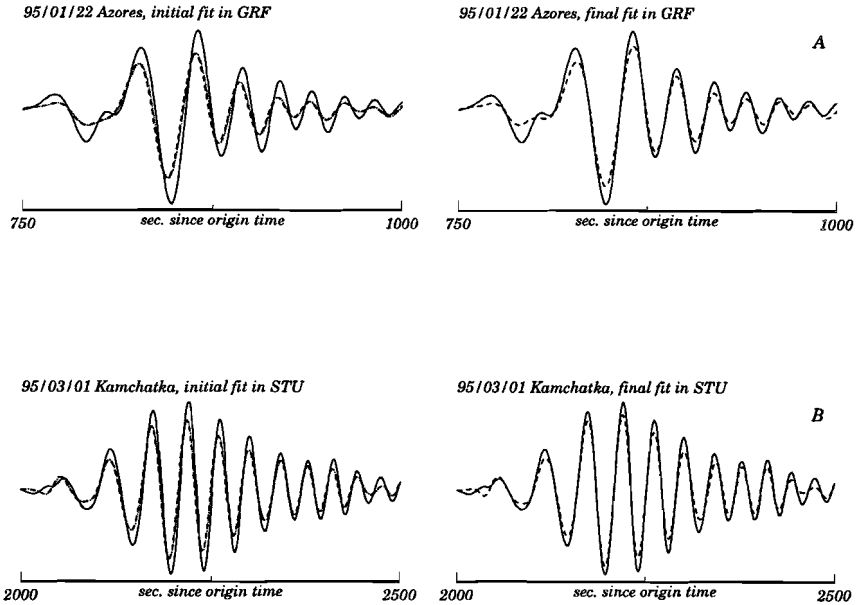


**Figure 4.6** Examples of the waveform fits. Dashed lines are synthetics, solid lines are recorded waveforms. All seismograms are band-pass filtered between  $T=20$  s and  $T=100$  s. The left panels show the initial fits according to the reference model (long-dashed lines) and the fits according to the one-dimensional model where the velocity at a certain depth is the mean of the final model at that depth (short-dashed lines). The right panels show the resulting fit (long-dashed lines) according to the final three-dimensional velocity model in Figure 4.5.

but this does not affect the model reconstruction very much, because it is the phase information that constrains the  $S$  velocity perturbation.

Figure 4.6 shows two examples of waveform fits obtained from the final three-dimensional model. These examples are representative of the quality that has been achieved. Figure 4.6a shows the fit in GRF for the Azores event of January 22, 1995 (path WLF-GRF). Figure 4.6b shows the fit in STU for the Kamchatka event of March 1, 1995 (path CLZ-STU). In all panels the solid lines are the recorded waveforms. In the left panels the long-dashed lines are the initial fits according to the initial one-dimensional reference model and the short-dashed lines are the fits according to the one-dimensional model where the velocity at a certain depth is the mean of the final model at that depth. It turned out that the deviations of

the mean layer perturbations of the final model from the reference model were of the order of 1%, whereas the lateral differences between the perturbations under two stations on a great circle are of the order of 4–5% (Figure 4.5). This means that the choice of the reference model does not severely influence the final velocity model, because the introduced nonlinearities are weak. The obtained data fits are mainly due to the lateral velocity perturbations rather than the mean (i.e., vertical) velocity perturbations of the layers. This is illustrated in Figure 4.6, from which it is obvious that only the final model gives a clearly improved fit to the waveforms (long-dashed lines in the right panels of Figure 4.6) and that the one-dimensional variations do not significantly improve the fit to the waveforms (short-dashed lines in the left panels of Figure 4.6).

When interpreting the velocity structure of the different layers (Figure 4.5), one should bear in mind that structures at the edges of the area covered by rays may be smeared out towards the unresolved region surrounding the resolved area. This may cause the anomalies to appear much larger in size than they actually are. This is a result of the regularization procedure, since the regularization tries to find the flattest model and therefore continues anomalies at the edges into unresolved areas. Examples of this can be seen in Figures 4.5c and 4.5d in the southwest corner of the model. The pronounced low-velocity structure turned out to be confined to the area just north of the French-German border when the smoothing weight  $\lambda$  in (4.1) was set to 0. This effect is also illustrated in Figure 4.7. A synthetic input model (Figure 4.7a) of alternating positive and negative anomalies on a scale comparable to the scale of the structures retrieved beneath Germany was sampled by the same 56 paths as used in the inversion of the real data. To the path-averages of the synthetic anomaly model, random noise was added with an rms value which was 40% of the rms value of these path-averages of the synthetic anomaly model. These data were then inverted applying the same smoothness constraints as in the inversion for Germany. The resulting model is shown in Figure 4.7b. The amplitudes of the anomalies in the input model are systematically underestimated, but there is relatively little smearing of anomalies. Only at the edges of the model some distortions occur due to the applied regularization.

## 4.4 Interpretation

As shown by the test in Figure 4.3a, the first two layers of the model (0–20 km in Figure 4.5a and 20–40 km in Figure 4.5b) contain the effects of variations in crustal thickness. Also, we realize that fundamental Rayleigh waves between periods of 20



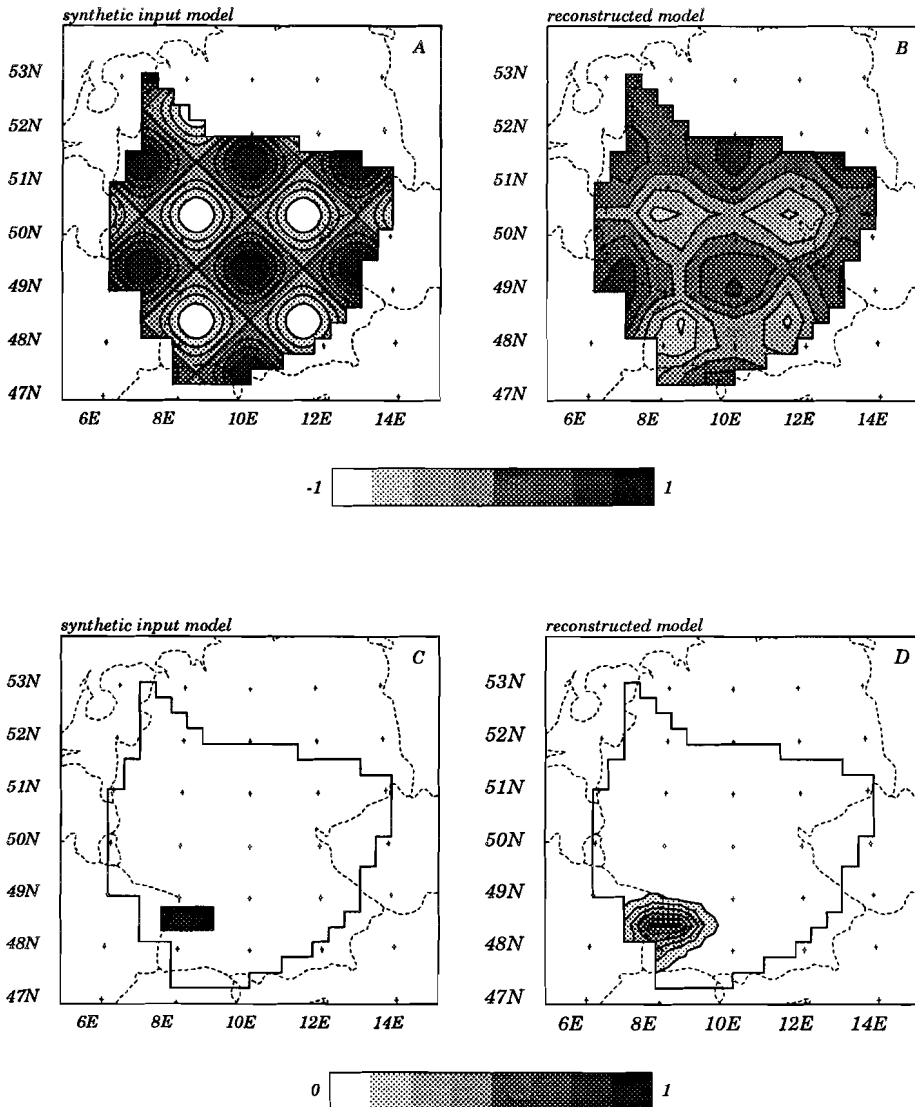


**Figure 4.7** Resolution tests. (a) Harmonic input model. (b) Reconstruction of harmonic model after inversion of the 56 data. (c) Synthetic block-shaped anomaly beneath the southern Rhine Graben. (d) Reconstruction of the synthetic anomaly beneath the southern Rhine Graben.

and 100 s are not the most convenient data to examine crustal structure. Reflection and refraction surveys provide better means to determine crustal structure. Nevertheless, the applied data set contains information on the first two layers. We will therefore occasionally consider the shallow *S* velocity structure as shown in Figures 4.5a and 4.5b.

#### 4.4.1 Eastern Part

A prominent feature in layers 3 and 4 (Figures 4.5c and 4.5d) is the high-velocity anomaly in the southeast. For the deeper layers ( $> 120$  km) this anomaly seems to vanish. To the northeast this high-velocity anomaly is bounded by a low-velocity structure, stretching almost parallel beneath the northeast striking part of the Czech-German border (Figure 4.5d). These low velocities seem to persist to larger depths, although somewhat broader than the expression between 80 and 120 km. The same transition from higher velocities in the south to lower velocities in the northeast has also been found in local *P* velocity studies beneath the Gräfenberg array by *Faber and Aichele* [1986] and by *Faber et al.* [1986]. The northeast striking boundary of the high-velocity anomaly seems to coincide with the boundary between two Hercynian units, the Moldanubian zone in the south and the Saxothuringian zone in the north [*Blundell et al.*, 1992; *Jacobshagen*, 1976]. Superimposed on the effects this boundary may have on seismic velocities, the relatively high velocities in the southeast are caused by an apparent thickening of the lithosphere from north to south. The increasing lithospheric thickness has been mapped by *Babuška and Plomerová* [1988], *Babuška et al.* [1984, 1987, 1990], *Plomerová and Babuška* [1988], and *Panza* [1985] and has been interpreted as being due to the formation of the lithospheric root of the Alps [*Blundell et al.*, 1992; *Panza and Mueller*, 1978]. Since the velocity in the lower lithosphere is greater than in the underlying asthenosphere, an increase in lithospheric thickness will result in a high-velocity region in the model. The low-velocity anomaly, most clearly visible in Figure 4.5d, northeast of this high-velocity anomaly lies in the northern part of the Bohemian Massif and is related to the Eger rift (Figure 4.1). The Eger rift is older than the European Cenozoic rift system, ECRIS, in its original definition (a continuous system of rift structures that traverses the lithosphere of central and western Europe extending from the Mediterranean to the North Sea over a distance of about 1100 km [*Prodehl et al.*, 1992], but is viewed as part of the ECRIS by *Ziegler* [1992]. The area of the Eger rift coincides with eastnortheast striking zones of Cenozoic volcanism [*Huckenholz and Kunzmann*, 1993; *Wilson and Downes*, 1992] and is characterized by an increase in heat flow [*Čermák et al.*, 1992]. The surface expression of this important

structure is the Eger Graben (parallel to the northern branch of the Czech-German border, Figure 4.1). We interpret the observed low-velocity anomaly in this area as the expression of the deep-reaching rift structure of the Eger Graben, indicating the presence of relatively hot material as could be expected from upwelling mantle material. Our results (Figures 4.5d–f) suggest that the geometry of the deeper structure related to the Eger Graben changes with depth. With increasing depth, we observe a broadening and a rotation from a northeast trending feature to a more north trending feature. These are indications that the visible graben is only a limited surface feature and that the entire rift system with its anomalous crustal and mantle structure is actually larger and does not necessarily follow its surface expression. *Wilson and Downes* [1991, 1992] suggested that the isotopic and trace element characteristics of volcanic rocks from the Cenozoic rift system can be explained in terms of a combination of both lithospheric and asthenospheric source components. The magmas generated in the asthenosphere or at the base of the lithosphere as a consequence of decompression during lithospheric extension interact with the lithosphere when ascending towards the surface. The concept of creation of magma in the asthenosphere or at the base of the lithosphere beneath the Eger Graben corresponds to the observation in our model that the low-velocity anomaly strikes most clearly parallel to the Eger Graben in Figure 4.5d (80–120 km depth).

#### 4.4.2 Western Part

The western part of the investigated region is dominated by features such as the Rhine Graben and the Rhenish Massif (Figure 4.1). The Rhine Graben is the central and most thoroughly examined part of the ECRIS [e.g., *Illies and Fuchs*, 1974; *Illies and Mueller*, 1970; *Prodehl et al.*, 1992, 1995; *Rothé and Sauer*, 1967]. It extends for about 300 km northward from Basel to a triple junction near Frankfurt, which forms the northern tip of the Rhine Graben. At this triple junction the rift system splits up. To the north it follows the Hessen Depression and Leine Graben and seems then to disappear beneath the young sediments of the North German Plain (Figure 4.1). The other branch continues from the triple junction northwestward through the Rhenish Massif into the Lower Rhine Embayment (Figure 4.1) and can from there on be traced into the North Sea. Today the Rhine Graben south of the triple junction is rather inactive with respect to tectonic and volcanic activities [*Lippolt et al.*, 1974; *Bonjer et al.*, 1984] compared to the northwestern prolongation through the Rhenish Massif, which is experiencing active rifting due to the present stress regime [*Blundell et al.*, 1992; *Müller et al.*, 1992; *Prodehl et al.*, 1992, 1995; *Raikes and Bonjer*, 1983].

*Panza et al.* [1980] and *Panza* [1985] inferred from a regional dispersion analysis of Rayleigh waves that the lithosphere-asthenosphere boundary is domed up to about 50 km depth beneath the Rhine Graben, Rhenish Massif, and the Lower Rhine Embayment regions. This statement, however, is not supported by the interpretations of more recent large-scale *P* velocity studies [*Babuška and Plomerová*, 1988; *Babuška et al.*, 1990; *Spakman*, 1986] and by recent local *P* velocity investigations carried out in the southern Rhine Graben area [*Glahn and Granet*, 1992; *Glahn et al.*, 1993] whose results clearly reject the presence of a distinct upwarping of the lithosphere-asthenosphere boundary. The *P* velocity model of *Glahn and Granet* [1992] and *Glahn et al.* [1993] for the southern Rhine Graben area shows a lithosphere and upper mantle structure which is rather heterogeneous with depth as well as laterally. Their model shows an anomaly pattern oriented along the strike of the graben down to a depth of about 70 km. At this depth a change in the anomaly pattern occurs and a dominant high-velocity anomaly is observed striking westward and reaching down to a depth of at least 140 km. This anomaly was not fully understood by *Glahn and Granet* [1992] and *Glahn et al.* [1993]. They claim that the low-velocity regions they observe in the uppermost mantle between the Moho and 70 km depth can only be seen as local features and cannot be regarded as a general asthenospheric upwelling.

In contrast to the southern Rhine Graben area, where regions of decreased velocities cannot be traced over long distances as continuous graben-related features, there is farther northward the region beneath the northern Rhine Graben and the western Rhenish Massif (Figure 4.1) which clearly shows reduced velocities from 50 to at least 200 km depth according to *Raikes* [1980] and *Raikes and Bonjer* [1983]. The transition under the Rhine Graben from the southern part, with its velocity fluctuations that are not directly correlated to the graben geometry, to the northern part, with markedly decreased velocities, was monitored by *Granet* [1986]. The area of the northern Rhine Graben is also characterized by an increased heat flow [*Čermák et al.*, 1992]. The deep-reaching low-velocity anomaly beneath the Rhenish Massif is centered under the western Eifel and terminates to the east approximately at the river Rhine [*Prodehl et al.*, 1992; *Raikes and Bonjer*, 1983]. This lateral asymmetry was discussed by *Fuchs and Wedepohl* [1983] in terms of the occurrence of Cenozoic volcanism west of the Rhine only. In contrast to the southern Rhine Graben area, the low velocities and increased heat flow indicate a broad updoming of the lithosphere-asthenosphere boundary to some 50 km beneath this area according to the authors mentioned above. This is supported by *Panza et al.* [1980], who found the lithosphere-asthenosphere boundary at 50 km depth. Although *Babuška and Plomerová* [1988] and *Babuška et al.* [1990] find a much

larger depth of the lithosphere-asthenosphere boundary than *Panza et al.* [1980] for the southern Rhine Graben area, for the northern prolongation of the Rhine Graben and for the Rhenish Massif both views are in agreement with each other and both show a thinned lithosphere with a thickness of less than 60 km. A general asthenospheric upwelling can therefore be assumed in this area. Considering this in combination with the increasing seismic activity from the northern Rhine Graben area into the Lower Rhine Embayment leads to the conclusion that the center of active rifting processes has shifted away from the south toward the northwest.

In our model we clearly observe relatively high velocities at greater depths under the southern part of the Rhine Graben and the adjacent Black Forest. This so-called Kraichgau anomaly shows roughly an east-west orientation (Figures 4.5d, 4.5e, and 4.5f) similar to the deeper observations by *Glahn and Granet* [1992] and *Glahn et al.* [1993]. Therefore, our model also suggests the absence of a recent upwelling of hot asthenospheric material beneath the southern Rhine Graben. The high velocities can be attributed to the interference of the rift system with the Alpine lithospheric root in the south [*Blundell et al.*, 1992]. Figure 4.7d shows that the east-west orientation of a synthetic input anomaly (Figure 4.7c) is recovered after inversion where we have followed the same procedure as in Figures 4.7a and 4.7b. This test shows that the orientation is not an artifact of the inversion. For the crustal and upper mantle layers (Figures 4.5a and 4.5b) to depths of about 40 km we also observe slightly higher velocities, but with no clear east-west orientation. This, but also the apparent velocity decrease from the Moho down to about 80 km beneath the southern Rhine Graben, corresponds to the results of *Glahn and Granet* [1992] and *Glahn et al.* [1993]. Similar to their interpretation, we interpret the velocity decrease between the Moho and 80 km depth (Figure 4.5c) as a local feature instead of an indication of general asthenospheric upwelling, because deeper than 80 km under the southern Rhine Graben, high velocities are observed. In the northern Rhine Graben the high velocities gradually change into lower velocities (Figure 4.5). Also the southwestern part of the Rhenish Massif, containing the volcanic area of the Eifel (Figure 4.1), shows up as an area with relatively low velocities extending over a large depth range. The contrast with the northeastern part of the Rhenish Massif, a region characterized by the absence of volcanism and not showing the pronounced low velocities, is clearly present below 80 km depth. These observations coincide well with the idea of an updoming of the lithosphere-asthenosphere boundary and with the results of *Raikes* [1980] and *Raikes and Bonjer* [1983]. The area with the Tertiary volcanic field of Vogelsberg (Figure 4.1) belongs to the northern aborted arm of the rift system and has a rather anomalous structure underneath. The Vogelsberg does not show up as an unambiguous anomaly in the deeper parts of our

model (Figure 4.5). A reason for this may be that the dimensions of the Vogelsberg area approach the limits of our resolution. On the other hand, the absence of any clear signature at depth coincides well with the results of *Raikes and Bonjer* [1983], who found that the decreased velocity associated with this volcanic feature has to be confined to a relatively shallow depth of less than 60 km. The shallower part of our model (Figures 4.5a and 4.5b) shows a rather faint expression of reduced velocities beneath the Vogelsberg area, but we prefer to interpret this structure with care. Finally, we observe for all depth levels a low-velocity anomaly below and to the northeast of the Saarland region (Figure 4.1). Since the formation of a half-graben, the Saar-Nahe trough, and extension of the lithosphere by 35% already occurred in Permo-Carboniferous time [*Henk*, 1993], it is hard to give a solid explanation for the observed lower velocities related to this frozen-in rift. Nevertheless, the measured increase in heat flow in this area [*Čermák et al.*, 1992] might be an indicator for higher temperatures at larger depths and therefore also reduced *S* velocities.

## 4.5 Conclusions

We have inverted fundamental mode Rayleigh waveforms (in the frequency band between 20 and 100 s) from 27 worldwide events recorded at 17 broadband stations in central and southern Germany to obtain a three-dimensional *S* velocity distribution beneath this area. We did not include possible effects of azimuthal anisotropy in our analysis. It is not likely that this will cause serious errors, since *Stange and Friederich* [1993] concluded that azimuthal anisotropy was not necessarily required to explain their surface wave data in the same region.

One of the prominent features of the model is the presence of low velocities below the northern branch of the Czech-German border, which is probably an expression of the rift structure beneath the Eger Graben. Also observed is a region of high velocities between 40 and 120 km depth beneath northern Bavaria, indicating an increase of lithospheric thickness towards the south close to the transition between two Hercynian units. Below the southern Rhine Graben, which at present is an inactive area with respect to rifting, high velocities are found. This coincides with the hypothesis that no hot mantle material is upwelling here now. These high velocities can be seen as a result of the interference of the rift system with the deeper Alpine structure. In contrast to the southern branch, under the northern branch of the Central European rift system, which is presently experiencing rifting, low velocities are more clearly visible. The structure below the volcanic Eifel, as well as the part of the Rhenish Massif west of the river Rhine, exhibit low velocities extending to

great depths. These observations could be explained by a broad (approximately 200 km wide) updoming of the lithosphere-asthenosphere boundary.

Most of the significant features in our model, which are limited by the degree of resolution of the actual anomalies, are interpreted in the previous section. They indicate that there is a strong correlation between upper mantle *S*-wave structure and the tectonic expressions at the surface. This conclusion is supported by the fact that variations in crustal thickness only slightly modify the anomalies found at greater depth, either because these variations appear to be minor for the major part of our model [Gutscher, 1995; Meissner *et al.*, 1987; Zeis *et al.*, 1990] or because the influence of variations in crustal thickness is restricted to the upper layers (down to 40 km depth (Figure 4.3a)). Additionally, the experiment of Figure 4.3b indicates that the reconstructed pattern of anomalies is not a result of mapping shallow structure to larger depths in the inversion. The connection between upper mantle structure and surface expressions is important, because it may provide a key to combining geologically and seismologically gained information into geodynamic conclusions.

# Chapter 5

## A possible interpretation of high shear-wave velocities beneath Bavaria, southern Germany

**Abstract** We suggest a possible explanation for a high shear-wave velocity anomaly observed under Bavaria. The closure of the Piemont ocean in the Cretaceous is a process which is related to the development of the Alps and the northern foreland. We propose that during the closure of this ocean, the young oceanic Adriatic plate subducted horizontally in a northward direction under central Europe (lithospheric doubling). At a certain stage, which is not tightly constrained by our scenario, the subduction polarity reversed to the present-day southward subduction of the European plate. We propose that the detached part of the Adriatic plate was left behind under central Europe. The young age of this part of oceanic lithosphere prevented it from sinking to larger depths. The observed high-velocity anomaly would be caused by the remnant oceanic lithosphere. In this chapter, we investigate the first order implications of the proposed scenario in terms of thermal, compositional and gravity effects. We show that temperature effects solely can not explain the observed seismic velocities, because the temperature contrasts are almost eliminated due to the long cooling history. It is, therefore, more likely that compositional effects, possibly in combination with small thermal effects, can explain the high velocities. It is also shown that the gravitational implications of the lithospheric doubling scenario are consistent with large-scale Bouguer anomaly observations.

---

<sup>1</sup>The work described in this chapter was done in collaboration with Rob Govers.



## 5.1 Introduction

An  $S$  velocity model of central and southern Germany down to depths of 200 km was recently presented by *Passier and Snieder* [1996] (Chapter 4). In this model, low-velocity areas were found under the Eger Graben, the northern Rhine graben, and the western Rhenish Massif including the Eifel region. See Figure 4.1 for the geographic locations of these structures. The low velocities suggest the upwelling of relatively hot mantle material under these regions. In contrast, the southern Rhine Graben area is characterized by relatively high velocities and no indications are found for active upwelling of mantle material in this area. Another dominant feature in the model is a high-velocity anomaly under northern Bavaria, which is the topic of this study. In this area, the  $S$  velocity is up to 7% higher than average. Most of the features of the model correlate well down to a depth of 200 km with geological and tectonic surface expressions. The Bavarian high-velocity region, however, seems to extend from a depth of 40 km only down to a depth of approximately 120 km, without any such surface expression. The part of the velocity model showing the Bavarian anomaly is displayed in Figure 5.1. Also shown in Figure 5.1 are the outlines of the most important geographic and tectonic units (c.f. Figure 4.1). It is important to note that at the southeastern edge of the model, along the strike of the Molasse basin, the suggested decrease of the high-velocity anomaly may be misleading, since there is little or no resolution in this area due to the absence of wave paths [*Passier and Snieder*, 1996]. The model contains no information on the possible continuation of the anomaly in a southeastward direction.

From a seismological point of view, the lithosphere is defined as the high-velocity lid on top of the asthenosphere, which is characterized by lower velocities. In this context, it has been suggested that the anomaly beneath northern Bavaria is the result of an increase of lithospheric thickness from north to south, which has been interpreted as the Alpine lithospheric root [*Blundell et al.*, 1992; *Panza and Mueller*, 1978]. In addition, it has been suggested that the transition between two Hercynian units, the Saxothuringian block and the Moldanubian block, contributes to the velocity increase from north to south (Figures 4.1 and 5.1). This explanation was primarily based on local  $P$  velocity studies [*Faber et al.*, 1986] and seismological studies of lithospheric thickness in central Europe [e.g., *Babuška et al.*, 1990]. There are, however, two questions that arise concerning this explanation. In the first place, interpreting higher velocities as being thickened lithosphere only because the lithosphere is defined by increased velocities can lead to a circular argument. Following this argument implies that an increase in lithospheric thickness would be the only possible explanation for high seismic velocities, but there might well be

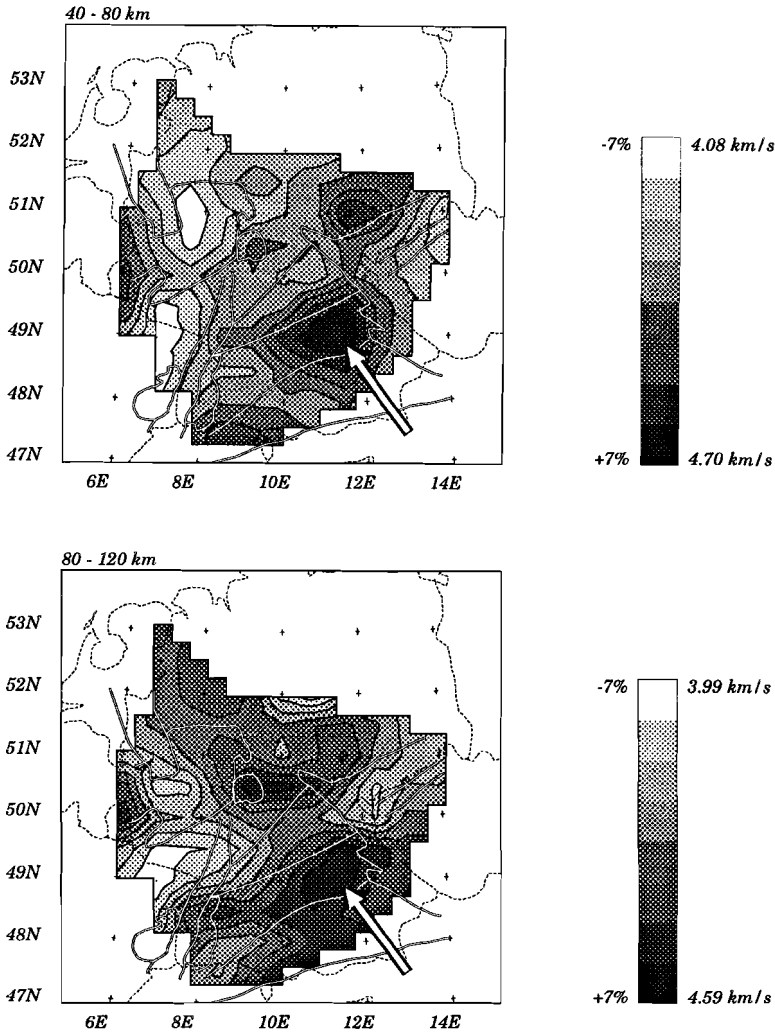


**Figure 5.1** Two layers (40–80 km and 80–120 km) of the shear velocity model of central and southern Germany. The range of the perturbations (relative to the layer mean) is plotted to the left side of the legends and the range of absolute *S* velocities is plotted to the right side of the legends. The depth interval of the layers is given in frame titles. The pronounced high-velocity anomaly under Bavaria is indicated by the arrow. At larger depths this anomaly disappears [Passier and Snieder, 1996]. Also indicated are the main geographic and tectonic units (see also Figure 4.1).

other structures giving rise to increased velocities under the 'unperturbed' lithosphere. In the second place, suppose that the increased velocities are an expression of a thickened lithosphere, then the explanation of the higher  $S$  velocity is shifted to the question what is the cause of the lithospheric thickening. An Alpine lithospheric root is not the only possible explanation. Seismological studies of lithospheric thickness in central Europe suggest an increase in the lithospheric thickness from about 80 km to about 130 km from north to south under the Moldanubian zone [e.g., *Babuška et al.*, 1990]. Under the Molasse basin, the thickness is approximately constant and under the Alps, it thickens even further to about 200 km. Crustal thickness, however, is approximately constant at 28 km under the Saxothuringian region and the Moldanubian region [*Zeis et al.*, 1990]. Under the Molasse basin, the depth of the Moho increases from north to south with a few kilometers, mainly caused by a corresponding thickening of the sedimentary cover [*Giese*, 1976] (see also next section). Under the Alps crustal thickness increases rapidly from north to south to reach depths of 50 to 60 km. Because, in the Moldanubian area, lithospheric thickening is not accompanied by any crustal thickening, it is unlikely that compressional geodynamic processes have led to a thickened lithosphere. In the remainder of this chapter we will suggest a possible scenario and investigate its implications that could explain the high velocities under Bavaria and that is different from the interpretation that the Bavarian anomaly is an expression of the Alpine root. Although not directly related to the actual deep Alpine structure, the Bavarian anomaly will be explained as the result of subduction of the African plate under central Europe. This subduction process is related to the Alpine orogeny and therefore a short outline of the Alpine history will now be given.

## 5.2 Alpine history

In this section we shall give a brief overview of the different stages and processes that have led to the present state of the Alpine orogen and its northern foreland. This overview consists of points of view that are commonly accepted as well as topics that are subject to debate.

One of the reasons for the observed large-scale complexity of the Alpine orogen is that many passive margins of small ocean basins have been created and subsequently destroyed. Spreading in the Alpine area started about the late Middle Jurassic (165–160 Ma) [*Trümpy*, 1982]. This rifting phase was particularly active during the separation of Gondwana and Laurasia and the associated opening of the Tethys and Atlantic ocean. In the Alpine realm a basin of true oceanic nature developed.

The original width of this ocean, called the Piemont ocean, is difficult to assess and estimates of the width range from 100 to 500 km [Blundell *et al.*, 1992]. This so-called Piemont ocean was bordered by the European plate in the north and northwest and by the Adriatic microplate in the south and southeast. The Adriatic plate formed the northern part of the African plate. From Middle Cretaceous (105–100 Ma) onward, closure of the basin started as the European and the Adriatic microplate began to converge [Dercourt *et al.*, 1986; Dewey *et al.*, 1989]. Because the oceanic lithospheric slab of the Piemont ocean was young and short, classical ‘Benioff’ subduction can be ruled out in the Alpine area [Vlaar and Wortel, 1976]. This might be the reason for the absence of volcanism associated with the Alpine Cretaceous subduction process. Generally, the subduction is assumed to have taken place in a southward direction [Kissling, 1993], meaning that the European plate subducted beneath the Adriatic microplate. However, up to now, the question how to characterize the subduction process accompanying the closure of the oceanic basin is still not resolved unambiguously and is open to debate. We will address this issue later again, but first the more recent Alpine history is further discussed in order to be able to propose an explanation for the Bavarian anomaly later in the chapter.

A second phase of convergence occurred during the Tertiary (50 Ma onward, [Dewey *et al.*, 1989]). With the ongoing convergence of Europe and Africa (together with its Adriatic promontory), the Alpine orogen developed during the collision process. From the Late Eocene to the Late Miocene (40–10 Ma) the Molasse foredeep evolved north of the Alps [Bachmann *et al.*, 1987; Ziegler, 1987, 1990] (Figure 4.1). Subsidence of the Molasse basin was controlled by tectonic loading of the lithosphere by the advancing Alpine nappes [Giese, 1976; Richter, 1951], combined with sedimentary loading. The river Danube marks the northern edge of the basin and runs approximately parallel to the Alpine front at a distance of about 100 km. Here the sediments reach a thickness of a few hundred meters. Sediment thickness increases to approximately 5 km near the Alpine thrust front [Geologische Karte von Bayern, 1981].

An important parameter in geodynamic studies are vertical motions of the free surface, because this quantity does not only contain information about current stress regimes, but also about deep mass distributions. At present, surface uplift rates of 1–2 mm per year are reported for the Alps and rates of a few tenths of a mm per year are reported for the Alpine foreland [e.g., Homewood *et al.*, 1986; Lemcke, 1974; Mueller, 1989; Pfiffner, 1986]. Lyon-Caen and Molnar [1989] suggest that the Alps and the adjacent foreland are currently not in regional isostatic equilibrium. They suggest that a recent (15 Ma or less) detachment of subducted lithosphere

beneath Italy could have led to a mass deficit. This could in turn have resulted in the present-day uplift and deviations from local isostatic equilibrium. On the other hand, *Mueller* [1989] attributes uplift of the Alps and foreland basin to isostatic rebound of less dense crustal masses which previously had been forced to greater depths. Although there exist different opinions about the underlying mechanism causing the present uplift, a model of the deep Alpine structure should predict the observed surface uplift rates.

In summary, the prolonged convergence of Europe and Africa has led to a mountain range of large geological complexity. This has resulted in an extremely excessive number of publications concerning studies of near-surface, deeper crustal and lithospheric structure beneath the Alps. Although a lot of work has been done and is still being done, *Kissling* [1993] points out that numerous major questions about the interior structure of the Alps are still left unanswered, and that suggested scenarios often have to be rated as speculative.

One of the major uncertainties is the nature of subduction beneath the Alps. Basically, there are two views on the problem of Alpine subduction. The ideas for the first view were already expressed by *Ampferer* [1906]. He postulated a series of subcrustal currents, which dragged crustal material nearly vertically beneath the growing Alpine orogen. This process was subsequently referred to as subfluence, or in German 'Verschluckung'. The subfluence hypothesis was picked up again by *Kraus* [1931] who proposed a 'double orogen' with lithospheric material moving into the mantle from the north as well as from the south (i.e. both directions perpendicular to the strike of the orogen). More recently, the subfluence model is imagined as two lithospheric slabs, one from the north and one from the south, which have both been pushed nearly vertically into the upper mantle during the collision process. [*Laubscher*, 1985; *Mueller and Panza*, 1986]. The second, more generally accepted view on Alpine subduction, envisions the Alps as a result of one-sided, southward subduction of the European plate beneath the Adriatic plate. In this case underthrusting takes place in a southward direction [e.g., *Kissling*, 1993; *Pfiffner et al.*, 1990; *Valasek et al.*, 1991]. According to this scenario, the latest stage of the collision is marked by northward indentation of a rigid wedge. The wedge of Adriatic crust is forced into the subducting European crust and splits it apart [*Holliger and Kissling*, 1992; *Meissner and Tanner*, 1993]. This wedging-subduction process appears to be responsible for a significant amount of shortening and thickening of the crust under the Alps.

### 5.3 Suggested alternative scenario

To explain the higher  $S$  velocities as observed beneath Bavaria (described in the introduction of this chapter), we suggest here an adjustment of the southward subduction scenario of the previous section. The proposed model is based on the principle of lithospheric doubling. Lithospheric doubling is defined by *Vlaar* [1982, 1983] as quasi-horizontal subduction of young ( $< 30$  Ma) oceanic lithosphere under continental lithosphere. The young subducting oceanic lithosphere is buoyant and the spreading ridge may also subduct. Although young oceanic lithosphere is less dense than the overriding continental lithosphere, the strength of the continental plate forces the oceanic plate to remain in position below the denser material. This results in a gravitationally unstable upper mantle, but this situation may ‘freeze’ in [*Nolet et al.*, 1986b]. *Vlaar and Cloetingh* [1984] show that lithospheric doubling provides a plausible scenario for the Alpine orogeny, although their view is not widely supported. *Dost* [1990] used the lithospheric doubling hypothesis to explain a high-velocity and high-density layer at approximately 100 km depth under the west European platform, which was interpreted as an eclogite layer. In other areas, such as the western United States, models suggesting (sub)horizontally subducting slab are more frequently assumed [e.g., *Atwater*, 1989; *Bird*, 1984; *Lipman et al.*, 1971].

To explain the Bavarian high-velocity anomaly, we also suggest lithospheric doubling, but not on a scale as large as inferred by [*Vlaar and Cloetingh*, 1984]. We propose that when subduction of the Piemont oceanic lithosphere started, this subduction was initially directed northward, the slab therefore underthrusting central Europe. Since this oceanic lithosphere was young [*Blundell et al.*, 1992] and therefore buoyant, subduction can be assumed to have taken place horizontally causing lithospheric doubling under the European plate. In order not to come into conflict with the ‘Verschluckung’ models or models based on southward subduction (see previous section) that are generally used to explain Alpine structures, the polarity of subduction needs to have switched after lithospheric doubling had taken place. With ‘polarity switch’ we mean that the role of overriding and underthrusting plate are reversed. It is important to note that it takes only a relatively short period to create a doubled lithospheric system with significant dimensions. If a convergence velocity of 4 cm per year is assumed, 5 Ma suffices to insert the oceanic lithosphere over a distance of 200 km under Europe. This shows that it is very well possible to propose a stage of lithospheric doubling beneath central Europe prior to a polarity switch of the subduction. Reversal of the polarity of subduction implies that the subducted oceanic lithosphere must have detached from the Adriatic plate. Sub-

sequently, subduction of the European plate commenced in a southward direction. The detached segment of oceanic lithosphere was left behind under central Europe. We do not want to speculate here on the precise mechanism causing such a reversal process. This would involve a detailed study of a more complete geodynamic scenario, which is at this point beyond our intentions. Nevertheless, a reversal of subduction polarity is feasible according to *Tao and O'Connell* [1992] if the upper lithosphere is considered as brittle and the lower lithosphere as viscous. A reversal of subduction polarity has already been proposed for other areas than the Alps [*Carney and MacFarlane*, 1982; *Hamilton*, 1979; *Karig and Mammerickx*, 1972; *Lewis and Hayes*, 1980; *Willett and Beaumont*, 1994]. In our proposed scenario, the actual duration of the doubling process and the timing of the polarity reversal are not tightly constrained. If doubling has been going on for a long time before the subduction polarity reversed, a large amount of oceanic slab material must have been subducted beneath central Europe. With progressive subduction, the northernmost part of the subducted lithosphere might have become separated from the continental lithosphere on top, leaving only the area immediately north of the Alps in a doubled state. On the other hand, if the polarity reversed a short time after lithospheric doubling initiated, oceanic lithosphere will only be present just north of the Alps and will be absent further northward.

In short, the scenario outlined above predicts from north to south (1) an unperturbed and undoubled continental lithosphere/upper mantle system (European plate), (2) a doubled lithosphere/upper mantle system (European plate on top of Adriatic plate), (3) the Alps on top of a still speculative slab configuration, and (4) the unperturbed Adriatic plate. We suggest that the part of oceanic lithosphere, which was left behind under central Europe after subduction commenced in a southward direction, is now causing the observed high-velocity anomaly under Bavaria. Further to the north, a possible continuation of the subducted oceanic lithosphere might have been separated from the continental lithosphere on top and might have sunk to greater depths, which makes it invisible in our *S* velocity model. We will now investigate some of the implications of this lithospheric doubling scenario. First, we will make a first order assessment of the nature of the velocity anomaly as would be produced by the presence of oceanic lithosphere beneath continental Europe. In doing so, temperature as well as compositional effects will be considered. Second, the gravitational signature of a horizontally subducted piece of oceanic lithosphere is compared with the observations.

### 5.3.1 Temperature

In this section we determine what the effect is of the presence of old oceanic lithosphere under central Europe on the temperature distribution. *Vlaar* [1983] already examined some one-dimensional thermal and magmatic consequences of lithospheric doubling. Here we will address the two-dimensional problem in order to estimate also the horizontal extent of the area thermally affected by the presence of the oceanic slab. In order to do so, we considered the two-dimensional thermal diffusion equation,

$$\frac{dT}{dt} = \frac{k}{\rho c_p} \left( \frac{\partial^2 T}{\partial x^2} + \frac{\partial^2 T}{\partial z^2} \right),$$

with  $k$  the conductivity,  $\rho$  the density, and  $c_p$  the specific heat. The diffusion equation has been solved numerically, using the 'method of lines' finite difference scheme [*Berezin and Zhidkov*, 1965; *Gear*, 1971], for a lithosphere/upper mantle configuration representing a partially doubled lithosphere. Because only thermal effects around 100 km depth are considered, we neglected radiogenic crustal heat production. Including heat production would only lead to somewhat higher temperatures at depth. Since we are looking for negative temperature differences relative to the unperturbed continental mantle geotherm, our study will therefore yield an upper limit of the thermal effect to be expected from the doubling process.

In the thermal model, we assume lithospheric doubling to take place instantaneously, thereby avoiding any complications due to transient dynamic processes, such as temperature changes during the active doubling stage. This is allowed, because the actual time needed to create the doubled system (about 5 Ma, see previous section) is small compared to the thermal time constant of the system [*Vlaar*, 1983]. We consider a continental system, which is instantaneously doubled at 80 km depth by an oceanic lithosphere/upper mantle system. We choose this depth, because it is a representative thickness of the unperturbed continental lithosphere in the neighboring areas [*Babuška et al.*, 1990]. The initial continental geotherm above the subducting oceanic plate is a steady state geotherm with a linear temperature distribution between 0°C at the surface and 700°C at 80 km depth. The original geotherm of the oceanic lithosphere is derived from the cooling half-space approximation [*Carslaw and Jaeger*, 1959; *Turcotte and Schubert*, 1982], which gives a depth dependence of the temperature according to an error-function. For the underlying mantle (continental and oceanic) temperatures are calculated using an adiabatic temperature rise with depth (0.6°C/km) [*Turcotte and Oxburgh*, 1969; *Verhoogen*, 1951]. The oceanic geotherm is computed for a lithospheric age of 25 Ma. The temperature at the top of the model is kept fixed at 0°C. At both vertical edges



of the model we apply a zero horizontal heat flow boundary condition, because no influences from outside our modeling area are assumed. Through the bottom of the model, at a depth of 400 km, the adiabatic temperature gradient is applied, assuming unperturbed mantle conditions at that depth. Figure 5.2 shows the temperature distributions of the doubled system at five stages of the cooling process. The model covers a horizontal distance of 800 km. The initial temperature distribution is determined by the oceanic slab subducted instantaneously and horizontally under the continental lithosphere in a northward direction over a length of 400 km. The final panel shows the temperature distribution 100 Ma after doubling took place. In the light of our proposed scenario, this could be interpreted as the maximum amount of time elapsed since doubling took place. The general trend that can be observed from Figure 5.2 is that thermal contrasts due to the presence of the subducted oceanic slab gradually decrease with increasing cooling history. After 100 Ma there are hardly any observable lateral temperature contrasts left. The thermal behavior has also been visualized in Figure 5.3, which shows the vertical temperature profiles through the doubled lithosphere/upper mantle system at 0, 2, 10, 30, and 100 Ma after doubling and the initial continental geotherm for comparison. The strong temperature contrast resulting from the insertion of oceanic lithosphere under 80 km of continental lithosphere ultimately leads to an overall cooling of the system. Apart from a laterally poorly pronounced thermal anomaly after 100 Ma, it can also be concluded that temperature differences with respect to an unperturbed continental mantle geotherm, at 80 km depth and 30 Ma or longer after doubling, can amount up to 200 or 300°C at most.

In order to translate this temperature difference to an  $S$  velocity perturbation, the derivative of the velocity with respect to the temperature,  $\partial\beta/\partial T$ , has to be computed. This derivative is given by

$$\frac{1}{\beta} \frac{\partial\beta}{\partial T} = \frac{1}{2} \left( \frac{1}{\mu} \frac{\partial\mu}{\partial T} + \alpha \right) ,$$

with  $\mu$  the shear modulus and  $\alpha = -(1/\rho)(\partial\rho/\partial T)$  the volume expansion coefficient. *De Jonge* [1995] has compiled the different values for the different parameters from the literature and he concludes that a temperature which is 100°C lower than a reference temperature yields an increase in  $S$  velocity between 0.2 and 0.8% of the reference velocity. If the temperature dependence of the  $S$  velocity is computed for the depth interval which is of interest here (about 80 km depth), using the values of *Anderson* [1988, 1989], it is found that a temperature decrease of 100°C with respect to a reference temperature will result in a relative  $S$  velocity increase of 0.5%. For our model, a value of 0.5%/100°C would imply a velocity anomaly in the order of

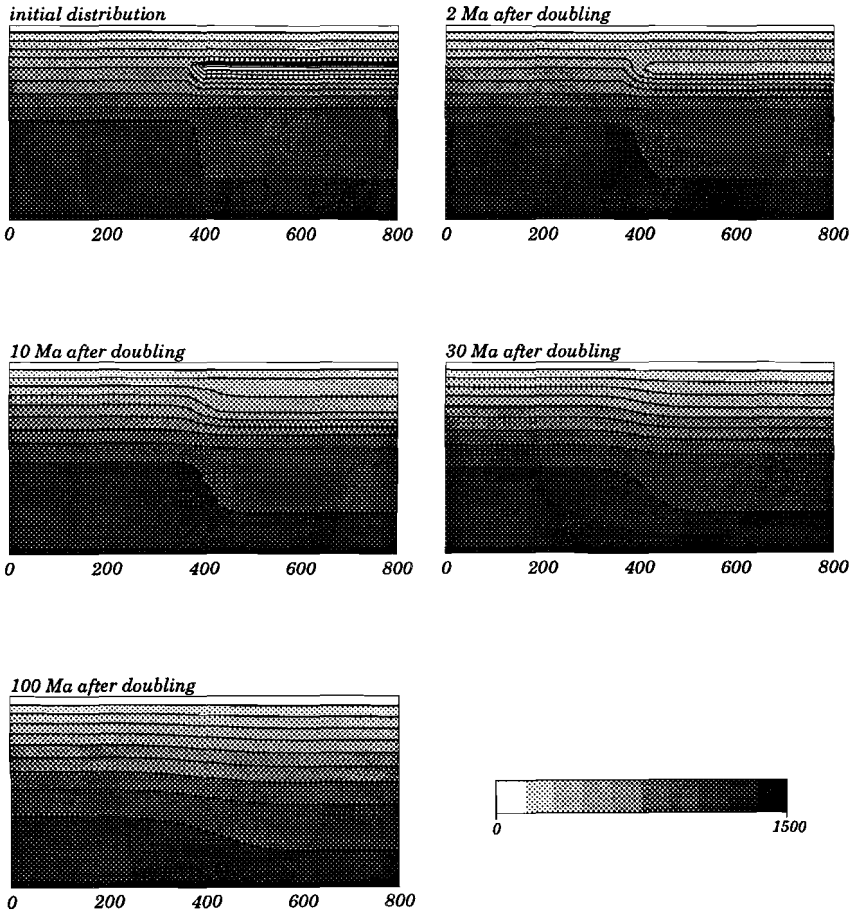


**Figure 5.2** Temperature distribution at five stages of the diffusive cooling process. From light to dark the grey shades indicate temperatures from 0°C to 1500°C. In the context of an oceanic slab subducting horizontally beneath central Europe, the left sides of the panels indicate north and the right sides indicate south. The model ranges down to a depth of 400 km and covers 800 km laterally.

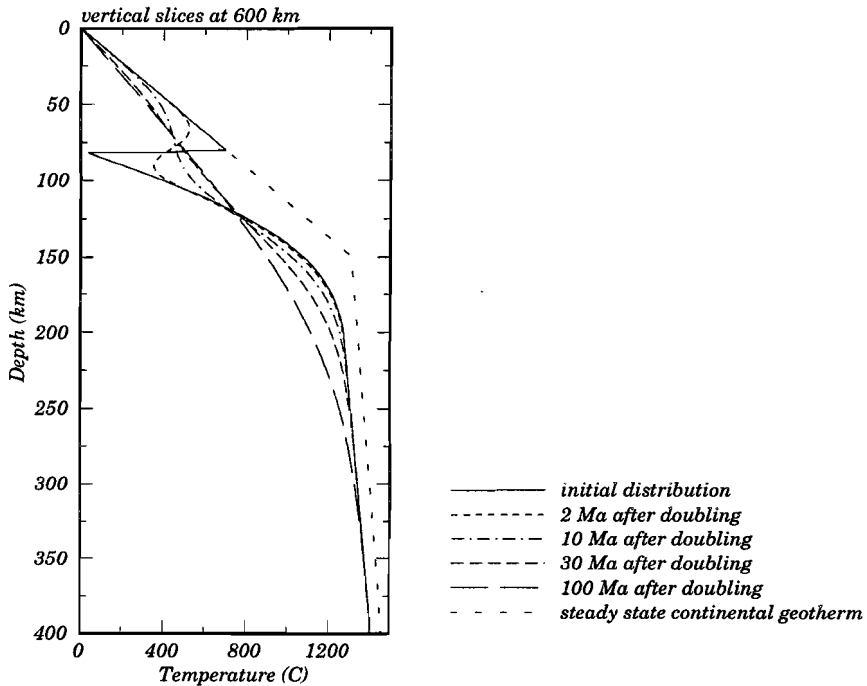


**Figure 5.3** Vertical temperature profiles through the model in Figure 5.2 for the horizontal position at 600 km. Also shown is the unperturbed continental geotherm.

1–1.5% if measured relative to the unperturbed continental mantle geotherm. In spite of the fact that the applied thermal model undoubtedly is a simplification of the true three-dimensional thermal distribution, we can conclude from this first order assessment, that temperature alone can never be the sole cause of the observed velocity anomaly (up to 7%). Furthermore, it is observed that the anomaly in the velocity model (Figure 5.1) seems to be much more localized than is predicted by the thermal model (Figure 5.2). Thermal effects may explain a small part the velocity anomaly, but to explain the major part other factors, such as composition, have to be considered. Especially for  $S$  velocity the composition may play an important role, since  $S$  velocity depends stronger on composition than  $P$  velocity does. In the next section we will estimate what the compositional effects would be on  $S$  velocity for the proposed lithospheric doubling mechanism.

It is important to note that the precise timing of the start of the building of the Alps is not of crucial importance with respect to the role played by the temperature in explaining the observed high-velocity anomaly under Bavaria. From Figures 5.2 and 5.3 it is clear that regardless whether doubling would have taken place for example 30 Ma or 100 Ma ago, the conclusion would still hold that thermal effects can only explain a rather small part of the observed anomaly and that other causes have to be sought, for instance composition, to explain the major part of the anomaly.

### 5.3.2 Composition

We will now try to estimate the effects on the  $S$  velocity anomaly of a horizontally subducted oceanic lithosphere beneath an 80 km thick continental lithospheric plate. An oceanic crust/upper mantle system consists of a basaltic crust underlain by a peridotite called harzburgite. Harzburgite is the crystalline residue left after partial melting has produced basalt. The major mineralogical components of harzburgite are olivine, about 70%, and orthopyroxene, about 20% [e.g., *Helfrich et al.*, 1989]. Beneath the harzburgite the undifferentiated parent mantle rock, pyrolite, can only be inferred, since actual samples of pyrolite do not exist. The basaltic crust will transform to eclogite at shallow depth during subduction [*Ringwood*, 1975]. *Gubbins and Snieder* [1991] and *Van der Hilst and Snieder* [1996] use the eclogite layer to model the dispersion of and precursors to  $P$ -waves. Due to the transformation from basalt to eclogite, the continental lithosphere will after doubling be underlain by an eclogite layer followed by harzburgite.

We are interested in the  $S$  velocity differences, resulting from compositional effects, between an oceanic lithosphere/upper mantle system and a reference system below a depth of 80 km. The perturbations in each layer of the velocity model (Figure 5.1) are given relative to the mean of each layer. For the layer between 40 and 80 km this is 4.40 km/s and for the layer between 80 and 120 km this is 4.32 km/s. The  $S$  velocities of mantle materials, eclogite and harzburgite in this case, can be determined from laboratory experiments with actual samples found in ophiolite sections. The problem is that the uncertainties in the velocities due to extrapolation of the data obtained at the laboratory to ambient mantle conditions may be large. Following the literature [e.g., *Anderson*, 1989; *Boyd and Meyer*, 1979; *Christensen*, 1984; *Christensen and Smewing*, 1981; *Manghnani and Ramanantoandro*, 1974; *Ringwood*, 1975; *Salisbury and Christensen*, 1978; *Sumino and Anderson*, 1984] we have taken 4.7–4.9 km/s and 4.6–4.9 km/s as possible ranges of values for the  $S$  velocities of eclogite and harzburgite, respectively. Both compositions appear to

be fast relative to the reference velocities. In both cases this is not surprising, since eclogite consists of garnet (about 50%) and clinopyroxene (about 50%) [e.g., *Helffrich et al.*, 1989], which are both known to have relatively high velocities. The relatively high velocity of harzburgite could also be expected because of the fact that cratonic roots show up as fast areas in tomographic models [*VanDecar et al.*, 1995]. These old cratonic roots mainly consist of harzburgite [*Boyd et al.*, 1993; *Menzies et al.*, 1993], which must be an important source of the anomaly, because thermal effects can be ruled out considering the age of the cratonic roots. The employed velocities for eclogite and harzburgite correspond to perturbations in the order of 8% relative to the reference values. Given the fact that it is unlikely that the layering of the subducted oceanic lithosphere coincides with the depth parameterization of the velocity model (layers from 40–80 km and 80–120 km), the velocity perturbations as caused by the subducted lithosphere will be spread out over these two layers. It must be emphasized that due to the uncertainties concerning the depth and thicknesses of the eclogite and harzburgite layers and the exact values of the  $S$  velocity we are only able to give a first order estimate of the velocity perturbation that would result from a doubled lithospheric system. This estimate, however, is of the same order of magnitude as the observed anomaly. Therefore, we can conclude that implications of the lithospheric doubling scenario are consistent with observations of the velocity anomaly.

### 5.3.3 Gravity

In the previous section we pointed out that the observed high velocities could be explained by the presence of oceanic lithosphere under central Europe. We will now test whether this hypothesis is also consistent with observed gravity anomalies. Figure 5.4 shows the observed Bouguer anomaly in the area of the seismic model. The anomaly pattern is shown between spherical harmonic degrees 26 and 200. This means that small-scale crustal heterogeneities have been removed. The remaining anomaly can be interpreted as a result of large-scale structures in the lithosphere or upper mantle. Under the Molasse basin, the gravity anomaly decreases towards the Alps in the south. This is most likely due to the increasing thickness of the sedimentary cover and the corresponding changes in Moho depth towards the Alps [*Lyon-Caen and Molnar*, 1989]. From northwest to southeast across the Moldanubian area, however, there are no significant changes in Moho depth or any other lateral crustal structures that may cause the observed gradient of the Bouguer anomaly. In the area of interest, the contrast in terms of gravitational characteristics between the crustal structure of the Saxothuringian zone and

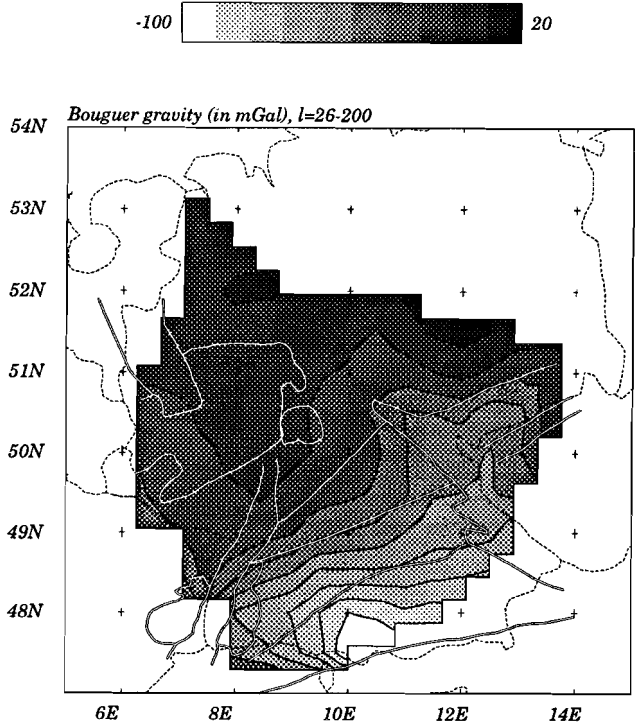


**Figure 5.4** Bouguer gravity filtered between harmonic degrees 26 and 200. This corresponds to scale-lengths of 750 and 100 km.

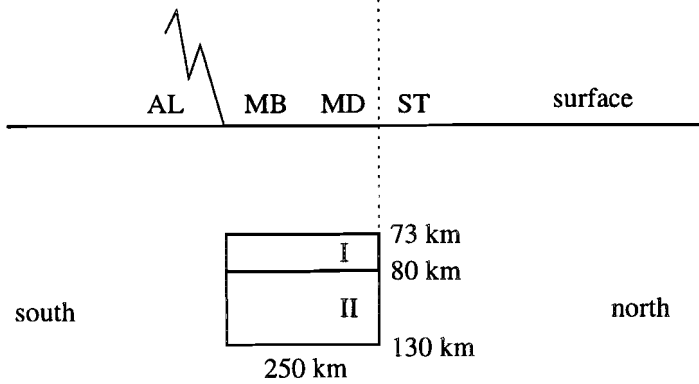
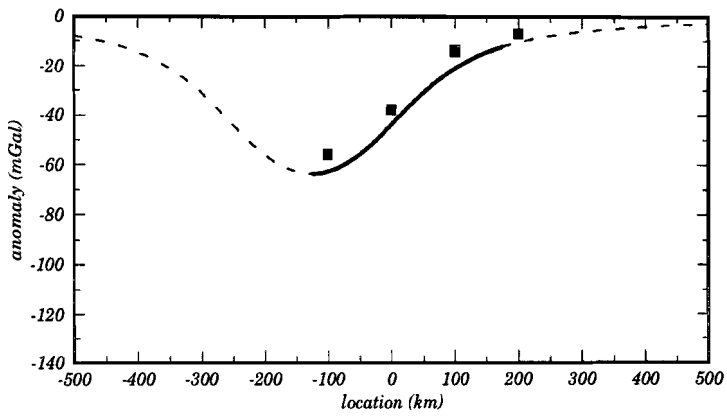
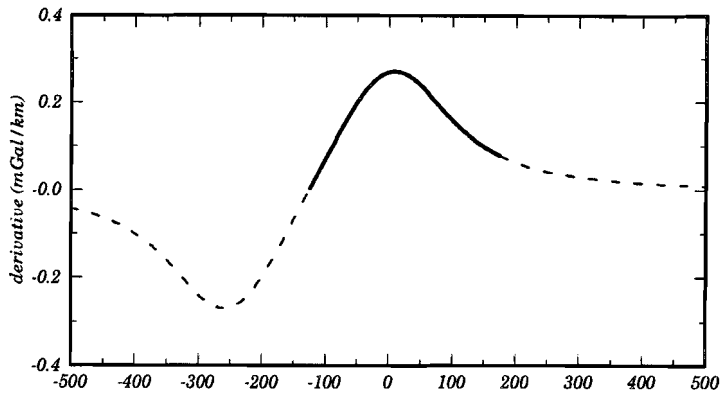
the Moldanubian zone is much less pronounced than further to the west [Plauermann, 1987, 1988]. The decreasing sharpness of the crustal contrast between the two zones from west to east is also clearly present in magnetic anomaly observations [Wonik et al., 1992]. Consequently, a sharp transition between the Saxothuringian and the Moldanubian block at crustal level, showing up as a gradient in a filtered image such as Figure 5.4, can be ruled out as the cause of the observed gradient in the gravity anomaly. For the above reasons, the observed gradient of the anomaly in the investigated area has to be explained by anomalous structure at lithospheric depth. The gradient of the Bouguer anomaly lies between 0.2 and 0.3 mGal/km. The absolute value of the anomaly, between  $-20$  and  $-60$  mGal, might be partly due to upper crustal effects. Although in the western part of the Moldanubian zone, the Rhine Graben, and the Black Forest, the crustal contributions to the observed

Bouguer anomaly are quite well constrained [Edel and Fluck, 1989; Gutscher, 1995], the crustal contribution in the eastern Moldanubian zone is less intensively examined. Since here the crustal and sub-crustal contributions to the observed gravity anomalies are not well determined, and since we are primarily interested in contributions of deeper upper mantle structure, we decided not to take the shallow structure into account in the gravity modeling. This is also the reason why we will mainly focus on the gradient of the gravity anomaly rather than on the absolute value.

In interpreting seismological models in terms of earth structure and composition we encounter a paradoxical situation. Seismic velocities, which can be determined with a reasonable resolution in the upper mantle, are difficult to extrapolate from a laboratory environment to mantle conditions. However, densities, for which laboratory extrapolations can be carried out with much more confidence, are difficult to determine in the earth. Because of this and because of the strong non-uniqueness of gravity modeling and because of the elementary character of this study, we choose not to model the absolute density distribution. Instead we test whether the gravitational observations could be explained by density perturbations which are realistic estimates when considered in the context of the scenario of lithospheric doubling.

The model we consider consists of an oceanic slab subducted northward over a distance of 250 km under central Europe. An eclogite crust with a thickness of 7 km was assumed over a harzburgite layer of 50 km. In the previous section it was noted that the oceanic components must be divided over two layers of the velocity model. In accordance with this, the eclogite layer is assumed to be just above 80 km and the harzburgite layer just below that depth (Figure 5.5). To explain the increasing negative Bouguer anomaly towards the south, the oceanic slab must have the effect of a 'light' body. This implies that the gravity effect of the denser eclogite has to be less than the effect of the harzburgite, which is less dense due to the fact that its denser components have left the material during differentiation.

**Figure 5.5** On the next page: bottom panel: synthetic model of block of horizontally subducted oceanic lithosphere (not to scale). Layer I is a 7 km thick eclogite layer ( $\Delta\rho = +0.15 \text{ g/cm}^3$ ) and layer II is a 50 km thick harzburgite layer ( $\Delta\rho = -0.07 \text{ g/cm}^3$ ). The depths of the layer interfaces are indicated to the right of the block and the two-letter codes, indicating the different tectonic regions, are explained in Figure 4.1. The corresponding Bouguer anomaly and the derivative of the Bouguer anomaly are shown in the upper two panels. Parts of the curves that are of interest are solid. The black squares are the observations (see text).





According to literature [e.g., *Anderson, 1989; Clark and Ringwood, 1964; Ringwood, 1975; Ringwood and Green, 1966*] the density of eclogite usually ranges from 3.50 to 3.55 g/cm<sup>3</sup>. The density of harzburgite ranges from 3.28 to 3.32 g/cm<sup>3</sup>. We take 3.37 g/cm<sup>3</sup> as an estimate of the density for an unperturbed mantle, because this is the density around 80 km depth according to the reference model. This results in representative density perturbations of approximately +0.15 and -0.07 g/cm<sup>3</sup> for eclogite and harzburgite, respectively. We model the gravitational effect of a cube-shaped lithospheric body extending from 73 to 130 km depth, measuring 250 km perpendicular to the strike of the Moldanubian area and measuring 250 km from the Bohemian Massif along the strike of the Moldanubian zone towards the southwest. At the surface, the gravity perturbation due to the density perturbations at depth is computed. A cross-section through the model, perpendicular to the strike of subducted oceanic slab, and its gravitational consequences are shown in Figure 5.5. The observed gravity at four points is indicated by the black squares in Figure 5.5. The black squares are determined as the averages along the northern boundaries of the Molasse basin, the Moldanubian zone, and the Saxothuringian zone, respectively. The most northern square is 100 km north of the Saxothuringian zone. In the modeling procedure, we have only considered the effects of the lithospheric block left beneath central Europe after a reversal of subduction polarity. The Alps are positioned immediately south of this block, but because we do not want to speculate on any deep Alpine structure, no structure is extrapolated under the Alps.

From Figure 5.5 it is clear that this simple two-layer model predicts a gravity anomaly with a gradient between 0.2 and 0.3 mGal/km over the northern edge of the slab. This coincides well with the observed gravity in the area where the northern edge of the slab is assumed to be (Figure 5.4). Also, the absolute level of the gravity anomaly is quite well approximated. Towards the south, the model of Figure 5.5 is of not much value, because the observed gravity anomaly will be strongly dominated by laterally heterogeneous structures related to the Molasse basin and the Alps in this area. The corresponding parts of the synthetic gravity profiles are therefore dashed in this region in Figure 5.5. On the northern edge of the subducted oceanic body there are no significant contributions to be expected from large-scale lateral crustal or upper mantle heterogeneities. In Figure 5.5 also the northernmost parts of the gravity profiles are dashed, since we do not aim to model gravity in this area. In spite of different sources of uncertainty, such as geometry and dimensions of the subducted slab and more reliable density information, it can be concluded that the proposed scenario of northward horizontal subduction during a relative short period prior to the main phase of the Alpine development is not in conflict with observations of the large-scale Bouguer anomaly.

## 5.4 Discussion

In this chapter, we propose an explanation for the observed high  $S$  velocity anomaly under Bavaria. This anomaly could be caused by a leftover from oceanic lithosphere subducted beneath central Europe during closure of the Piemont ocean, an early stage related to the Alpine history. In this scenario, the composition of the oceanic body, possibly in combination with small temperature effects (which are rather insensitive to the precise timing of the Alpine orogeny), can be seen as the direct cause of the observed velocity perturbation. It is also shown that the gravitational implications of the proposed scenario are comparable to the observations.

Although we bring up a possible explanation, the arguments given in favor of this scenario should by no means be interpreted as unambiguous evidence. They should only be seen as indicators which are consistent with some first order implications of the scenario. Of course, there are still problems left concerning this explanation. For example, the velocity anomaly is only observed in the eastern part of the Moldanubian zone, whereas the large-scale Bouguer anomaly pattern reveals a gradient in the entire Moldanubian zone. This means that in the light of our explanation, the oceanic slab seems to extend to the west according to the gravity observations. However, this does not become clear from the velocity model. A possible reason for this could be that towards the west the large-scale velocity anomaly related to the slab structure interferes with smaller-scale crustal structures, such as the Urach structure [Glahn *et al.*, 1992] or deeper lithospheric structure of the Schwarzwald and the southern Rhine Graben [Prodehl *et al.*, 1992]. These small-scale features could obscure the velocity signature of an oceanic slab. On the other hand, one could argue that the oceanic slab is only present under the eastern part of the Moldanubian block and that it terminates towards the west according to the  $S$  velocity model. The observed gravity gradient (Figure 5.4) in the west might then be the result of smearing of a sharp contrast between the Saxothuringian and Moldanubian zone due to the applied filtering.

In order to find evidence for the true structure in the northern Alpine foreland, and also for the actual structure under the Alps, more sophisticated geodynamic modeling studies using additional data have to be carried out in the future. Hopefully, these studies will clarify the mechanism responsible for the switch of the subduction polarity and yield more information about the geometry and the dimensions of subduction in the Alpine area. The probable deviations from local isostatic equilibrium [Lyon-Caen and Molnar, 1989] should pose important constraints on a more detailed modeling approach. It is interesting to note that the buoyant slab in our model predicts an uplift of approximately 1 km under local isostatic equilibrium

conditions. Since the topography in the Moldanubian area is only around 400 m, this implies that our model is also compatible with the results from *Lyon-Caen and Molnar* [1989].

For the compositional and gravitational modeling in this study, we assumed a horizontally layered oceanic lithosphere with a constant thickness and with vertical edges. This is probably a simplified view on the problem and the velocities and density perturbations have to be seen as averages of the oceanic structure. Nevertheless, in spite of the remaining questions and uncertainties concerning dimensions of the structure and velocity and density parameters, our study shows that first order effects on  $S$  velocity and on Bouguer gravity can well be explained by a paleo-subduction process. It would therefore be very useful to carry out further studies to quantify this scenario and to clarify and find evidence for the true upper mantle structure in the Alpine area and its foreland.

# Chapter 6

## Surface wave waveform inversions to test shear-wave velocities under eastern Australia

**Abstract** The waveform inversion method explained in Chapter 3 yields estimates of local structure and average velocity gradients. In this chapter, this technique is used to test specific features (and their amplitudes) of a three-dimensional tomographic model. As an example, we test features of a recent  $S$  velocity model of the Australian region by *Zielhuis and Van der Hilst* [1996]. We invert 20 Rayleigh wave waveforms between 20 and 110 s recorded on the Australian continent, most of them by the mobile SKIPPY network. From the data, we directly extract local measurements of the  $S$  velocity structure at various locations beneath Australia. These measurements do not suffer from several problems that occur in tomographic inversions of large datasets (e.g., spatial variations in resolution, different sampling of anisotropy). Consequently, our results are an independent test of the characteristics of the large-scale Australian model. Because we obtain local measurements that appear to be consistent with the large-scale three-dimensional  $S$  velocity model tested in this study, our results provide illustrative examples of how specific features of a complex velocity structure can be easily determined by applying the inversion technique of Chapter 3 to only a few waveforms.

---

<sup>1</sup>The work described in this chapter was done in collaboration with Rob van der Hilst. A modified version of this chapter has been submitted for publication in *Geophys. Res. Lett.*

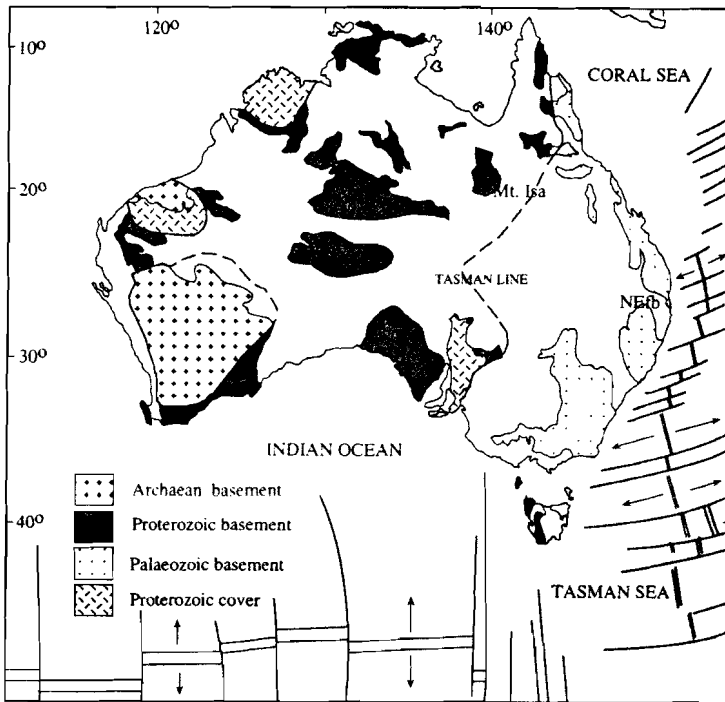


**Figure 6.1** Major geological subdivision of the Australian continent. The Tasman Line separates the Precambrian cratons in central Australia from Phanerozoic basement in eastern Australia. The location and nature of this boundary is controversial. NEfb is the New England fold belt. After Zielhuis and Van der Hilst [1996].

## 6.1 Introduction

From a tectonic point of view, the Australian continent can roughly be divided into three zones [Shaw *et al.*, 1995]. The most recent tectonic processes are found in the east (Figure 6.1) and are of Phanerozoic age (less than about 0.57 Ga), whereas the oldest processes took place in the west and are of Archaean age (more than 2.5 Ga). The central part of the continent consists of Proterozoic cratons (0.57–2.5 Ga). The boundary between these Proterozoic shields in central Australia and the younger regions in the Phanerozoic east is often referred to as the Tasman Line (TL). The assumed location of the TL is mainly based on studies of geological outcrops and of gravity and magnetic anomalies. One interpretation of the location is shown in

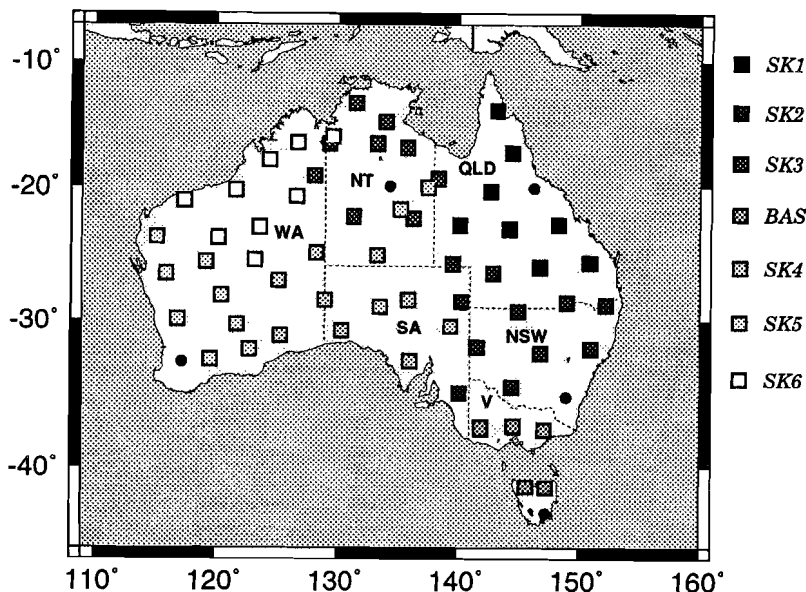


**Figure 6.2** Locations of the SKIPPY stations (squares) and permanent stations (circles). The grey shades indicate the period of deployment: darker arrays are deployed earlier than lighter arrays. Abbreviations on the map: WA, Western Australia; NT, Northern Territory; SA, South Australia; QLD, Queensland; NSW, New South Wales; V, Victoria.

Figure 6.1. The boundaries between the units are controversial, but can possibly be delineated by seismic imaging. The Australian continent is ideally situated for such seismological studies, since it is almost completely surrounded by a zone of high seismic activity. To exploit optimally the abundance of regional seismicity, the Research School of Earth Sciences of the Australian National University initiated in 1993 the SKIPPY project in order to study continent's interior [Van der Hilst *et al.*, 1994; Kennett and Van der Hilst, 1996]. The project embraces subsequent deployments of arrays, named SK1 thru SK6 and BAS. Each individual array consists of up to 12 broad-band instruments (Figure 6.2). Between May 1993 and the end of 1996, these individual subarrays, in combination with several permanent IRIS and GEOSCOPE stations, yield a very dense data coverage of the Australian continent.

*Zielhuis and Van der Hilst* [1996] used waveforms recorded by the permanent stations and the earliest SKIPPY employments in eastern Australia (SK1 and SK2). These stations are mainly located in Queensland, New South Wales, and Victoria (Figure 6.2). Using the Partitioned Waveform Inversion (PWI) technique [*Nolet*, 1990], they constructed a three-dimensional model of the  $S$  velocity distribution in the upper mantle and the transition zone beneath eastern Australia and the adjacent oceanic regions. This model will hereafter be referred to as ZH96. Work is in progress to include also data from later employments. As an example, Figure 6.3 shows layers at depths of 140 and 300 km of a model which is based on the dataset from which model ZH96 has been constructed, augmented by data from the employment of the stations in Northern Territory (SK3). These two layers show the characteristic features of the model, which extends down to a depth of 670 km. The best resolution is obtained for the regions beneath Northern Territory, eastern Australia, and the oceanic areas east of the continent.

In the construction of models such as ZH96, numerous crossing paths eventually have led to the final model. Characteristics of a large amount of data, rather than the behaviour of individual waveforms, outline the features of the  $S$  velocity distribution beneath the Australian continent and the adjacent oceanic areas. In procedures like PWI, effects such as trade-offs, spatial variations in resolution (different effects of path coverage), sampling of anisotropy, if any, are likely to influence the final result. Due to regularization, the amplitudes of the anomalies in the final model have to be interpreted with care. In this chapter, we will use the waveform inversion method explained in Chapter 3 to test independently several aspects of model ZH96. We will use only a small amount of waveforms to obtain local information about the  $S$  velocity structure at various locations beneath the Australian continent. By doing so, we extract local  $S$  velocity information directly from the data without suffering from the possibly disturbing effects that might be associated with the inversion of large datasets. This strategy will enable us to test, using an independent technique, several spatial features observed in the model obtained from PWI. Considering the examples of Chapter 3, the method also allows a test of the amplitude of these features. Specifically, in the upper 200 km we aim to test pronounced low velocities along the eastern continental margin and the latitudinal dependence of the nature of the transition from these low velocities to higher velocities in central Australia. According to model ZH96, in the southeastern part of the continent, this transition occurs over a broad zone rather than abruptly. However, further to the north, the contrast seems to be rather sharp. Deeper than 200 km, we will test the assumed presence of high velocities under the Mt. Isa block region (Figure 6.1) extending to the New England fold belt region. For a comprehensive discussion and interpretation

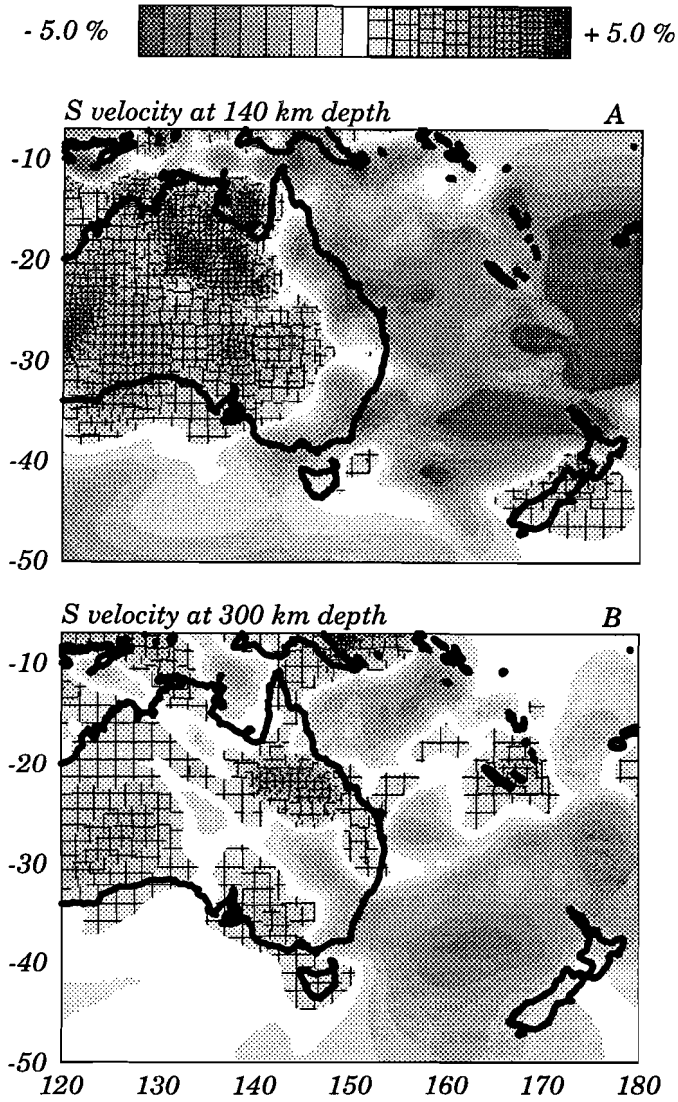


**Figure 6.3** *S* velocity distributions at depths of (a) 140 km and (b) 300 km obtained after inversion of the dataset of ZH96, augmented by data from the employment of the stations in Northern Territory (SK3). Reference velocities are 4.5 and 4.66 km/s, respectively.



Date	Time	Lat	Lon	Depth	$m_b/M_s$	Region
93/05/27	08:52:00	29.4 S	178.0 W	128	5.9/-	Kermadec
93/08/10	00:51:55	45.0 S	166.7 E	15	6.2/7.1	S. Island (NZ)
93/08/21	08:07:50	46.3 S	95.8 E	15	5.0/-	SE. Indian Rise
94/02/09	19:27:09	21.2 S	173.5 W	21	5.6/5.2	Tonga
94/06/18	03:25:20	42.9 S	171.5 E	15	6.2/7.2	S. Island (NZ)
94/12/25	11:43:54	30.4 S	177.8 W	37	5.1/-	Kermadec
95/04/16	13:23:48	10.1 S	159.4 E	23	5.6/5.7	Solomon Islands

Table 6.1 Events used

of model ZH96 we refer to *Zielhuis and Van der Hilst* [1996].

## 6.2 Method and data

We used the surface wave waveform inversion method presented in *Passier and Snieder* [1995b] and Chapter 3 to obtain relative  $S$  velocity perturbations as a function of depth between pairs of stations. Each individual pair of stations lies on a similar great circle that connects them to a source. Phase differences associated with the two fundamental mode Rayleigh wave waveforms were inverted for  $S$  velocity perturbations on the path between the stations. The stations and events that were used for this so-called case I are shown in Figure 6.4. In this study, the stations within one pair are typically separated by 300 to 400 km. Alternatively, surface wave waveforms recorded in two stations at approximately the same epicentral distance, but with a slightly different azimuth to the source, were inverted for the relative path-averaged horizontal  $S$  velocity gradient between the structures under the two paths. The stations and events used for this configuration, which is called case II, are shown in Figure 6.5. For case II, higher modes can be incorporated in the waveform inversion to enhance the depth resolution with respect to the inversions of only fundamental mode data. The characteristics of all stations and events that were used are listed in Tables 6.1 and 6.2.

We used vertical component displacement waveforms in the period range between 20 and 110 s. To be able to compare two waveforms in the case II inversions, we corrected for differences in epicentral distance. To correct for this difference in the case II inversions, the waveforms recorded at the stations at the smallest epicentral

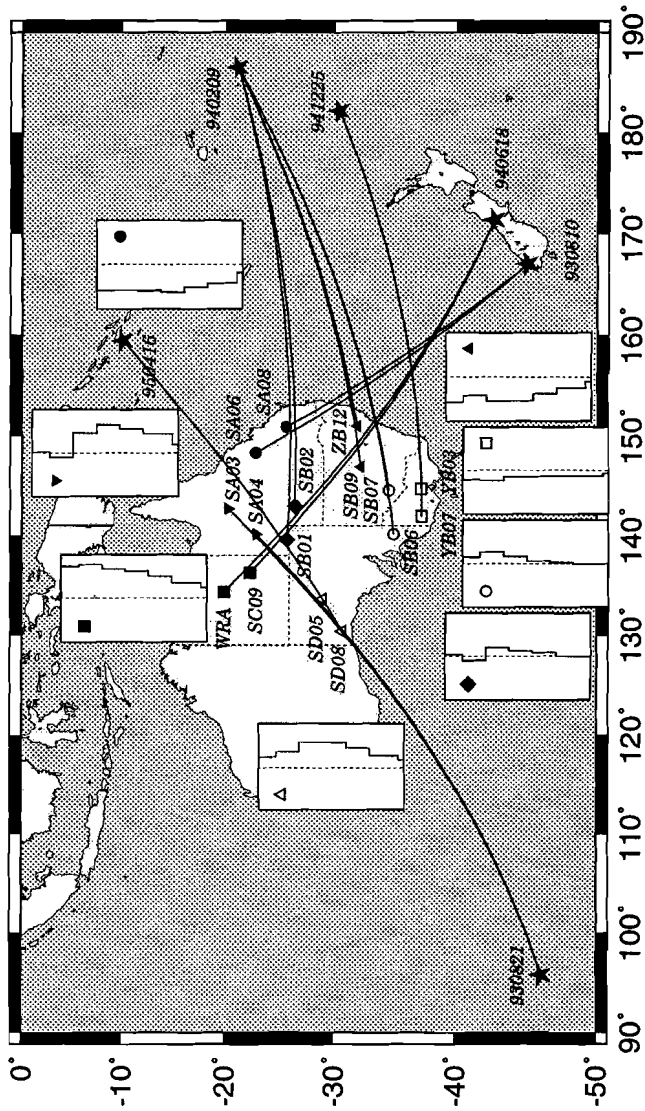


**Figure 6.4** Stations, events, great circle paths, and inversion results for the case I inversions. Symbols in the velocity panels correspond to station symbols for which the perturbations were obtained. In the velocity panels, perturbations range from -5% to 5% and depth ranges from 0 to 250 km.

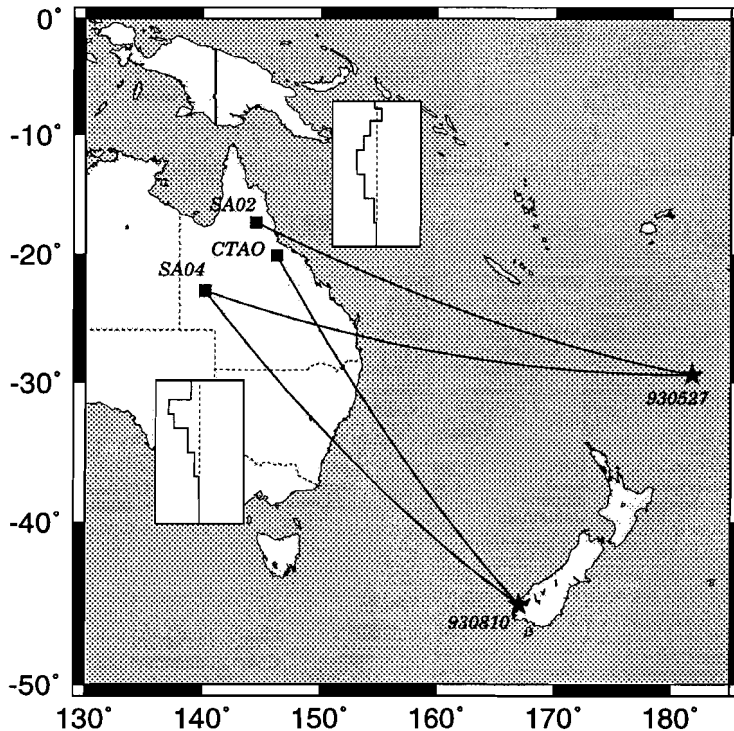


**Figure 6.5** Stations, events, great circle paths, and inversion results (in both cases: northern path minus southern path) for the case II inversions. In the velocity panels, perturbations range from  $-2\%$  to  $2\%$  and depth ranges from 0 to 600 km.

distance (SA02 and CTAO, respectively), were shifted forward to the epicentral distance of the accompanying station (SA04). This was achieved by adding a phase shift to each frequency component according to the reference model. Throughout this study, we used the same reference model as was used for model ZH96. It has a crustal thickness of 30 km and it is a slightly modified PREM model in the mantle [Zielhuis and Nolet, 1994].

In the following discussion of case I results, we use the terms initial fit and final fit. An initial fit is defined as the comparison between a waveform recorded in the second station (largest epicentral distance) and a synthetic waveform which is computed by propagating the waveform recorded in the first station (smallest

Station	Lon	Lat
SA02	144.49 E	17.36 S
SA03	142.67 E	20.34 S
SA04	140.14 E	22.94 S
SA06	148.31 E	22.90 S
SA08	150.89 E	25.71 S
SB01	139.59 E	25.79 S
SB02	142.89 E	26.51 S
SB06	140.15 E	35.04 S
SB07	144.51 E	34.66 S
SB09	146.86 E	32.29 S
ZB12	151.00 E	31.97 S
SC09	136.30 E	22.40 S
YB03	144.64 E	37.28 S
YB07	141.92 E	37.34 S
SD05	133.59 E	29.00 S
SD08	130.41 E	30.72 S
WRA	134.34 E	19.94 S
CTAO	146.25 E	20.09 S

**Table 6.2** *Stations used*

epicentral distance) to the second station according to the reference model. A final fit is defined as the comparison between, again, a waveform recorded in the second station and a synthetic waveform which is now computed by propagating the waveform recorded in the first station to the second station according to the model obtained from the inversion.

### 6.3 Results

We will discuss the results for the case I and case II inversions separately. In some inversions, regularization has been applied by adding the weighted depth integral of the squared velocity perturbations to the function to be minimized in the inversion. If applied, the weights given to the regularization term were small. This is why in most cases not only the sign of the velocity perturbation, but also its amplitude can

be interpreted.

### 6.3.1 Case I

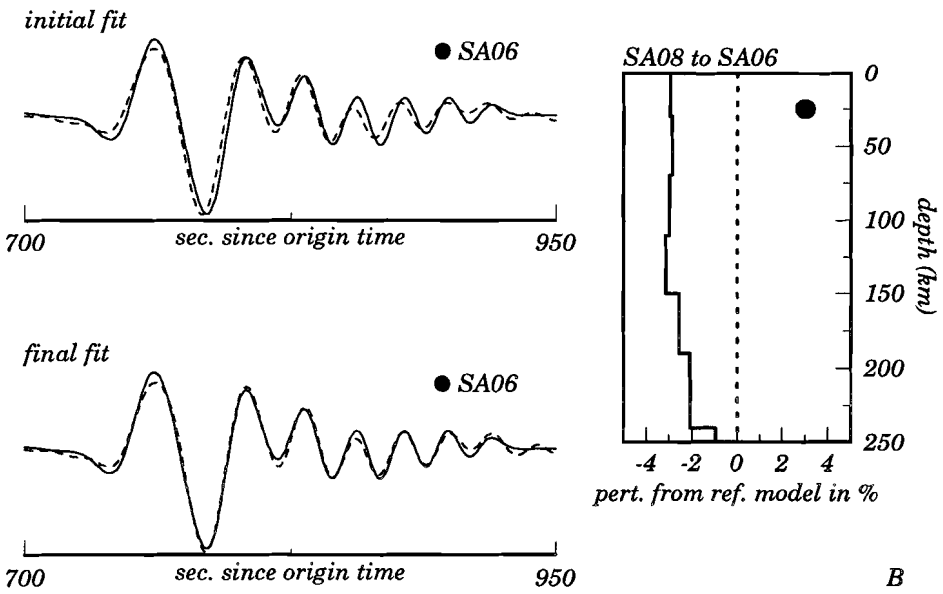
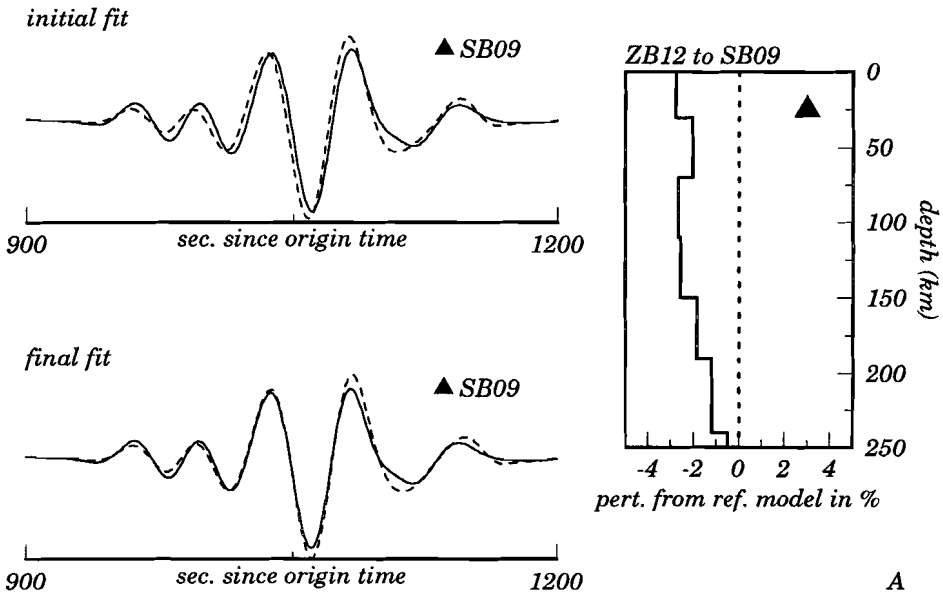
Figure 6.4 shows the locations of the case I experiments. Figures 6.6a–h show the data, the fits, and the obtained velocity perturbations between the two stations of each pair. The perturbations are relative to the reference model. The symbols in the upper corners correspond to the symbols that are used in Figure 6.4 for the station locations. The inversion results are also shown in Figure 6.4. In *Passier and Snieder* [1995b], the vertical resolving power of the technique is discussed and it is shown that the crustal contamination below the Moho is small.

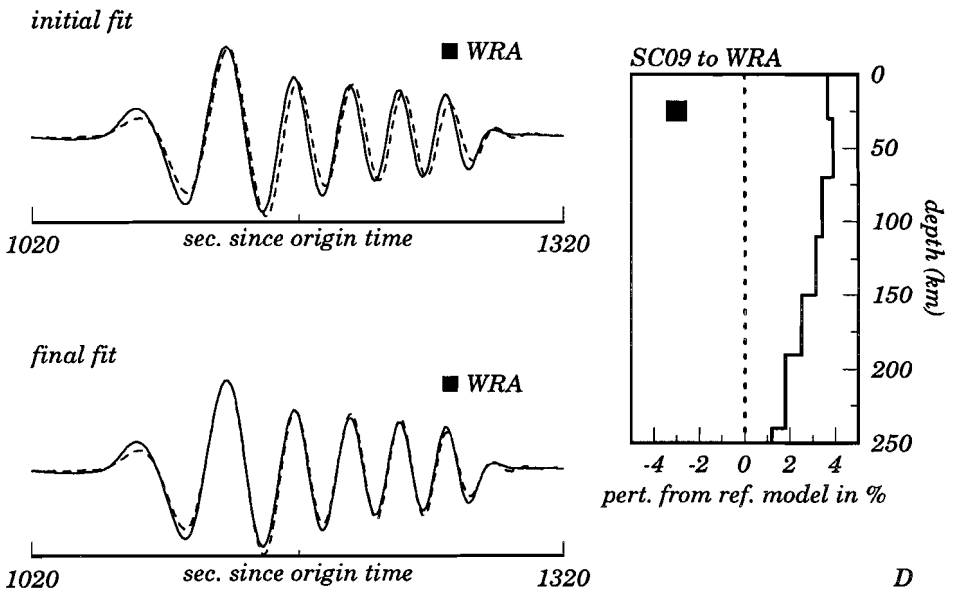
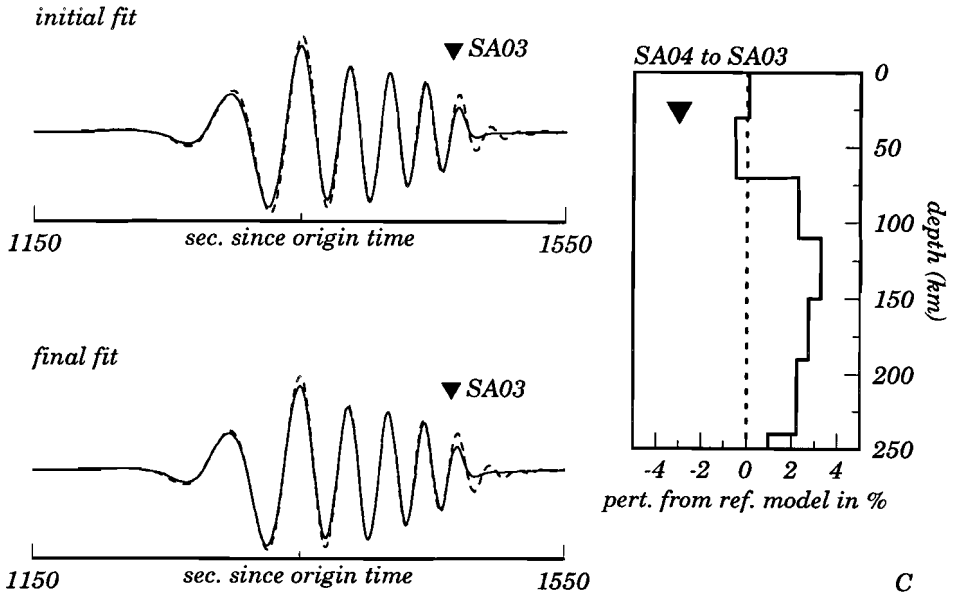
Our results along the easternmost edge of the continent (path SA08 to SA06, solid circle; path ZB12 to SB09, solid triangle) both reveal  $S$  velocities which are 2 to 3% lower than the reference model. These lower-than-average velocities persist from the surface down to a depth of at least 200 km (Figures 6.6a and 6.6b). The negative perturbations are also expressed by the initial fits. In these two examples, the datafit clearly improves after inversion.

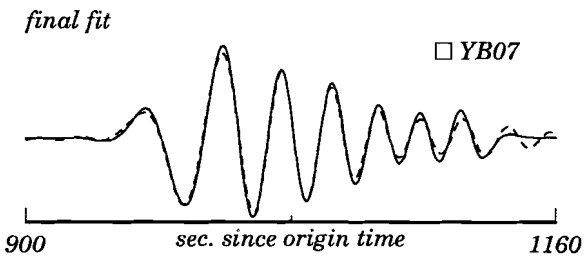
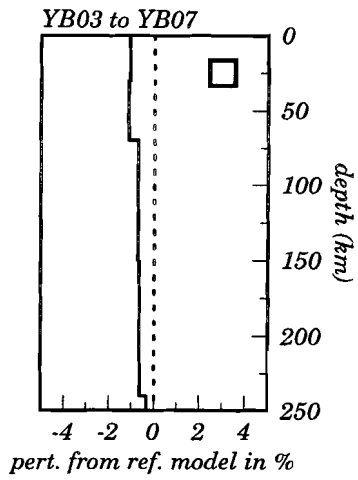
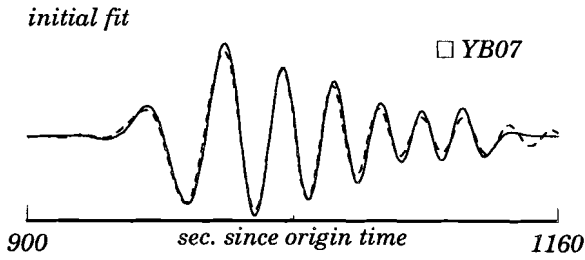
A dramatic change in the  $S$  velocity structure in north Australia can be observed if we move from the eastern continental margin westward to the central part of the continent (Figures 6.6c and 6.6d, path SA04 to SA03, solid inverted triangle; path SC09 to WRA, solid square). Both inversions yield  $S$  velocities which are 3 to 4% higher than the reference model down to a depth of at least 200 km. The structure between SA04 and SA03 seems to be only slightly perturbed down to 70 km depth. At first sight, the initial fit in SA03 (Figure 6.6c) seems to be good and may not indicate a significant velocity perturbation. However, closer examination of the waveforms revealed a substantial mismatch at the lowest frequencies. Therefore, only a significant perturbation is found at larger depths. The obtained final datafits are good. These results indicate a transition in north Australia from low upper mantle velocities in the east to high upper mantle velocities in the central part of the continent.

Further to the south, we do not observe such a sharp transition if we move from the eastern margin in a westward direction (Figures 6.6e, 6.6f, and 6.6g). Instead, the inversion results (path YB03 to YB07, open square; path SB07 to SB06, open circle; path SB02 to SB01, solid diamond) suggest a region with moderate  $S$  velocity

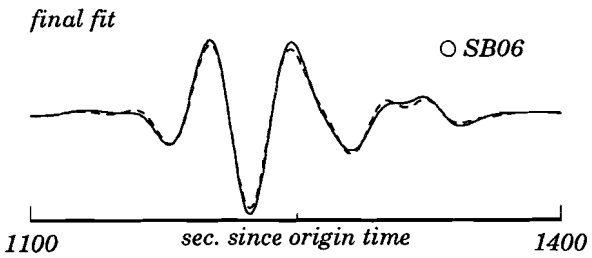
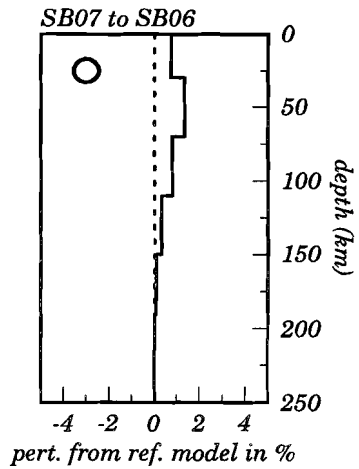
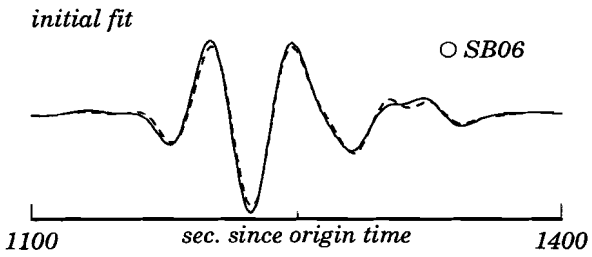
**Figure 6.6** On the next four pages: data (solid lines), results, and fits (dashed lines) for the case I inversions.





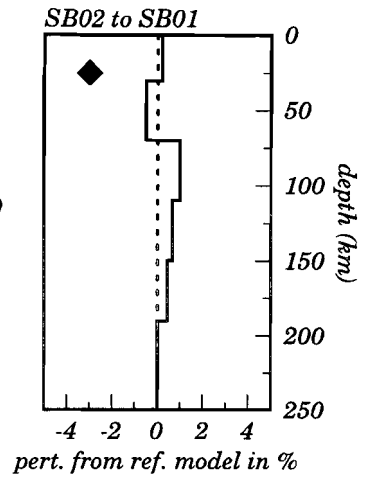
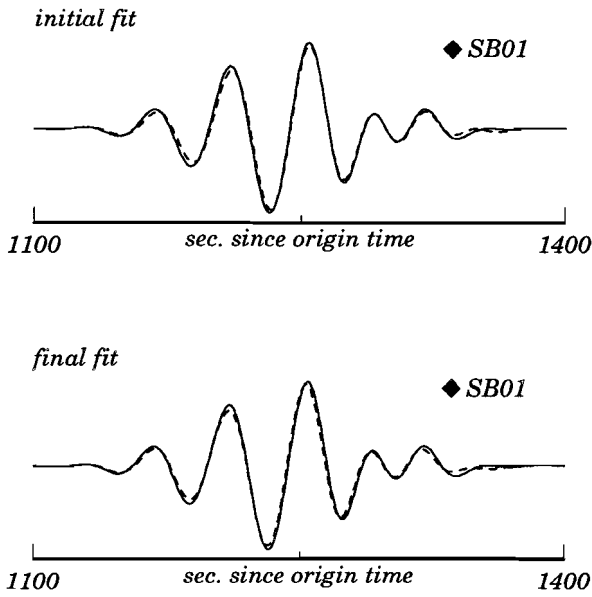


E

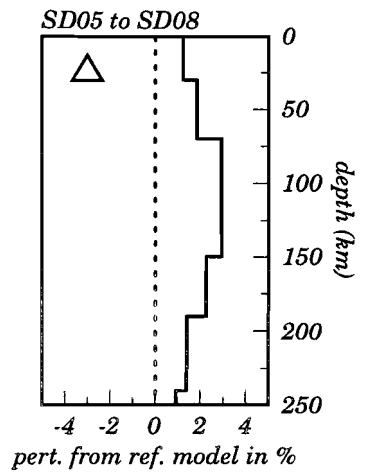
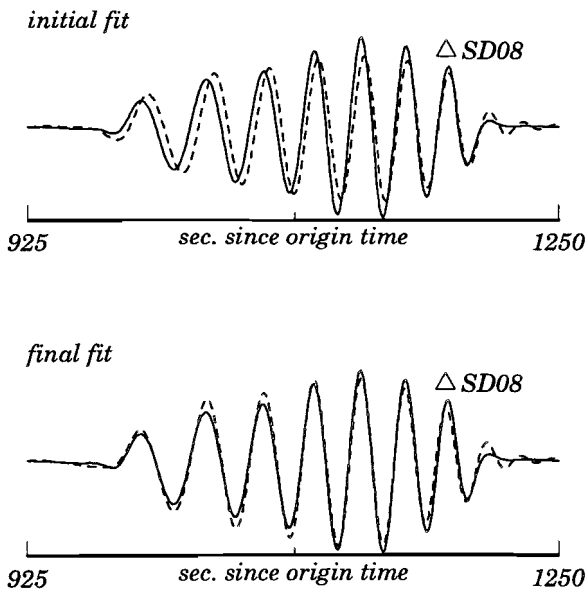


F





G



H

perturbations adjacent to the areas with pronounced low velocities in the east. The small velocity perturbations are already suggested by the initial fits: for all frequencies, the initial fits are close to the final fits. Moving further westward in the southern part of the continent, we find high velocities again (Figure 6.6h) for the path between SD05 and SD08 (open triangle). The perturbations are strongest between 70 and 150 km depth and the amplitude is about 2 to 3%. The final fit indicates that this perturbation fits the data well.

Our observations correspond well with the features in the model obtained by PWI. From the results of our tests, we can confirm the most important statements made by *Zielhuis and Van der Hilst* [1996] about the *S* velocity structure under Australia. These are (1) pronounced low velocities along the Phanerozoic eastern edge of the continent, (2) in the north, a rapid transition to higher velocities in the area with Proterozoic shields in central Australia, and (3) more to the south, a gradual transition to the higher velocities in the Proterozoic regions. At a depth of 80 km, our experiments as well as PWI reveal a lateral contrast of about 6% across the transition from east to west.

### 6.3.2 Case II

Figure 6.5 shows the setting of the case II experiments. The data, corrected for differences in epicentral distance, are shown in Figures 6.7b and 6.7f. In the data, a clear difference in the behaviour of the fundamental modes between the two events is observed. Figure 6.7b shows that the fundamental mode energy of the 930527 event arrives about at the same time in SA02 and SA04. The fundamental mode energy released by the 930810 event, however, clearly arrives earlier at SA04 than at CTAO (Figure 6.7f). In both cases, the higher modes arrive earlier at SA04 than at SA02 and CTAO, respectively. Based on a comparison between synthetic seismograms for the studied events with different numbers of modes and the observed data, it was decided that the main portion of energy for the 930527 event is carried by the fundamental mode and the first two higher modes. The 930810 event is best represented by the fundamental mode and only the first higher mode. Figures 6.7a and 6.7e show the path-averaged velocity contrasts relative to the reference model as they are obtained by inversion. The perturbations are also shown in Figure 6.5. Synthetic tests in *Passier and Snieder* [1995b] demonstrate that for the employed frequencies the solution is reliable at least down to 400 km depth. Both inversions reveal higher velocities under the path to SA04 than under the paths to SA02 and CTAO, respectively. Inversion of the data of the 930527 event shows that the largest contrast between the paths to SA02 and SA04 is located between depths of 150 and

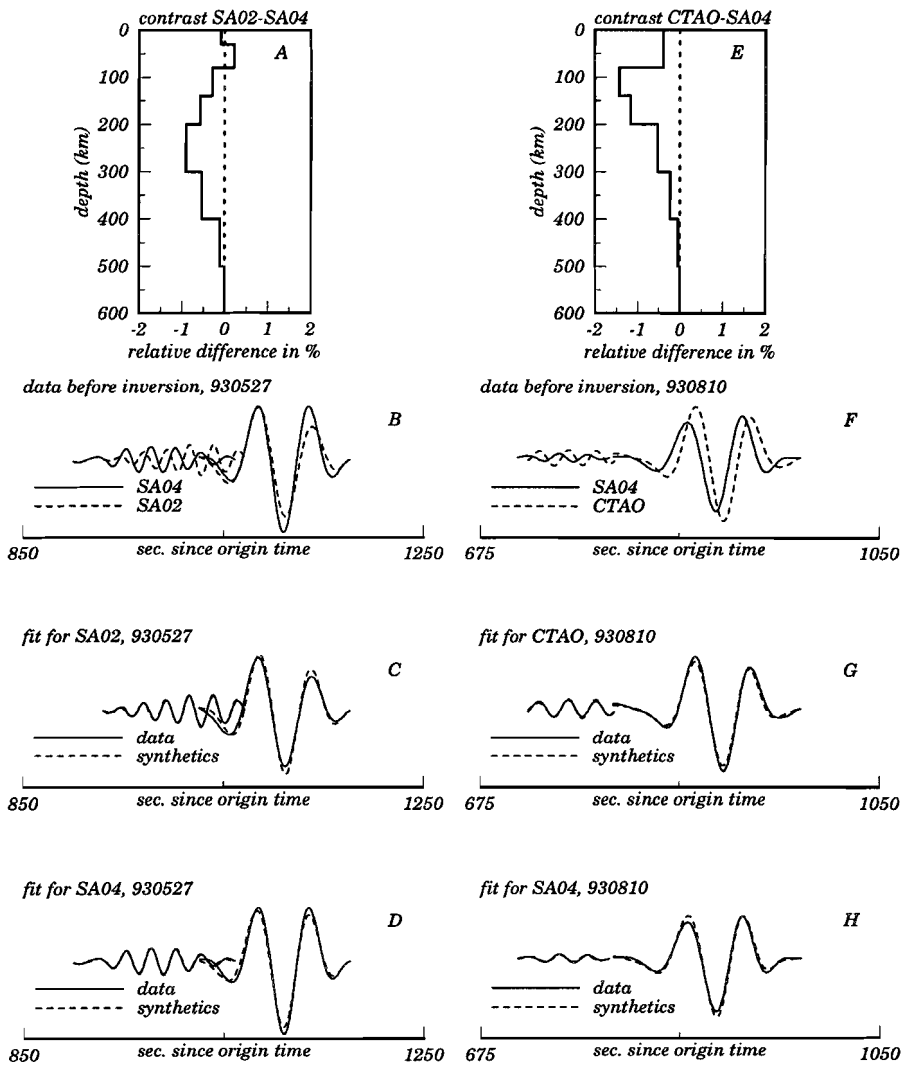


**Figure 6.7** Data (corrected for differences in epicentral distance), results, and fits for the case II inversions.

400 km. At shallower depth, the contrast is less pronounced (Figure 6.7a). This corresponds to the observation that the fundamental mode arrives simultaneously at the two stations, but that the higher mode energy arrives earlier at SA04 than at SA02. Figures 6.7c and 6.7d demonstrate that the waveform fits obtained from the model are good. In contrast to this event, inversion of the data of the 930810 event reveals that the depth interval where the path to SA04 is faster than the path to CTAO is mainly restricted to shallower levels between 80 and 200 km (Figure 6.7e). Again, the obtained fits to the data are good (Figures 6.7g and 6.7h).

For each event, the oceanic structure under the paths from the events to the stations does not show large differences (Figures 6.3 and 6.5). We therefore assumed that the velocity contrasts obtained by the inversions must be located along the part of the propagation path where at least one of the two paths is traveling through continental structure. Our inversion results, in combination with the orientation of the used paths, suggest a strong component of the velocity gradient from the northeast to the southwest in the uppermost mantle under northeast Australia. For the deeper levels, we find a strong component of the velocity gradient in the north-south direction. These observations correspond well with the structure obtained from PWI. Following the results of *Zielhuis and Van der Hilst* [1996] (Figure 6.3), we conclude that it is most likely that the differences we observe in the waveforms are mainly caused by a dominating contrast, centered around 140 km depth, between low velocities along the northeastern continental margin and high velocities southwest of this low velocity belt. Also, at larger depths, the contrast between high velocities under the Mt. Isa block and New England fold belt and lower velocities north of that area contributes to observed phase differences in the waveforms.

The direct measurements of the gradients (and also the local measurements of the case I examples) can be added to large-scale inversions as independent constraints. We assumed that for both case II examples the measured gradients are from continental origin (i.e., no contributions from the parts where both paths travel through oceanic structure). This means that for both examples approximately one third of the total structure along each path must be the cause of the observed gradients. This implies that the analysis of the 930810 event suggests a contrast of about 3 to 4% in the uppermost mantle beneath the continent. This is less than the value suggested by the models obtained by PWI and by the case I experiments, which is about 6%. This discrepancy might be due to effects of structure along the oceanic parts of the paths. These effects have been assumed to be negligible, but might in reality contribute to a small part of the observed phase shifts. Analysis of the data of the 930527 event suggests a contrast of up to about 3% in the deeper areas of the region. This coincides well with the value according to the models obtained by

PWI.

## 6.4 Conclusions

The waveform inversion method explained in Chapter 3 yields estimates of local structure and average velocity gradients. In this chapter, this technique has been used as an independent tool to test specific features (and their amplitudes) of a three-dimensional tomographic model. As an example, we have tested features of a recent  $S$  velocity model of the Australian region by *Zielhuis and Van der Hilst* [1996]. This has been accomplished by applying the technique to 20 Rayleigh wave waveforms recorded on the Australian continent. Using only these few waveforms, we have obtained various local measurements of the  $S$  velocity structure at different positions on the continent. In this way, we do not suffer from several disadvantages associated with large-scale tomographic imaging techniques.

Since our results confirm the major characteristics of the model of the Australian region, they provide illustrative examples of how specific features of a complex velocity structure can be easily visualized and/or verified by applying the inversion technique of Chapter 3 to only a few waveforms. For such a test, the role of the relatively short paths between the stations in the case I examples is crucial. The use of short paths increases the resolution by reducing the low-pass character of the data [*Passier and Snieder, 1995a*]. Since structural differences directly translate into observable phase differences between recorded waveforms, the examples in this chapter not only demonstrate the possibility of using the method as an independent testing tool, but the technique also provides a way to obtain results that can be used as constraints in subsequent large-scale inversions of much larger datasets.

# Appendix A

## Ray tracing on a sphere

In this appendix the theory of the kinematic ray tracing and the construction of the synthetic amplitude spectra is explained. Let, in a cartesian coordinate system,  $\mathbf{r}$  be the ray position,  $s$  the arc length along the ray and  $c$  the phase velocity of the medium. From the eikonal equation the first order system

$$\frac{d\mathbf{r}}{ds} = c\mathbf{p}$$
$$\frac{d\mathbf{p}}{ds} = \nabla \left( \frac{1}{c} \right)$$

follows. Considering surface-waves propagating in a two-dimensional horizontal plane, this system represents four first order differential equations. If  $x$  is the direction of the ray in a homogeneous medium and the  $y$ -direction is perpendicular to  $x$ , then with

$$\frac{d}{ds} = \frac{dx}{ds} \frac{d}{dx} = cp_x \frac{d}{dx} \quad \text{and} \quad p_x = \left( \frac{1}{c^2} - p_y^2 \right)^{1/2}$$

two first order differential equations are left to be solved:

$$\frac{dy}{dx} = \frac{p_y}{\left( \frac{1}{c^2} - p_y^2 \right)^{1/2}}$$
$$\frac{dp_y}{dx} = \frac{1}{c \left( \frac{1}{c^2} - p_y^2 \right)^{1/2}} \partial_y \left( \frac{1}{c} \right) . \quad (\text{A.1})$$

These coupled equations can be solved for  $p_y$  and  $y$  as a function of  $x$ . However, these equations are for ray tracing in a two-dimensional cartesian coordinate system.

Therefore an operation is needed, which transforms the problem of ray tracing on a sphere to the ray tracing problem in cartesian coordinates. For this purposes the Mercator transformation proposed by *Jobert and Jobert* [1983] was chosen:

$$x = \phi$$

$$y = \ln(\tan(\theta/2))$$

together with the transformation for the velocity  $c$ :

$$c_{trans}(x, y) = \frac{c(\theta, \phi)}{\sin(\theta)} = c(x, y) \cosh(y) , \quad (\text{A.2})$$

where  $\theta$  is the colatitude and  $\phi$  the longitude. The wave equation on a sphere becomes after this transformation

$$\partial_{xx}^2 u + \partial_{yy}^2 u = \frac{1}{c_{trans}^2(x, y)} \partial_{tt}^2 u ,$$

which is exactly the wave equation in cartesian coordinates with local velocity  $c_{trans}(x, y)$ . This means that in  $(x, y)$  space rays can be traced by solving the set of the two first order differential equations (A.1). The velocities  $c$  defined on a sphere were transformed into  $c_{trans}$ . This  $c_{trans}$  was then used in equations (A.1) to trace rays through the transformed velocity field. The equations were solved numerically using a fourth order Runge-Kutta integrator [*Press et al.*, 1990] with a step-size of  $1^\circ$ .

In Figure A.1a a schematic representation of a bundle of rays is shown. The source and the station are situated on the equator. The rays leave the source with different azimuths. In the example of Figure A.1a the equator is crossed at the location of the station between ray #3 and ray #4. The same occurs between ray #5 and ray #6. A crossing of the equator at a station location means that the station will register an arrival. The ray configuration of Figure A.1a will therefore yield two arrivals for the station shown. In the experiments 400 rays were shot over a total azimuthal range of  $140^\circ$ . Increasing the ray density did not alter the complexity of the obtained amplitude spectra. We therefore concluded that shooting 400 rays over a azimuthal range of  $140^\circ$  was an adequate setup for our analysis. By interpolating the travel times along two rays on both sides of an arrival the arrival time was found. Figure A.1b illustrates how the relative amplitudes of the arrivals were determined. The relative amplitudes are inversely proportional to the square root of the width of the ray tube. The width of a ray tube is defined as the distance between two rays that yield an arrival. In Figure A.1b a small width ( $dw_1$ ) and

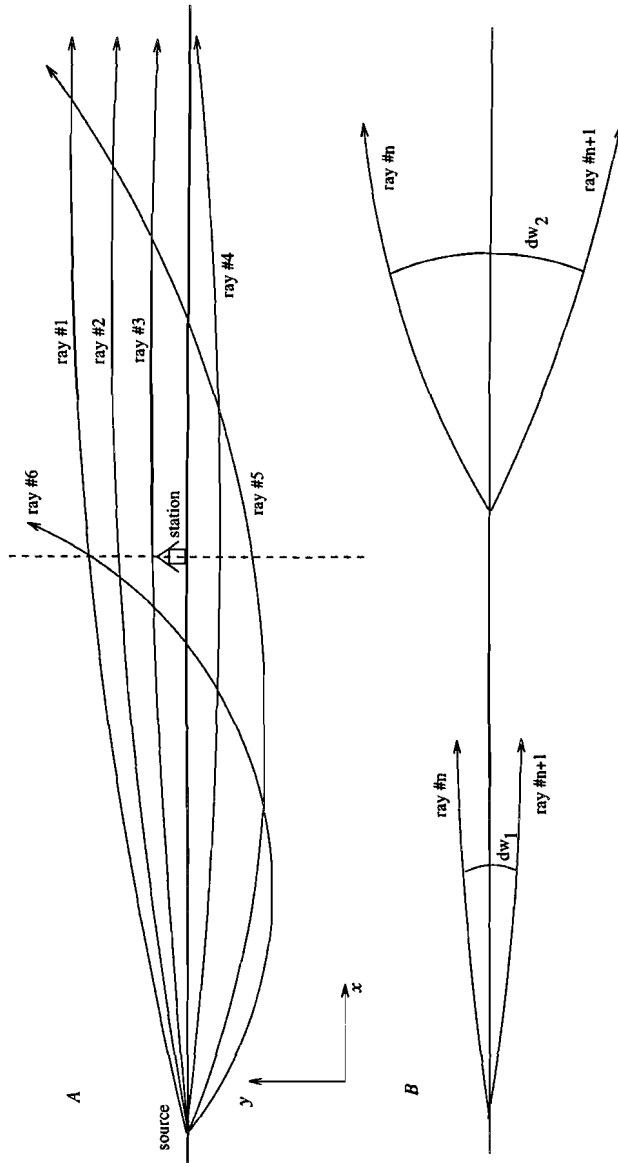


**Figure A.1** Schematic illustration of the determination of (a) the number of arrivals in a station and (b) the relative amplitudes of the arrivals.



a large width ( $dw_2$ ) are shown. The arrival between the rays separated by  $dw_1$  will have a larger amplitude than the arrival between the rays separated by  $dw_2$ . This way of determining relative amplitudes is based on the energy flux over the surface [*Aki and Richards, 1980*]. Note that at a caustic, where rays cross, this does not hold any more as the width goes to zero and the amplitude diverges. If two successive rays crossed exactly at the location of the station, the arrival was excluded from the analysis. However, the number of arrivals that was excluded for this reason could be neglected in comparison with the number of arrivals for which an amplitude determination based on the width of a ray tube was possible.

# References

- Aki, K. & Richards, P.G., 1980. *Quantitative Seismology*, W.H. Freeman, New York.
- Alsina, D. & Snieder, R.K., 1996. Constraints on the velocity structure beneath the Tornquist-Teisseyre zone from beamforming analysis, *Geophys. J. Int.*, in press.
- Ampferer, O., 1906. Über das Bewegungsbild von Faltengebirgen, *Jahrb. Kais. Kön. geol. Reichsanst.*, **56**, 539–622.
- Anderson, D.L., 1988. Temperature and pressure derivatives of elastic constants with application to the mantle, *J. geophys. Res.*, **93**, 4688–4700.
- Anderson, D.L., 1989. *Theory of the earth*, Blackwell, Oxford.
- Atwater, T., 1989. Plate tectonic history of the northeast Pacific and western North America, in *The eastern Pacific ocean and Hawaii*, pp. 21–72, eds. E.L. Winterer, D.M. Hussong & R.W. Decker, The geology of North America, N, Geol. Soc. Am., Boulder.
- Babuška, V. & Plomerová, J., 1988. Subcrustal continental lithosphere: a model of its thickness and anisotropic structure, *Phys. Earth planet. Inter.*, **51**, 130–132.
- Babuška, V., Plomerová, J. & Granet, M., 1990. The deep lithosphere in the Alps: a model inferred from *P* residuals, *Tectonophysics*, **176**, 137–165.
- Babuška, V., Plomerová, J. & Šílený, J., 1984. Large-scale oriented structures in the subcrustal lithosphere of central Europe, *Ann. Geophys.*, **2**, 649–662.
- Babuška, V., Plomerová, J. & Šílený, J., 1987. Structural model of the subcrustal lithosphere in central Europe, in *Composition, structure and dynamics of the lithosphere-asthenosphere system*, pp. 239–251, eds. K. Fuchs & C. Froidevaux, AGU, Washington DC.
- Bachmann, G.H., Müller, M. & Weggen, K., 1987. Evolution of the Molasse basin (Germany, Switzerland), *Tectonophysics*, **137**, 77–92.
- Berezin, I.S. & Zhidkov, N.P., 1965. *Computing methods, vol. II*, Pergamon.
- Bird, P., 1984. Laramide crustal thickening event in the Rocky Mountain foreland and Great Plains, *Tectonics*, **3**, 741–758.
- Blundell, D., Freeman, R. & Mueller, S. (Eds.), 1992. *A Continent Revealed, the European Geotraverse*, Cambridge Univ. Press, New York.

- Bonjer, K.-P., Gelbke, C., Gilg, B., Rouland, D., Mayer-Rosa, D. & Massinon, B., 1984. Seismicity and dynamics of the upper Rhine Graben, *J. Geophys.*, **55**, 1-12.
- Boyd, F.R. & Meyer, H.O.A., 1979. *The mantle sample*, AGU, Washington DC.
- Boyd, F.R., Pearson, D.G., Nixon, P.H. & Mertzman, S.A., 1993. Low-calcium garnet harzburgites from southern Africa; their relations to craton structure and diamond crystallization, *Contr. Min. Petr.*, **113**, 352-366.
- Brune, J. & Dorman, J., 1963. Seismic waves and Earth structures in the Canadian shield, *Bull. seism. Soc. Am.*, **53**, 167-210.
- Buttkus, B. (Ed.), 1986. *Ten years of the Gräfenberg array: defining the frontiers of broadband seismology*, Wittmann and Wäsch, Gehrden.
- Cara, M., 1978. Regional variations of higher Rayleigh mode phase velocities, a spatial filtering method, *Geophys. J. R. astr. Soc.*, **54**, 439-460.
- Carlson, R.W., 1994. Mechanisms of earth differentiation: consequences for the chemical structure of the mantle, *Rev. Geophys.*, **32**, 337-361.
- Carney, J.N. & MacFarlane, A., 1982. Geologic evidence bearing on the Miocene to recent structural evolution of the New Hebrides arc, the evolution of the India-Pacific plate boundaries, *Tectonophysics*, **87**, 147-175.
- Carslaw, H.S. & Jaeger, J.C., 1959. *Conduction of heat in solids*, Oxford Univ. Press, Oxford.
- Čermák, V., Balling, N., Della Vedova, B., Lucazeau, F., Pasquale, V., Pellis, G., Schulz, R. & Verdoya, M., 1992. Heat flow density map, scale 1:2,500,000, in *A Continent Revealed, the European Geotraverse—Atlas of Compiled Data*, Map 13, eds. R. Freeman & St. Mueller, Cambridge Univ. Press, New York.
- Christensen, N.I., 1984. Seismic velocities, in *Handbook of physical properties of rocks*, **2**, pp. 1-228, ed. R.S. Carmichael, CRC Press, Boca Raton.
- Christensen, N.I. & Smewing, J.D., 1981. Geology and seismic structure of the northern section of the Oman ophiolite, *J. geophys. Res.*, **86**, 2545-2555.
- Clark, S.P. & Ringwood, A.E., 1964. Density distribution and constitution of the mantle, *Rev. Geophys.*, **2**, 35-88.
- De Jonge, M.R., 1995. *Geodynamic evolution and mantle structure*, Ph.D. Thesis, Utrecht University, Utrecht.
- Dercourt, J., Zonenshain, L.P., Ricou, L.E., Kazmin, V.G., Le Pichon, X., Knipper, A.L., Grandjacquet, C., Sbertshikov, I.M., Geysant, J., Lepvrier, C., Percher-sky, D.H., Boulin, J., Sibuet, J.C., Savostin, L.A., Sorokhtin, O., Westphal, M., Bazhenov, M.L., Lauer, J.P. & Biju-Duval, B., 1986. Geological evolution

- of the Tethys from the Atlantic to the Pamirs since the Lias, *Tectonophysics*, **123**, 241–315.
- Dewey, J.F., Helman, M.L., Turco, E., Hutton, D.H.W. & Knott, S.D., 1989. Kinematics of the western Mediterranean, in *Alpine Tectonics*, pp. 265–283, eds. M.P. Coward, D. Dietrich & R.G. Park, *Geol. Soc. Lond. Spec. Publ. #45*, Blackwell, Oxford.
- Dost, B., 1990. Upper mantle structure under western Europe from fundamental and higher mode surface waves using the NARS array, *Geophys. J. Int.*, **100**, 131–151.
- Dziewonski, A.M. & Anderson, D.L., 1981. Preliminary reference earth model, *Phys. Earth planet. Inter.*, **25**, 297–356.
- Edel, J.B. & Fluck, P., 1989. The upper Rhenish Shield basement (Vosges, upper Rhine Graben and Schwarzwald): main structural features deduced from the magnetic, gravimetric and geological data, *Tectonophysics*, **169**, 303–316.
- Faber, S. & Aichele, H., 1986. The structure of the lithosphere beneath the Gräfenberg array, in *Ten years of the Gräfenberg array: defining the frontiers of broadband seismology*, pp. 83–88, ed. B. Buttkus, Wittmann and Wäsch, Gehrden.
- Faber, S., Plomerová, J. & Babuška, V., 1986. Deep-seated lateral velocity variations beneath the GRF array inferred from mislocation patterns and *P* residuals, *J. Geophys.*, **60**, 139–148.
- Fuchs, K., Bonjer, K.-P., Gajewski, D., Lüschen, E., Prodehl, C., Sandmeier, K.-J., Wenzel, F. & Wilhelm, H., 1987. Crustal evolution of the Rhine Graben area. 1. Exploring the lower crust in the Rhine Graben rift by unified geophysical experiments, *Tectonophysics*, **141**, 261–275.
- Fuchs, K. & Wedepohl, K., 1983. Relation of geophysical and petrological models of upper mantle structure of the Rhenish Massif, in *Plateau Uplift, the Rhenish Shield—A case history*, pp. 352–363, eds. K. Fuchs, K. von Gehlen, H. Mälzer, H. Murawski & A. Semmel, Springer Verlag, Berlin.
- Gear, C.W., 1971. *Numerical initial value problems in ordinary differential equations*, Prentice Hall, Englewood Cliffs.
- Geologische Karte von Bayern 1:500,000 + Erläuterungen, 1981. Bayer. Geol. Landesamt, München.
- Giese, P., 1976. The basis features of crustal structures in relation to the main geological units, in *Explosion seismology in central Europe*, pp. 221–241, eds. P. Giese, C. Prodehl & A. Stein, Springer Verlag, Berlin.

- Glahn, A. & Granet, M., 1992. 3-D structure of the lithosphere beneath the southern Rhine Graben area, *Tectonophysics*, **208**, 149–158.
- Glahn, A., Granet, M. & the Rhine Graben Teleseismic Group, 1993. Southern Rhine Graben: small-wavelength tomographic study and implications for the dynamic evolution of the graben, *Geophys. J. Int.*, **113**, 399–418.
- Glahn, A., Sachs, P.M. & Achauer, U., 1992. A teleseismic and petrological study of the crust and upper mantle beneath the geothermal anomaly Urach/SW-Germany, *Phys. Earth Planet. Inter.*, **69**, 176–206.
- Grand, S.P., 1994. Mantle shear structure beneath the Americas and surrounding oceans, *J. geophys. Res.*, **99**, 11591–11621.
- Granet, M., 1986. A teleseismic study of the upper Rhine Graben area: array mislocation diagram and 3-D velocity inversion, *J. Geophys.*, **59**, 119–128.
- Gubbins, D. & Snieder, R., 1991. Dispersion of P waves in subducted lithosphere: Evidence for an eclogite layer, *J. geophys. Res.*, **96**, 6321–6333.
- Gudmundsson, O., Davies, J.H. & Clayton, R.W., 1990. Stochastic analysis of global travel time data: mantle heterogeneity and random errors in the ISC data, *Geophys. J. Int.*, **102**, 25–43.
- Gutenberg, B., 1953. Wave velocities at depths between 50 and 600 kilometers, *Bull. seism. Soc. Am.*, **43**, 223–232.
- Gutenberg, B., 1959. The asthenosphere low velocity layer, *Ann. Geophys.*, **12**, 439–460.
- Guterch, A., Grad, M., Materzok, R. & Perchuc, E., 1986. Deep structure of the Earth's crust in the contact zone of the Palaeozoic and Precambrian platforms in Poland (Tornquist-Teisseyre Zone), *Tectonophysics*, **128**, 251–279.
- Gutscher, M.-A., 1995. Crustal structure and dynamics in the Rhine Graben and the Alpine foreland, *Geophys. J. Int.*, **122**, 617–636.
- Hadiouche, O., Kruger, F. & Kind, R., 1991. Mapping the crust in southeastern Germany using Rayleigh waves in the period range 6–16 s, *Geophys. Res. Lett.*, **18**, 1087–1090.
- Hamilton, W., 1979. Tectonics of the Indonesian region, *USGS prof. Pap.*, **1078**.
- Harjes, H.-P. & Seidl, D., 1978. Digital recording and analysis of broadband seismic data at the Gräfenberg (GRF)-array, *J. Geophys.*, **44**, 511–523.
- Harvey, D.J., 1981. Seismogram synthesis using normal mode superposition: The locked-mode approximation, *Geophys. J. R. astr. Soc.*, **66**, 37–70.
- Helfrich, G.R., Stein, S. & Wood, B.J., 1989. Subduction zone thermal structure and mineralogy and their relationship to seismic wave reflections and conversions at the slab/mantle interface, *J. geophys. Res.*, **94**, 753–763.

- Henk, A., 1993. Subsidenz und Tektonik des Saar-Nahe-Beckens (SW-Deutschland), *Geol. Rundschau*, **82**, 3–19.
- Holliger, K. & Kissling, E., 1992. Gravity interpretation of a unified acoustic 2D image of the central Alpine collision zone, *Geophys. J. Int.*, **111**, 213–225.
- Homewood, P., Allen, P.A. & Williams, G.D., 1986. Dynamics of the Molasse basin of western Switzerland, in *Foreland Basins*, pp. 199–217, eds. P.A. Allen & P. Homewood, Blackwell, Oxford.
- Hu, G. & Menke, W., 1992. Formal inversion of laterally heterogeneous velocity structure from *P*-wave polarization data, *Geophys. J. Int.*, **110**, 63–69.
- Huckenholz, H.G. & Kunzmann, T., 1993. Tertiärer Vulkanismus im Bayerischen Teil des Egergrabens und des Mesozoischen Vorlandes, *Berichte der Deutschen Mineralogischen Gesellschaft*, **2**, 1–34.
- Illies, J.H. & Fuchs, K. (Eds.), 1974. *Approaches to taphrogenesis*, Schweizerbart, Stuttgart.
- Illies, J.H. & Mueller, St. (Eds.), 1970. *Graben problems*, Schweizerbart, Stuttgart.
- Inoue, H., Fukao, Y., Tanabe, K. & Ogata, K., 1990. Whole mantle *P*-wave travel time tomography, *Phys. Earth planet. Inter.*, **59**, 294–328.
- Jacobshagen, V., 1976. Main geologic features of the Federal Republic of Germany, in *Explosion seismology in central Europe*, pp. 3–17, eds. P. Giese, C. Prodehl & A. Stein, Springer Verlag, Berlin.
- Jannane, H., Beydoen, W., Crase, E., Cao, D., Koren, Z., Landa, E., Menses, M., Pica, A., Noble, M., Roeth, G., Singh, S., Snieder, R., Tarantola, A., Trezeguet, D., & Xie, M., 1989. Wavelengths of earth structure that can be resolved from seismic reflection data, *Geophysics*, **54**, 906–910.
- Jobert, N. & Jobert, G., 1983. An application of ray theory to the propagation of waves along a laterally heterogeneous spherical surface, *Geophys. Res. Lett.*, **10**, 1148–1151.
- Kahle, H.-G. & Werner, D., 1980. A geophysical study of the Rhine Graben, II; Gravity anomalies and geothermal applications, *Geophys. J. R. astr. Soc.*, **62**, 631–647.
- Karig, D.E. & Mammerickx, J., 1972. Tectonic framework of the New Hebrides island arc, *Mar. Geol.*, **12**, 187–205.
- Kawakatsu, H., 1983. Can 'pure-path' models explain free oscillation data?, *Geophys. Res. Lett.*, **10**, 186–189.
- Kennett, B.L.N. & Van der Hilst, R.D., 1996. Using a synthetic continental array in Australia to study the Earth's interior, *J. Phys. Earth*, in press.

- Kissling, E., 1993. Deep structure of the Alps—what do we really know?, *Phys. Earth Planet. Inter.*, **79**, 87–112.
- Knopoff, L., 1972. Observation and inversion of surface wave dispersion, *Tectonophysics*, **13**, 497–519.
- Knopoff, L., Mueller, S. & Pilant, W.L., 1966. Structure of the crust and upper mantle in the Alps from the phase velocity of Rayleigh waves, *Bull. seism. Soc. Am.*, **56**, 1009–1044.
- Knopoff, L., Berry, M.J. & Schwab, F.A., 1967. Tripartite phase velocity observations in laterally heterogeneous regions, *J. geophys. Res.*, **72**, 2595–2601.
- Kraus, E.C., 1931. Die Alpen als Doppelorogen, *Geol. Rundschau*, **22**, 65–78.
- Kushnir, A.F., Levshin, A.L. & Lokshtanov, D.E., 1988. Determination of the velocity section from the spectra of surface waves by nonlinear optimization methods, in *Computational Seismology: Earthquake Prediction and the Structure of the Earth*, vol. 21, pp. 127–141, Allerton, New York.
- Kushnir, A.F., Levshin, A.L. & Lokshtanov, D.E., 1989. Determination of a regional velocity structure from surface wave seismograms recorded at a set of stations, in *Proceedings of the Sixth International Mathematical Geophysics Seminar*, vol. 3, pp. 489–498, Free Univ., Berlin, Germany.
- Landisman, M., Dziewonski, A.M. & Sato, Y., 1969. Recent improvements in the analysis of surface wave observations, *Geophys. J. R. astr. Soc.*, **17**, 369–403.
- Laske, G., Masters, G. & Zürn, W., 1994. Frequency-dependent polarization measurements of long-period surface waves and their implications for global phase-velocity maps, *Phys. Earth planet. Inter.*, **84**, 111–137.
- Laubscher, H.P., 1985. The tectonics of the western and southern Alps: Correlation between surface observations and deep structure, in *Second EGT workshop—the southern segment*, pp. 93–101, eds. D.A. Galson & St. Mueller, European Science Foundation, Strasbourg, France.
- Lay, T. & Kanamori, H., 1985. Geometric effects of global lateral heterogeneity on long-period surface wave propagation, *J. geophys. Res.*, **90**, 605–621.
- Lehmann, I., 1961. *S* and structure of the upper mantle, *Geophys. J. R. astr. Soc.*, **4**, 124–138.
- Lemcke, K., 1974. Vertikalbewegung des vorgesozoischen Sockels im Nördlichen Alpenvorland vom Perm bis zur Gegenwart, *Ecl. geol. Helv.*, **67**, 121–133.
- Lerner-Lam, A.L., & Jordan, T.H., 1983. Earth structure from fundamental and higher mode waveform analysis, *Geophys. J. R. astr. Soc.*, **75**, 759–797.
- Levshin, A.L., Ritzwoller, M.H. & Ratnikova, L.I., 1994. The nature and cause of polarization anomalies of surface waves crossing northern and central Eurasia, *Geophys. J. Int.*, **117**, 577–590.

- Lewis, S.D. & Hayes, D.E., 1980. The tectonics of northward propagating subduction along eastern Luzon, Philippine islands, in *The tectonic and geologic evolution of southeast Asian seas and islands*, pp. 57–78, ed. D.E. Hayes, AGU, Geophys. Monogr. Ser. Vol. 27, Washington DC.
- Lipman, P.W., Prostka, H.J. & Christiansen, R.L., 1971. Evolving subduction zones in the western United States, as interpreted from igneous rocks, *Science*, **174**, 821–825.
- Lippolt, H., Todt, W. & Horn, P., 1974. Apparent potassium-argon ages of lower Tertiary Rhine Graben volcanics, in *Approaches to taphrogenesis*, pp. 213–221, eds. J. Illies et al., Schweizerbart, Stuttgart.
- Lomax, A., & Snieder, R., 1994. Finding sets of acceptable solutions with a genetic algorithm with application to surface wave group dispersion in Europe, *Geophys. Res. Lett.*, **21**, 2617–2620.
- Lyon-Caen, H. & Molnar, P., 1989. Constraints on the deep structure and dynamic processes beneath the Alps and adjacent regions from an analysis of gravity anomalies, *Geophys. J. Int.*, **99**, 19–32.
- Manghnani, M.H. & Ramanantoandro, R., 1974. Compressional and shear wave velocities in granulite facies rocks and eclogites to 10 kbar, *J. geophys. Res.*, **79**, 5427–5446.
- Marquering, H., & Snieder, R., 1995. Surface wave mode coupling for efficient forward modeling and inversion of body wave phases, *Geophys. J. Int.*, **120**, 186–208.
- Marquering, H., Snieder, R., & Nolet, G., 1996. Waveform inversions and the significance of surface-wave mode coupling, *Geophys. J. Int.*, **124**, 258–278.
- Mayer-Rosa, D. & Mueller, St., 1973. The gross velocity-depth distribution of P- and S-waves in the upper mantle of Europe from earthquake observations, *Zeitschr. Geophys.*, **39**, 395–410.
- Meissner, R., 1986. *The Continental Crust*, Academic, San Diego, Calif.
- Meissner, R. & Tanner, B., 1993. From collision to collapse: phases of lithospheric evolution as monitored by seismic records, *Phys. Earth Planet. Inter.*, **79**, 75–86.
- Meissner, R., Wever, Th. & Flüh, E.R., 1987. The Moho in Europe—implications for crustal development, *Ann. Geophys.*, **5**, 357–364.
- Menke, W., 1984. *Geophysical Data Analysis: Discrete Inverse Theory*, Academic, San Diego, Calif.
- Menzies, M.A., Fan, W. & Zhang, M., 1993. Palaeozoic and Cenozoic lithoprobes and the loss of > 120 km of Archaean lithosphere, Sino-Korean craton, China,



- in *Magmatic processes and plate tectonics*, pp.71–81, eds. H.M. Prichard, T. Alabaster, N.B.W. Harris & Neary, C.R., *Geol. Soc. Spec. Publ. #76*, Univ. Wales Coll. Cardiff, Cardiff.
- Mochizuki, E., 1993. Spherical harmonic analysis in terms of line integral, *Phys. Earth planet. Inter.*, **76**, 97–101.
- Montagner, J.P., 1994. Can seismology tell us anything about convection in the mantle?, *Rev. Geophys.*, **32**, 115–138.
- Montagner, J.P. & Tanimoto, T., 1991. Global upper mantle tomography of seismic velocities and anisotropies, *J. geophys. Res.*, **96**, 20337–20351.
- Mueller, St., 1989. Deep-reaching geodynamic processes in the Alps, in *Alpine Tectonics*, pp. 303–328, eds. M.P. Coward, D. Dietrich & R.G. Park, *Geol. Soc. Lond. Spec. Publ. #45*, Blackwell, Oxford.
- Mueller, St. & Panza, G.F., 1986. Evidence of a deep-reaching lithospheric root under the Alpine arc, in *The origin of arcs*, pp. 93–113, ed. F.-C. Wezel, Elsevier, Amsterdam.
- Müller, B., Zoback, M.L., Fuchs, K., Mastin, L., Gregersen, S., Pavoni, N., Stephansson, O. & Ljunggren, C., 1992. Regional patterns of tectonic stress in Europe, *J. geophys. Res.*, **97**, 11783–11803.
- Neele, F., VanDecar, J.C. & Snieder, R.K., 1993a. A formalism for including amplitude data in tomographic inversions, *Geophys. J. Int.*, **115**, 482–496.
- Neele, F., VanDecar, J.C. & Snieder, R.K., 1993b. The use of P-wave amplitude data in joint inversions with travel times for upper-mantle velocity structure, *J. geophys. Res.*, **98**, 12033–12054.
- Nolet, G., 1975. Higher Rayleigh modes in Western Europe, *Geophys. Res. Lett.*, **2**, 60–62.
- Nolet, G., 1990. Partitioned waveform inversion and two-dimensional structure under the Network of Autonomously Recording seismographs, *J. geophys. Res.*, **95**, 8499–8512.
- Nolet, G., Dost, B. & Paulssen, H., 1986a. Intermediate wavelength seismology and the NARS experiment, *Ann. Geophysicae*, **4**, 305–314.
- Nolet, G., Dost, B., & Paulssen, H., 1986b. The upper mantle under Europe: an interpretation of some preliminary results from the NARS project, *Geol. Mijnbouw*, **65**, 155–165.
- Nolet, G., Grand, S.P. & Kennett, B.L.N., 1994. Seismic heterogeneity in the upper mantle, *J. geophys. Res.*, **99**, 23753–23766.
- Nolet, G. & Panza, G.F., 1976. Array analysis of seismic surface waves: Limits and possibilities, *Pure Appl. Geophys.*, **114**, 775–790.

- Nolet, G., Sleeman, R., Nijhof, V. & Kennett, B.L.N., 1989. Synthetic reflection seismograms in three dimensions by a locked-mode approximation, *Geophysics*, **54**, 350–358.
- Nolet, G., Van Trier, J. & Huisman, R., 1986c. A formalism for nonlinear inversion of seismic surface waves, *Geophys. Res. Lett.*, **13**, 26–29.
- Paige, C.C. & Saunders, M.A., 1982. LSQR: an algorithm for sparse linear equations and sparse least squares, *ACM Trans. Math. Soft.*, **8**, 43–71 and 195–209.
- Panza, G.F., 1985. Lateral variations in the lithosphere in correspondence of the southern segment of EGT, in *Second EGT workshop: The southern segment*, pp. 47–51, eds. D.A. Galson & St. Mueller, ESF, Strasbourg.
- Panza, G.F. & Mueller, St., 1978. The plate boundary between Eurasia and Africa in the Alpine area, *Mem. Sci. Geol. Univ. Padova*, **33**, 43–50.
- Panza, G.F., Mueller, St. & Calcagnile, G., 1980. The gross features of the lithosphere-asthenosphere system in Europe from seismic surface waves and body waves, *Pure Appl. Geophys.*, **118**, 1209–1213.
- Passier, M.L. & Snieder, R.K., 1995a. On the presence of intermediate-scale heterogeneity in the upper mantle, *Geophys. J. Int.*, **123**, 817–837.
- Passier, M.L. & Snieder, R.K., 1995b. Using differential waveform data to retrieve local *S* velocity structure or path-averaged *S* velocity gradients, *J. geophys. Res.*, **100**, 24061–24078.
- Passier, M.L. & Snieder, R.K., 1996. Correlation between shear-wave upper mantle structure and tectonic surface expressions: application to central and southern Germany, *J. geophys. Res.*, in press.
- Pedersen, H.A., Campillo, M. & Balling, N., 1994. Changes in the lithospheric structure across the Sorgenfrei-Tornquist Zone inferred from dispersion of Rayleigh waves, *Earth planet. Sci. Lett.*, **128**, 37–46.
- Pfiffner, O.A., 1986. Evolution of the north Alpine foreland basin in the Central Alps, in *Foreland Basins*, pp. 219–228, eds. P.A. Allen & P. Homewood, Blackwell, Oxford.
- Pfiffner, O.A., Frei, W., Valasek, P., Stäuble, M., DuBois, L., Levato, L., Schmid, S. & Smithson, S.B., 1990. Crustal shortening in the Alpine orogen: results from deep seismic reflection profiling in the eastern Swiss Alps—line NFP 20-EAST, *Tectonics*, **9**, 1327–1356.
- Plaumann, S., 1987. Karte der Bougueranomalien in der Bundesrepublik Deutschland 1:1,500,000, *Geol. Jahrb.*, **E40**, 3–7.

- Plaumann, S., 1988. Kompilation einer Schwerekarte für die westliche ČSSR, das Erzgebirge (DDR) und Nordostbayern, *Zeitschrift der Deutschen Geologischen Gesellschaft*, **139**, 177–190.
- Plomerová, J. & Babuška, V., 1988. Lithosphere thickness in the contact zone of the Moldanubicum and Saxothuringicum in central Europe, *Phys. Earth planet. Inter.*, **51**, 159–165.
- Pollitz, F.F., 1994. Global tomography from Rayleigh and Love wave dispersion: effect of ray-path bending, *Geophys. J. Int.*, **118**, 730–758.
- Press, F., 1956. Determination of crustal structure from phase velocity of Rayleigh waves part 1, southern California, *Bull. geol. Soc. Am.*, **67**, 1647–1658.
- Press, W.H., Flannery, B.P., Teukolsky, S.A. & Vetterling, W.T., 1990. *Numerical Recipes*, Cambridge University Press, Cambridge.
- Prodehl, C., Mueller, St., Glahn, A., Gutscher, M. & Haak, V., 1992. Lithospheric cross sections of the European Cenozoic rift system, *Tectonophysics*, **208**, 113–138.
- Prodehl, C., Mueller, St. & Haak, V., 1995. The European Cenozoic rift system, in *Continental rifts: evolution, structure, tectonics*, pp. 133–212, ed. K.H. Olsen, Elsevier, Amsterdam.
- Pulliam, R.J., Vasco, D.W. & Johnson, L.R., 1993. Tomographic Inversions for Mantle *P* wave Velocity Structure Based on the Minimization of  $l^2$  and  $l^1$  Norms of International Seismological Centre Travel Time Residuals, *J. geophys. Res.*, **98**, 699–734.
- Raikes, S., 1980. Teleseismic evidence for velocity heterogeneity beneath the Rhenish Massif, *J. Geophys.*, **48**, 80–83.
- Raikes, S. & Bonjer, K.-P., 1983. Large-scale mantle heterogeneity beneath the Rhenish Massif and its vicinity from teleseismic *P* residuals measurements, in *Plateau uplift, the Rhenish Shield—A case history*, pp. 315–331, eds. K. Fuchs, K. von Gehlen, H. Mälzer, H. Murawski & A. Semmel, Springer Verlag, Berlin.
- Reichenbach, H. & Mueller, St., 1974. Ein Krusten-Mantel-Modell für das Riftsystem um den Rheingraben, abgeleitet aus der Dispersion von Rayleigh-Wellen, in *Approaches to taphrogenesis*, pp. 348–354, ed. J.H. Illies & K. Fuchs, Schweizerbart, Stuttgart.
- Richter, M., 1951. Molasse und Alpen, *Zeitschrift der Deutschen Geologischen Gesellschaft*, **102**, 177–180.
- Ringwood, A.E., 1975. *Composition and petrology of the earth's mantle*, McGraw-Hill, New York.

- Ringwood, A.E. & Green, D.H., 1966. An experimental investigation of the gabbro-eclogite transformation and some geophysical implications, *Tectonophysics*, **3**, 383–427.
- Ritzwoller, M.H. & Lavelly, E.M., 1995. Three-dimensional seismic models of the earth's mantle, *Rev. Geophys.*, **33**, 1–66.
- Romanowicz, B., 1987. Multiplet-multiplet coupling due to lateral heterogeneity: asymptotic effects on the amplitude and frequency of the earth's normal modes, *Geophys. J. R. astr. Soc.*, **90**, 75–100.
- Romanowicz, B., 1990. The Upper mantle degree 2: Constraints and inferences from global mantle wave attenuation measurements, *J. geophys. Res.*, **95**, 11051–11071.
- Romanowicz, B., 1994. On the measurement of anelastic attenuation using amplitudes of low frequency surface waves, *Phys. Earth planet. Int.*, **84**, 179–191.
- Romanowicz, B., Karczewski, J.F., Cara, M., Bernard, P., Borsenberger, J., Cantin, J.M., Dole, B., Fouassier, D., Koenig, J.C., Morand, M., Pillet, R., Pyrolley, A. & Rouland, D., 1991. The GEOSCOPE program; present status and perspectives, *Bull. seism. Soc. Am.*, **81**, 243–264.
- Rothé, J.P. & Sauer, K. (Eds.), 1967. *The Rhine Graben progress report 1967*, Abh. Geol. Landesamt Bade-Württemberg.
- Roult, G., Rouland, D. & Montagner, J.P., 1994. Antarctica II: Upper mantle structure from velocities and anisotropy, *Phys. Earth planet. Inter.*, **84**, 33–57.
- Salisbury, M. & Christensen, N.I., 1978. The seismic velocity structure of a traverse through the Bay of Islands ophiolite complex, Newfoundland, an exposure of oceanic crust and upper mantle, *J. geophys. Res.*, **83**, 805–817.
- Seidl, D. & Mueller, St., 1977. Seismische Oberflächenwellen, *J. Geophys.*, **42**, 283–328.
- Seidl, D., Reichenbach, H. & Mueller, St., 1970. Dispersion investigations of Rayleigh waves in the Rhinegraben rift system, in *Graben problems*, pp. 203–206, eds. J.H. Illies & St. Mueller, Schweizerbart, Stuttgart.
- Shaw, R.D., Welmann, P., Gunn, P., Whitaker, A.J., Tarlowski, C. & Morse, M.P., 1995. Australian Crustal Elements Map, *AGSO Research Newsletter*, **23**, 1–3.
- Snieder, R., 1986. 3-D linearized scattering of surface waves and a formalism for surface wave holography, *Geophys. J. R. astr. Soc.*, **84**, 581–605.
- Snieder, R., 1987. On the connection between ray theory and scattering theory for surface waves, in *Mathematical Geophysics*, pp. 77–84, edited by N.J. Vlaar et al., D. Reidel, Norwell, Mass.

- Snieder, R.K., 1988. Large-scale waveform inversion of surface waves for lateral heterogeneity: 2. Application to surface waves in Europe and the Mediterranean, *J. geophys. Res.*, **93**, 12067–12080.
- Snieder, R.K., Beckers, J. & Neele, F., 1991. The effect of small-scale structure on normal mode frequencies and global inversions, *J. geophys. Res.*, **96**, 501–515.
- Snieder, R. & Nolet, G., 1987. Linearized scattering of surface waves on a spherical Earth, *J. Geophys.*, **61**, 55–63.
- Snieder, R.K., & Romanowicz, B., 1988. A new formalism for the effect of lateral heterogeneity on normal modes and surface waves I; Isotropic perturbations, perturbations of interfaces and gravitational perturbations, *Geophys. J. R. astr. Soc.*, **92**, 207–222.
- Spakman, W., 1986. The upper mantle structure in the central European Mediterranean region, in *Proc. of the Third Workshop on the European Geotraverse (EGT) project—the central segment*, pp. 215–221, eds. R. Freeman, St. Mueller & P. Giese, ESF, Strasbourg.
- Spakman, W., 1991. Delay-time tomography of the upper mantle below Europe, the Mediterranean, and Asia Minor, *Geophys. J. Int.*, **107**, 309–332.
- Spakman, W., Van der Lee, S. & Van der Hilst, R., 1993. Travel-time tomography of the European-Mediterranean mantle down to 1400 km, *Phys. Earth planet. Inter.*, **79**, 3–74.
- Stacey, F.D., 1992. *Physics of the earth*, Brookfield Press, Kenmore, Queensland, Australia.
- Stange, S. & Friederich, W., 1993. Surface wave dispersion and upper mantle structure beneath southern Germany from joint inversion of network recorded teleseismic events, *Geophys. Res. Lett.*, **20**, 2375–2378.
- Su, W.-J. & Dziewonski, A.M., 1991. Predominance of long-wavelength heterogeneity in the mantle, *Nature*, **352**, 121–126.
- Su, W.-J. & Dziewonski, A.M., 1992. On the scale of mantle heterogeneity, *Phys. Earth planet. Inter.*, **74**, 29–54.
- Su, W.-J., Woodward, R.L. & Dziewonski, A.M., 1992. Deep origin of mid-ocean-ridge seismic velocity anomalies, *Nature*, **360**, 149–152.
- Su, W.-J., Woodward, R.L. & Dziewonski, A.M., 1994. Degree 12 model of shear velocity heterogeneities in the mantle, *J. geophys. Res.*, **99**, 6945–6980.
- Sumino, Y. & Anderson, O.L., 1984. Elastic constants of minerals, in *Handbook of physical properties of rocks*, **3**, pp. 39–138, ed. R.S. Carmichael, CRC Press, Boca Raton.

- Tanimoto, T., 1991. Predominance of large-scale heterogeneity and the shift of velocity anomalies between the upper and lower mantle, *J. Phys. Earth*, **38**, 493–509.
- Tao, W.C. & O'Connell, R.J., 1992. Ablative subduction: a two-sided alternative to the conventional subduction model, *J. geophys. Res.*, **97**, 8877–8904.
- Trümpy, R., 1982. Alpine paleogeography: a reappraisal, in *Mountain building processes*, pp. 149–156, ed. K. Hsü, Academic Press, London.
- Turcotte, D.L. & Oxburgh, E.R., 1969. Convection in a mantle with variable physical properties, *J. geophys. Res.*, **74**, 1458–1474.
- Turcotte, D.L. & Schubert, G., 1982. *Geodynamics: applications of continuum physics to geological problems*, J. Wiley, New York.
- Valasek, P., Mueller, St., Frei, W. & Holliger, K., 1991. Results of NFP 20 seismic reflection profiling along the Alpine section of the European Geotraverse (EGT), *Geophys. J. Int.*, **105**, 85–102.
- Van der Hilst, R., Engdahl, R., Spakman, W. & Nolet, G., 1991. Tomographic imaging of subducted lithosphere below northwest Pacific island arcs, *Nature*, **353**, 37–43.
- Van der Hilst, R.D., Kennett, B.L.N., Christie, D. & Grant, J., 1994. SKIPPY: Mobile broad-band arrays to study the seismic structure of the lithosphere and mantle beneath Australia, *EOS Trans. Am. Geophys. Un.*, **75**, 177 & 180–181.
- Van der Hilst, R. & Snieder, R., 1996. Observations and numerical modelling of high-frequency precursors to P-wave arrivals at station SNZO New Zealand, *J. geophys. Res.*, **101**, 8473–8488.
- VanDecar, J.C., James, D.E. & Assumpção, 1995. Seismic evidence for a fossil mantle plume beneath South America and implications for plate driving forces, *Nature*, **378**, 25–31.
- Verhoogen, J., 1951. The adiabatic gradient in the mantle, *Trans. Am. geophys. Union*, **32**, 41.
- Vlaar, N.J., 1982. Lithospheric doubling as a cause of intracontinental tectonics, *Proc. Roy. Neth. Ac. Sc.*, **B85**, 469–483.
- Vlaar, N.J., 1983. Thermal anomalies and magmatism due to lithospheric doubling and shifting, *Earth Plan. Sc. Lett.*, **65**, 322–330.
- Vlaar, N.J. & Cloetingh, S.A.P.L., 1984. Orogeny and ophiolites: plate tectonics revisited with reference to the Alps, *Geol. Mijnbouw*, **63**, 159–164.
- Vlaar, N.J. & Wortel, M.J.R., 1976. Lithospheric aging, instability and subduction, *Tectonophysics*, **32**, 331–351.

- White, B., Nair, B. & Bayliss, A., 1988. Random rays and seismic amplitude anomalies, *Geophysics*, **53**, 903–907.
- Willett, S.D. & Beaumont, C., 1994. Subduction of Asian lithospheric mantle beneath Tibet inferred from models of continental collision, *Nature*, **369**, 642–645.
- Wilson, M. & Downes, H., 1991. Tertiary-Quaternary extension related alkaline magmatism in western and central Europe, *J. Petrol.*, **32**, 811–849.
- Wilson, M. & Downes, H., 1992. Mafic alkaline magmatism associated with the European Cenozoic rift system, *Tectonophysics*, **208**, 173–182.
- Wonik, T., Galdéano, A., Hahn, A. & Mouge, P., 1992. Magnetic anomalies map, scale 1:2,500,000, in *A Continent Revealed, the European Geotraverse—Atlas of Compiled Data*, Map 13, eds. R. Freeman & St. Mueller, Cambridge Univ. Press, New York.
- Woodhouse, J.H., 1974. Surface waves in a laterally varying structure, *Geophys. J. R. astr. Soc.*, **37**, 461–490.
- Woodhouse, J.H. & Dziewonski, A.M., 1984. Mapping the upper mantle: three-dimensional modeling of earth structure by inversion of seismic waveforms, *J. geophys. Res.*, **89**, 5953–5986.
- Woodhouse, J.H. & Wong, Y., 1986. Amplitude, phase and path anomalies of mantle waves, *Geophys. J. R. astr. Soc.*, **87**, 753–773.
- Woodward, R.L. & Masters, G., 1991. Lower mantle structure from long-period differential travel times, *Nature*, **352**, 231–233.
- Zeis, S., Gajewski, D. & Prodehl, C., 1990. Crustal structure of southern Germany from seismic refraction data, *Tectonophysics*, **176**, 59–86.
- Zhang, Y.-S. & Tanimoto, T., 1991. Global Love wave phase velocity variation and its significance to plate tectonics, *Phys. Earth planet. Inter.*, **66**, 160–202.
- Zhang, Y.-S. & Tanimoto, T., 1993. High-resolution global upper mantle structure and plate tectonics, *J. geophys. Res.*, **98**, 9793–9823.
- Ziegler, P.A., 1987. Late Cretaceous and Cenozoic intra-plate compressional deformations in the Alpine foreland—a geodynamic model, *Tectonophysics*, **137**, 389–420.
- Ziegler, P.A., 1990. *Geological atlas of Western and Central Europe*, SIPM, The Hague.
- Ziegler, P.A., 1992. European Cenozoic rift system, *Tectonophysics*, **208**, 91–111.
- Zielhuis, A. & Nolet, G., 1994. Shear-wave velocity variations in the upper mantle beneath Central Europe, *Geophys. J. Int.*, **117**, 695–715.

- Zielhuis, A. & Van der Hilst, R.D., 1996. Upper mantle shear velocity beneath eastern Australia from inversion of waveforms from SKIPPY portable arrays, *Geophys. J. Int.*, in press.



## Samenvatting in het Nederlands

In de seismologie houdt men zich bezig met de wiskundige en fysische bestudering van aardbevingen. Ook wordt onderzocht hoe de trillingen van de aarde, veroorzaakt door aardbevingen, gebruikt kunnen worden om tot uitspraken omtrent de inwendige structuur van de aarde te komen. Een deel van de seismologen richt zijn aandacht op het mechanisme van de bron. Zij proberen de eigenschappen van het breukproces te achterhalen als functie van tijd en plaats. Ook proberen ze te komen tot een statistische beschrijving van de verdeling van de aardbevings locaties, zowel in tijd als in plaats. Een ander deel van de seismologen houdt zich bezig met de voortplanting van de energie die vrijkomt als een aardbeving plaats vindt. Deze energie plant zich voort langs het aardoppervlak (oppervlaktegolven) en door het binnenste van de aarde (ruimtegolven). Deze tak van de seismologie houdt zich bezig met de beschrijving van het golfveld en de effecten op dit golfveld die veroorzaakt worden door heterogene structuren in de aarde die het golfveld onderweg tegen komt.

Een belangrijk doel voor veel seismologen is het bepalen van de binnenste structuur van de aarde. Pogingen om dit te bereiken maken gebruik van registraties van waarnemingen van de zich voortplantende energie die bij een aardbeving vrij komt. Ideeën over de interne structuur van de aarde kunnen verkregen worden door voorwaartse modellering of inverse modellering. Voorwaartse modellering houdt in dat de aan het oppervlak waarneembare effecten van in de aarde aanwezige structuren op het zich voortplantende golfveld gemodelleerd worden. Het resultaat wordt dan vergeleken met de waarnemingen. Bij inverse modellering worden de waarnemingen als uitgangspunt gebruikt om op een systematische manier een model van de aarde te vinden dat het beste de waarnemingen verklaart. In de seismologie worden deze inverse methodes vaak gebruikt om modellen te construeren van de seismische snelheden in de mantel en in de korst van de aarde. De waarnemingen die dan als uitgangspunt gebruikt worden, bestaan uit reistijden als ruimtegolven gebruikt worden of uit dispersiemetingen als oppervlaktegolven gebruikt worden.

De ontwikkeling van de seismologie in het algemeen, en de constructie door middel van inverse methodes van de zogenaamde tomografische modellen tot een diepte van enkele honderden kilometers in het bijzonder, heeft de laatste tientallen jaren enorm geprofiteerd van de snel toenemende omvang en beschikbaarheid van computer faciliteiten en data sets. Verschillende modellen van de drie-dimensionale verdeling van de seismische snelheden in de mantel van de aarde zijn tegenwoordig

beschikbaar, evenals een stel regionale modellen van de snelheden in de mantel in gebieden zoals Europa en de Middellandse Zee, Tibet, Antarctica, Noord-Amerika, zuid Brazilië, enz. Voor het grootste deel van de wereld zijn er echter geen regionale modellen beschikbaar. Door de beperkte verdeling van seismiciteit en stations op de aarde is het ook niet erg waarschijnlijk dat een aanzienlijk deel van de aarde in de nabije toekomst in kaart gebracht zal worden met regionale modellen. Een belangrijk verschil tussen de regionale en globale modellen is de lengteschaal van de structuren die in de modellen zichtbaar zijn. De globale modellen laten structuren zien die veel grootschaliger zijn dan de structuren in de regionale modellen. Er zijn verschillende factoren die ervoor zorgen dat de kleinschaligere structuren minder aanwezig zijn in de inversieresultaten dan de grootschaligere, zoals de beperkte bedekking van de aarde met paden waardoor een beperkte resolutie optreedt, de regularisatie die nodig is in de inverse procedure en het feit dat de waarnemingen waaruit een model geconstrueerd wordt integralen zijn van de aardstructuur waardoor de informatie van kleinere structuren uitgemiddeld wordt. Een overeenkomst tussen de globale en de regionale modellen is de amplitude van de afgebeelde anomalieën ten opzichte van een sferisch symmetrisch referentiemodel. Deze amplitudes zijn voor beide modellen in de orde van een paar procent.

In de moderne geofysica worden de globale tomografische modellen vaak gebruikt om de seismische structuur van de mantel van de aarde te relateren aan het karakter van mantelconvectie. De ruimtelijke afmetingen van de snelheidsanomalieën in de globale modellen worden zelfs gebruikt om harde uitspraken te doen omtrent het convectieproces in de mantel. Door dit te doen wordt impliciet aangenomen dat de globale modellen een juiste en volledige beschrijving geven van de heterogene structuur in de mantel en dat het gerechtvaardigd is om de kleinschaligere structuur, zoals die te zien is in de regionale modellen, te verwaarlozen als de hele aarde beschouwd wordt. Hoofdstuk 2 gaat over de vraag of het geoorloofd is om te denken dat de mantel overheerst wordt door grootschalige structuren of dat het voorkomen van kleinschaligere structuren op globale schaal erkend moet worden. De lengteschaal van heterogeniteiten in de mantel is niet alleen van belang wat betreft convectie, maar ook andere geodynamische processen hangen sterk af van de lengteschaal van heterogeniteiten in de mantel, omdat de gradiënten in de mantelstructuur de aandrijvende krachten zijn van de dynamische processen. In Hoofdstuk 2 wordt een effect beschouwd dat afhangt van de gradiënt van de mantelstructuur in plaats van de integraal van de structuur. Hiervoor wordt het idee van meerpading uit de kast gehaald. Meerpading houdt in dat de laterale heterogeniteiten in de bovenmantel ervoor zorgen dat de oppervlaktegolven zich voortplanten langs paden die afwijken van de grootcirkel tussen de bron en ontvanger. De verschillende paden

tussen de bron en ontvanger resulteren op de plaats van de ontvanger in een registratie van interferentie van verschillende aankomsten uit verschillende richtingen. Dit heeft tot gevolg dat sommige frequenties constructief zullen interfereren en andere frequenties elkaar zullen uitdoven. Hierdoor zal het amplitudespectrum van de oppervlaktegolven knopen (negatieve interferentie) en buiken (positieve interferentie) gaan vertonen. Met toenemende loopafstand zullen de meerpading effecten sterker worden en zullen de amplitudespectra meer knopen en buiken gaan vertonen. Ook mag aangenomen worden dat in een medium waarin grootschalige structuren overheersen minder meerpading zal optreden dan in een medium waarin de middelgrote en kleinschaligere structuren sterker aanwezig zijn. Dit komt omdat in een medium met kleinere structuren de gradiënten sterker en daarom de afwijkingen van de grootcirkel groter zijn dan in een medium met grotere structuren. In Hoofdstuk 2 worden de amplitudespectra van lang-periodische oppervlaktegolven (tussen 60 en 360 s) geanalyseerd en de meerpading effecten worden vergeleken met de effecten zoals die door de bestaande globale modellen en door een aantal synthetisch gegenereerde modellen voorspeld worden. Deze synthetisch gegenereerde modellen bevatten meer middelgrote structuren dan de globale modellen. De conclusie is dat in de echte aarde de middelgrote structuren sterker aanwezig moeten zijn dan in de globale modellen te zien is. Het is daarom niet geoorloofd structuren met lengteschalen zoals die in de regionale modellen zichtbaar zijn, te verwaarlozen op globale schaal.

In Hoofdstuk 3 wordt een methode verder uitgewerkt en getest om gradiënten en kleinere structuren beter af te beelden. De methode gebruikt golfvormen van oppervlaktegolven afkomstig van een bepaalde beving en geregistreerd in twee stations die niet al te ver van elkaar af liggen. De verschillen in de golfvormen worden geïnverteerd voor een lokaal lateraal homogeen  $S$  snelheidsmodel of voor een padgemiddelde horizontale  $S$  snelheidsgradiënt. In het eerste geval liggen de stations op dezelfde grootcirkel die hen verbindt met de bron. Omdat de stations relatief dicht bij elkaar liggen, leidt dit tot minder uitmidding van de kleinere structuren. In het tweede geval liggen de stations ongeveer even ver van de beving af, maar verschilt het azimuth naar de bron ietwat. In beide gevallen worden de frequentieafhankelijke faseverschillen tussen de geregistreerde golfvormen gebruikt als data voor een inversie voor  $S$  snelheidsinformatie. Enkele voorbeelden met echte data worden getoond voor het tweede geval. De voorbeelden hebben allemaal te maken een duidelijke tectonische scheidinglijn in centraal Europa: de Tornquist-Teisseyre lijn. Beneden een diepte van 80 km wordt loodrecht op deze lijn een snelheidscontrast van 8 tot 9% gevonden. Dit snelheidscontrast onder het centrale deel van de Tornquist-Teisseyre lijn wordt gerealiseerd over een afstand van maximaal 600 km.

Door ook boventonen in de inversie te betrekken kan zelfs een resolutie bereikt worden tot een diepte van 400 km. Voor dit diepere deel wordt een omkering van het teken van het contrast gevonden. Deze resultaten komen goed overeen met andere studies voor dit gebied.

In Hoofdstuk 4 wordt een toepassing getoond van de andere wijze waarop de inversiemethode van Hoofdstuk 3 gebruikt kan worden, nl. wanneer de stations op dezelfde grootcirkel liggen met de bron. Grondtonen van Rayleigh golven met periodes tussen 20 en 100 s zijn geïnverteerd om een model te krijgen van de drie-dimensionale  $S$  snelheidsverdeling onder centraal en zuid Duitsland. De data zijn afkomstig van 27 teleseismische bevingen geregistreerd in 17 breedbandstations in Duitsland en omgeving. Dit resulteert in 56 paden, steeds tussen twee stations die elk op dezelfde grootcirkel met een epicentrum liggen. De faseverschillen tussen de golfvormen geregistreerd door een stationspaar zijn direct geïnverteerd voor de pad-gemiddelde  $S$  snelheidsverstooring tussen de twee stations. Alle padmodellen werden vervolgens gecombineerd in één drie-dimensionaal model. De belangrijkste structuren van het verkregen model zijn (1) lage snelheden onder de Eger Slenk, die een gevolg zijn van de diepe structuur van deze rift, (2) hoge snelheden tussen 40 en 120 km diepte onder noord Beieren, duidend op een dikker wordende lithosfeer naar het zuiden toe, (3) hoge snelheden onder het gebied van de zuidelijke Rijn Slenk (tegenwoordig niet actief wat betreft rifting), hetgeen wijst op afwezigheid van omhoogkomend heet mantelmateriaal, en (4) lage snelheden onder het noordelijke deel van de Rijn Slenk en de noordelijke tak van het Centraal Europese riftsysteem, de tak die tegenwoordig wel actief is wat betreft rifting. Dit gebied beslaat het Rijns Massief ten westen van de Rijn en de vulkanische gebieden van de Eifel. Deze lage snelheden duiden op het omhoog komen op grote schaal van de lithosfeer-asthenosfeer grens. Het model laat een duidelijke correlatie zien tussen de  $S$  snelheid in de bovenmantel tot een diepte van 200 km en tektonische verschijnselen aan het oppervlak.

De hoge snelheidsanomalie onder Beieren zoals die te zien is in het model dat in Hoofdstuk 4 behandeld is, kan gezien worden als een uitdrukking van de Alpine lithosferische wortel. In Hoofdstuk 5 komt een mogelijke alternatieve verklaring voor deze anomalie aan de orde, die gerelateerd is aan de Alpine geschiedenis. Het sluiten van de Piemont oceaan in het Krijt is een proces dat is gerelateerd aan de ontwikkeling van de Alpen en het noordelijke voorland. Er wordt gesteld dat tijdens het sluiten van deze oceaan de jonge oceanische Adriatische plaat in een noordwaartse richting horizontaal subduceerde onder centraal Europa (lithosferische verdubbeling). Op een bepaald moment, waarvan de exacte timing niet is vastgelegd door het alternatieve scenario, draaide de subductiepolariteit om naar de huidige zuid-

waartse subductie van de Europese plaat [*Wortel*, pers. comm.]. Er wordt gesteld dat het hierbij los gekomen deel van de Adriatische plaat achter bleef onder centraal Europa. Doordat dit stuk oceanische lithosfeer jong was, zonk het niet weg naar grotere diepte. De waargenomen hoge snelheidsanomalie zou het gevolg zijn van dit achtergebleven stuk oceanische lithosfeer. In Hoofdstuk 5 worden de eerste-orde implicaties van het voorgestelde scenario onderzocht in termen van thermische, compositionele en gravitationele effecten. Er wordt aangetoond dat thermische effecten op zich de waargenomen snelheidsanomalie niet kunnen verklaren, omdat de verschillen in temperatuur bijna verdwenen zijn door de lange afkoelingsgeschiedenis. Het is daarom meer waarschijnlijk dat compositionele effecten, misschien samen met kleine temperatuurseffecten, de hoge snelheden kunnen verklaren. Ook wordt aangetoond dat de gravitationele implicaties van het lithosferische verdubbelingsscenario consistent zijn met groot-schalige observaties van de Bougueranomalie.

In Hoofdstuk 6 wordt de golfvorminversiemethode van Hoofdstuk 3 gebruikt om bepaalde structuren en amplitudes van een drie-dimensionaal tomografisch model te testen. Als voorbeeld worden enkele kenmerken van een recent *S* snelheids model van Australië getest. Uit de data verkrijgen we direct lokale metingen van de snelheidsstructuur op verschillende plaatsen onder het Australische continent. Deze metingen hebben niet te lijden van verschillende problemen die optreden in tomografische inversies van grote datasets, zoals bijvoorbeeld variaties in resolutie en verschillende bemonstering van anisotropie. Bijgevolg zijn de resultaten een onafhankelijke test van de kenmerken van het drie-dimensionale model van Australië. De lokale metingen verkregen in Hoofdstuk 6 zijn consistent met dit model.

Het werk dat in dit proefschrift beschreven is, heeft duidelijk gemaakt dat middelgrote en kleinschalige bovenmantelheterogeniteiten onderschat worden in de huidige globale seismologische modellen. Dit impliceert dat sterke gradiënten ook onderschat worden. Omdat de gradiënten de aandrijvende krachten achter allerlei geodynamische processen zijn, is een goed beeld van de gradiënten en structuren gewenst als men seismologische modellen wil interpreteren in een geokinematisch en geodynamisch licht. Vervolgens is een methode beschreven en getest om, met behulp van oppervlaktegolven, gradiënten en kleinschalige bovenmantelstructuur in kaart te brengen. Deze methode is toegepast om een drie-dimensionaal snelheidsmodel van centraal en zuid Duitsland te maken tot een diepte van 200 km. Ook is de methode gebruikt om aspecten van een model van de *S* snelheidsstructuur onder Australië te testen. Een karakteristiek kenmerk van het Duitslandmodel, een hoge snelheidsanomalie onder noord Beieren, is geïnterpreteerd in het licht van een kinematisch scenario, bestaande uit een paleo-subductie proces. Deze interpretatie is een voorbeeld van de rol die seismologische modellen kunnen spelen in de geodynamica.

Om deze rol in de toekomst belangrijker te maken, moeten seismologische studies zich onder andere blijven richten op het correct in kaart brengen van kleinschalige structuren in de bovenmantel in de gebieden die geodynamisch gezien interessant zijn.

## Acknowledgments

Ofschoon alleen mijn naam op de kaft van dit boekje staat, is het zeker niet zo dat de inhoud van dit proefschrift tot stand is gekomen zonder enige vorm van begeleiding, ondersteuning, hulp en samenwerking. Iedereen die op wat voor manier dan ook heeft bijgedragen aan mijn promotie werk in de afgelopen vier jaar wil ik daar bij deze hartelijk voor bedanken. Een aantal personen en instanties verdient het om even apart genoemd te worden.

Allereerst wil ik mijn promotor en begeleider Roel Snieder bedanken voor zijn begeleiding van het onderzoek. Zijn enthousiasme en brede vakkennis, in combinatie met zijn prettige manier van samenwerken, hebben mij altijd goed op weg geholpen. En gehouden! Mede door zijn wekelijkse aio-spreekuur is dit proefschrift gezond ter wereld gekomen. Zijn vele keuringen van tussentijds geproduceerde manuscripten bleken een goed medicijn tegen een al te zware bevalling op het einde. Bovendien heeft hij mij gewezen op de schoonheid van een 727 en een MD-11, iets wat mij anders volkomen zou zijn ontgaan.

Ook ben ik Rob van der Hilst dankbaar voor zijn initiatief om mij naar MIT te laten komen om daar het werk te verrichten met de SKIPPY data. Het was plezierig om met hem samen te werken. Dit uitstapje tegen het einde van mijn tijd als aio heb ik als bijzonder leerzaam ervaren. I would like to thank MIT for their hospitality and providing the facilities to carry out the work described in Chapter 6. I thank NATO for supporting my stay at MIT financially. Ik wil Shell bedanken voor het financieren van de reiskosten naar het IUGG congres in Boulder, Colorado in juli 1995. De financiële bijdragen van zowel NWO als de faculteit Aardwetenschappen om bezoeken aan verschillende congressen mogelijk te maken, werden erg gewaardeerd.

The work described in this thesis has benefitted from constructive comments by various reviewers over the past four years. In particular, I would like to thank Yu-Shen Zhang and Oli Gudmundsson for their help on the work described in Chapter 2. In addition, Barbara Romanowicz provided useful suggestions for the same chapter. De medewerking van Reinoud Vissers en Martyn Drury bij de geologische interpretatie van het Duitsland model was ook bijzonder welkom. Bij het zoeken naar geschikte data voor Hoofdstuk 4 was het erg handig om Bernard Dost en zijn Orfeus Data

Centrum in de buurt te hebben. Ook ben ik dank verschuldigd aan Rob Govers voor zijn hulp bij het tot stand komen van Hoofdstuk 5. Zonder zijn tektonofysische kijk op de aarde zou ik, als seismoloog, een aantal geodynamische processen ongetwijfeld op brute wijze geweld aan gedaan hebben.

Dat ik altijd met plezier naar het IvA gekomen ben, kwam mede doordat ik altijd op een prettige samenwerking kon rekenen op de momenten dat dat nodig bleek. Een aangename werksfeer zoals die onder de medewerkers en studenten van de vakgroep geofysica aanwezig is, hoop ik ook in de toekomst te mogen blijven ervaren. I also thank all the foreigners who worked in the seismology group in Utrecht over the past few years during my time as a graduate student. I feel they were the ingredients that are necessary to season a Dutch institute.

Mijn dank gaat ook uit naar mijn ouders. Hun oprechte interesse door de jaren heen in mijn werk en welzijn stel ik nog altijd zeer op prijs. In het bijzonder was de steun die ik van hen tijdens mijn eerste studiejaar in Utrecht heb gekregen van cruciaal belang. In de afgelopen jaren ben ik gaan beseffen dat deze ouderlijke steun extra waardevol is, omdat het krijgen ervan lang niet altijd zo vanzelfsprekend is als dat ik voorheen altijd gedacht had.

IJsaap wordt bedankt voor zijn eeuwige en alles relativierende aanwezigheid.

Als laatste, maar zeker niet als minste, Fraukje, wil ik jou bedanken. Zonder jou was dit proefschrift er nooit gekomen.



## Curriculum Vitae

De schrijver van dit proefschrift werd op 13 mei 1969 geboren te Bergen op Zoom. In 1981 werd begonnen met het VWO aan het Gertrudis Lyceum in Roosendaal. In mei 1987 werd daar het atheneum-B diploma gehaald. In dat zelfde jaar werd begonnen met de studie geofysica aan de Universiteit Utrecht, alwaar in november 1988 het propaedeutisch examen en in juli 1992 het doctoraal examen behaald werd. Aansluitend hierop was de auteur tot augustus 1996 werkzaam als assistent in opleiding bij de vakgroep geofysica aan de Universiteit Utrecht. De maanden april en mei in 1996 werden doorgebracht aan het Massachusetts Institute of Technology. Na voltooiing van het proefschrift trad hij in dienst bij Koninklijke/Shell, afdeling exploratie en produktie.

*Tonight my bag is packed  
Tomorrow I'll walk these tracks  
That'll lead me across the border*

---

*Bruce Springsteen, 1995  
Across the border*